# Improving Contrast Agent Based Cerebral Perfusion Assessment

## Arterial input function measurement and leakage correction

Tseng, C.

**DOI**
10.4233/uuid:92f49cdb-dc0b-4467-9598-7138957fec48

**Publication date**
2025

**Document Version**
Final published version

**Citation (APA)**
Tseng, C. (2025). *Improving Contrast Agent Based Cerebral Perfusion Assessment: Arterial input function measurement and leakage correction*. [Dissertation (TU Delft), Delft University of Technology]. https://doi.org/10.4233/uuid:92f49cdb-dc0b-4467-9598-7138957fec48

**Important note**
To cite this publication, please use the final published version (if applicable).
Please check the document version above.

# Improving Contrast Agent Based Cerebral Perfusion Assessment

## Arterial input function measurement and leakage correction

**Chih-Hsien Tseng**

# Improving contrast agent based cerebral perfusion assessment

Arterial input function measurement and leakage correction

# Improving contrast agent based cerebral perfusion assessment

Arterial input function measurement and leakage correction

## Dissertation

for the purpose of obtaining the degree of doctor
at Delft University of Technology
by the authority of the Rector Magnificus, prof. dr. ir. T.H.J.J. van der Hagen,
chair of the Board for Doctorates
to be defended publicly
on **Wednesday 19 March 2025** at **17:30** o'clock

by


**Chih-Hsien TSENG**

Master of Science in Biomedical Engineering,
National Taiwan University, Taiwan,
born in Taipei, Taiwan

This dissertation has been approved by the promotors:

Dr. F. M. Vos
Prof. dr. ir. M. J. P. van Osch
Prof. dr. M. Smits

Composition of the doctoral committee:

| | |
|---|---|
| Rector Magnificus, | chairperson |
| Dr. F. M. Vos, | Delft University of Technology, promotor |
| Prof. dr. ir. M. J. P. van Osch, | Leiden University Medical Center, promotor |
| Prof. dr. M. Smits, | Erasmus MC, promotor |
| *Independent members:* | |
| Prof. dr. J.A. Hemandez-Tamames | Delft University of Technology |
| Prof. dr. L. Knutson | Johns Hopkins School of Medicine, USA |
| Prof. dr. ir. W.H. Backes | Maastricht UMC |
| Dr. ir. P.J. van Houdt | Netherlands Cancer Institute |
| Prof. dr. S. Stallinga | Delft University of Technology, reserve member |

This research is part of the "HollandPTC-Varian consortium-confined call 2018" program (project number: 2018017) financed by the HollandPTC-Varian consortium.

*Keywords:* Gadolinium-based contrast agent, perfusion MRI, cerebral perfusion, vascular permeability, arterial input function, inflow artifact, partial volume effect, leakage correction, numerical methods.

*Printed by:* Gildeprint

*Cover by:* Chih-Hsien Tseng. Includes adapted images generated by OpenArt.



ISBN 978-94-6518-024-3

An electronic copy of this dissertation is available at
https://repository.tudelft.nl/.

*In theory, there is no difference between theory and practice.*
*But, in practice, there is.*

Jan L. A. van de Snepscheut

# CONTENTS

# SUMMARY

Magnetic resonance imaging (MRI) is a widely used medical imaging technique enabling detailed contrast in soft tissues such as the brain. Traditionally, MRI produces qualitative, 'weighted' images that merely emphasize properties like the longitudinal ($T_1$) and transverse ($T_2^*$) relaxation times. Alternatively, quantitative MRI (qMRI) measures underlying tissue parameters directly, offering enhanced reproducibility and sensitivity to various pathological conditions. This dissertation focuses on advancing the qMRI techniques: dynamic susceptibility contrast (DSC) and dynamic contrast enhanced (DCE) MRI. Specifically, it aims to improve the accuracy and reliability of cerebral perfusion measurements in brain tumors.

Initially a comprehensive literature review on the application of DCE and DSC MRI in glioma imaging is provided in **Chapter 2**. It highlights their potential to derive biomarkers for assessing tumor hemodynamics, grading, treatment response, and prognosis. In spite of this promise, significant barriers to clinical adoption are identified, including the lack of standardized acquisition protocols and analysis methods. The chapter emphasizes the need for robust and reproducible frameworks to ensure consistent perfusion measurements across different clinical settings and imaging platforms, signifying the importance of the original research of this dissertation.

The arterial input function (AIF) is a critical factor for accurate perfusion parameter estimation in DSC MRI. Therefore, we explore sophisticated strategies for AIF measurement in **Chapter 3**. This study demonstrates that AIFs derived from DCE MRI exhibit superior reproducibility and reliability compared to those obtained directly from DSC MRI. Also, DCE-derived AIFs provide more consistent perfusion estimates. As such utilizing a DCE-driven AIFs offers a more reliable alternative to traditional DSC-based AIFs.

To further improve the AIF determination, we introduce in **Chapter 4** an innovative methodology to simultaneously correct for inflow and partial volume effects (PVEs) on DCE AIF measurement. We establish that the PVE closely resembles the inflow effect, enabling their concurrent mitigation. Clinical validation involving ten patients with diverse brain tumors confirms the efficacy of the proposed method. What is more, it is demonstrated that alternative AIF sources, such as the superior sagittal sinus (SSS), are unsuitable due to contrast agent dispersion. Therefore, we advocate to derive the AIF directly from arterial regions and applying a meticulous correction method to ensure reliable vascular parameter assessment.

In **Chapter 5**, we propose a comprehensive method that integrates DCE and DSC image analysis to correct for contrast agent leakage in DSC MRI. Simulations demonstrate that it facilitates precise estimation of essential vascular parameters, includ-

ing the volume transfer constant, vascular volume, and extravascular volume fraction. Furthermore, it is shown that the method induces minimal bias in the parameter estimates. As a result, leakage artifacts are efficiently eliminated, which is pivotal for cerebral blood volume estimation. Clinical application in ten patients showcases that the proposed method preserves more realistic contrast agent levels than the current standard. This preservation can ensure that vital properties of the vascularization can be accurately measured, enhancing the DSC technique's reliability.

In summary, the techniques introduced in this dissertation offer solutions to several challenges inherent to DCE and DSC MRI. As such this research paves the way for more accurate, reliable, and clinically applicable perfusion assessment, which may have important implications for neuro-radiology.

# SAMENVATTING

Magnetic Resonance Imaging (MRI) is een vaak gebruikte medische beeldvormingstechniek, die veel contrast geeft in zachte weefsels, zoals de hersenen. Traditioneel levert MRI kwalitatatieve, zogenaamd 'gewogen' beelden die slechts bepaalde fysische eigenschappen benadrukken. Kwantitatieve MRI (qMRI), daarentegen, meet de onderliggende weefselparameters zelf, wat een verbeterde reproduceerbaarheid en gevoeligheid bij diverse ziektes levert. Dit proefschrift richt zich op de verbetering van de qMRI-technieken Dynamic Susceptibility Contrast (DSC) en Dynamic Contrast Enhanced (DCE) MRI. Uiteindelijk is het doel om hiermee de nauwkeurigheid en betrouwbaarheid van metingen van de bloeddoorstroming (perfusie) in hersentumoren te verbeteren.

Aanvankelijk wordt in **Hoofdstuk 2** een uitgebreide literatuurstudie gepresenteerd over de toepassing van DCE- en DSC-MRI in de beeldvorming van veel voorkomende hersentumor: gliomen. Daarbij wordt met name gekeken naar mogelijkheden om eigenschappen te meten met betrekking tot de hemodynamica in deze tumoren, maar ook de gradatie, behandelrespons en prognose. Ondanks veelbelovende vooruitzichten worden ook obstakels voor klinische implementatie genoemd, waaronder het ontbreken van gestandaardiseerde acquisitie-protocollen en analyse methodes. Het hoofdstuk benadrukt de noodzaak van robuuste en reproduceerbare technieken om consistente perfusiemetingen te waarborgen. Deze moeten kunnen worden toegepast in verschillende klinische omgevingen en types MRI scanner, wat het belang van het onderwerp van dit proefschrift onderstreept.

De Arteriele Input Function (AIF) is een cruciaal onderdeel bij het schatten van perfusieparameters gebaseerd op DSC-MRI. Daarom onderzoeken we in **Hoofdstuk 3** geavanceerde werkwijzen voor AIF-meting. Deze studie toont aan dat AIF's afgeleid van DCE-MRI een superieure reproduceerbaarheid hebben vergeleken met AIF's verkregen uit DSC-MRI. Het gebruik van een DCE-gestuurde AIF biedt derhalve een betrouwbaarder alternatief voor traditionele, op DSC gebaseerde AIF's.

Om de bepaling van de AIF verder te verbeteren, ontwikkelen we in **Hoofdstuk 4** een innovatieve techniek om gelijktijdig te corrigeren voor ongewenste instroom- en Partiele Volume-Effecten (PVE's) op de DCE-AIF-metingen. We laten zien dat PVE's sterk lijken op instroom effecten, waardoor een gelijktijdige compensatie mogelijk is. Klinische validatie in tien patiënten met uiteenlopende hersentumoren toont de effectiviteit van de ontwikkelde methode. Bovendien wordt aangetoond dat meting in de Superior Sagittal Sinus (SSS), waar geen instroom effecten zijn, niet een geschikt alternatief is. Daarom pleiten wij ervoor de AIF direct te meten in arterien en een goede correctiemethode toe te passen .

In **Hoofdstuk 5** stellen we een nieuwe methode voor die DCE en DSC beeldanalyse integreert om te corrigeren voor ongewenste effecten van lekkage van contrastmiddel in DSC-MRI. Simulaties tonen aan dat de methode een nauwkeurige meting van belangrijke vasculaire parameters mogelijk maakt, waaronder een transfer constant, het vasculaire volume en de extravasculaire volume-fractie. Daarbij worden lekkage-artefacten dus op efficiënt wijze gecorrigeerd. Klinische toepassing bij tien patiënten laat zien dat de voorgestelde methode realistische metingen geeft dan de huidige standaard. Dit verhoogd de betrouwbaarheid van de metingen door DSC-MRI.

Samengevat bieden de in deze dissertatie geïntroduceerde technieken oplossingen voor verschillende problemen die inherent zijn aan DCE- en DSC-MRI. Dit onderzoek effent daarmee de weg voor een nauwkeurigere, betrouwbaardere en beter klinisch toepasbare perfusiebeoordeling, wat zeer belangrijk is voor de neuroradiologie.

# 1

# General Introduction

1

Magnetic resonance imaging (MRI) is widely used for diagnosis and monitoring of brain diseases, offering detailed images of the anatomy with high spatial resolution. Conventional MRI techniques, such as $T_1$-weighted and $T_2$-weighted imaging, enable identifying the location, size, and approximate extent of brain tumors. These techniques rely on the different relaxation times of water protons in various tissues to generate contrast and delineate pathological from normal brain tissue. However, for a deeper understanding of the microstructural alterations and vascular characteristics in a tumor, conventional MRI is insufficient. Specifically, it does not facilitate optimal differentiation between tumor types, assessment of tumor grade, and distinction between tumor recurrence and treatment-related changes, such as radiation or post-surgical effects.

Advanced MRI techniques can offer information that goes beyond anatomical details of a brain tumor. Specifically, perfusion MRI provides data on vascular permeability and blood flow of the tumor and surrounding tissues. In this way insight can be obtained into the tumor's metabolic properties, which can help in tumor grading, assessment of pathological progression, longitudinally post-treatment monitoring, and predicting treatment response.

Perfusion MRI techniques encompass contrast-based methods, such as dynamic contrast enhanced (DCE) and dynamic susceptibility contrast (DSC) MRI, which rely on intravenous contrast agent injection to highlight blood vessels and blood flow. Alternatively, arterial spin labeling (ASL) is a non-contrast-agent based method that uses the spins in blood as an intrinsic tracer to estimate cerebral blood flow. In general, the former methods generate high signal- and contrast-to-noise ratio due to large relaxation changes induced by the contrast agents. Therefore, they are more widely applied in clinical applications. This thesis focuses on new image processing methods for contrast agent based perfusion MRI, applied to brain tumor imaging.

## 1.1. Basic principles of MRI

MRI relies on quantum mechanical properties that hydrogen spins exhibit when placed within a strong magnetic field ($B_0$). Specifically, in the presence of such a magnetic field, these spins tend to align with the field's direction. As a consequence, the aggregate of millions of spins locally creates a net magnetization vector. This rest situation can be disturbed, however, by applying a radiofrequency (RF) pulse, that tilts the net magnetization vector towards the transverse plane, perpendicular to the main magnetic field direction. Once the RF pulse is turned off, the protons relax back to the original equilibrium state, which is generally referred to as relaxation. Particularly, this process is characterized by two distinct *relaxation* times: the longitudinal relaxation time ($T_1$), reflecting the time for the spins to realign with the main magnetic field direction, and the transverse relaxation time ($T_2$), corresponding to the time for the magnetization to disappear from the transverse plane. During the relaxation process, additional magnetic fields are superimposed on the main magnetic field, varying linearly in strength

along a particular axis (x, y, or z) to allow for localization and measurement of the magnitude of the magnetization. The signals emitted during the relaxation processes are detected by receiver coils, and are converted into images.

Image contrast in MRI is primarily determined by the differences in $T_1$ and $T_2$ relaxation times of various tissues, as well as the density of hydrogen protons. By adjusting the parameters of the MRI protocols, such as the repetition time (TR), the echo time (TE), and the flip angle (FA), the generated images can emphasize the magnitude of the magnetization along the direction of the main magnetic field or in the transverse plane, yielding $T_1$-weighted or $T_2$-weighted images, respectively. Practically, $T_1$-weighted images are useful for visualization of normal anatomy and assessment of fat-containing structures, whereas $T_2$-weighted images are sensitive to changes in water content, typically associated with pathology (e.g. edema).

## 1.2. GADOLINIUM-BASED CONTRAST AGENTS

Gadolinium-based contrast agents (GBCAs) are paramagnetic substances that modulate the relaxation times of the magnetization. These alterations of the relaxation times can effectively increase the image contrast, providing valuable insight into the dynamics of blood flow and the microvascular environment in tissues, c.q. brain tumors.

GBCAs predominantly shorten the longitudinal relaxation time. As such they enable a quicker realignment of the spins with the main magnetic field after the application of a radiofrequency pulse. This acceleration of longitudinal relaxation results in an increased signal intensity on $T_1$-weighted images, especially in areas with high contrast agent concentration, e.g. in regions with disrupted blood-brain barrier (BBB) in the brain. Furthermore, this effect enables the delineation of vascular structures and assessment of the perfusion of tissues (see further below). $T_1$-weighted images are often acquired before and after GBCA administration for localization of tumors and assessment of the contrast-enhancing volume. Additionally, dynamic $T_1$-weighted imaging before, during and after contrast injection can be applied to derive several meaningful parameters of the vascularization. The latter application is generally referred to as DCE MRI and will be described in detail in the next section.

While a primary use of GBCAs is based upon the enhancing $T_1$ contrast effect, the transverse relaxation time is also influenced by GBCAs, albeit through different mechanisms. GBCAs cause a decrease in transverse relaxation time, through dephasing which yields signal loss in $T_2$- and $T_2^*$-weighted images. This reduction of transverse relaxation results from susceptibility changes induced by the presence of the GBCA in blood vessels. This phenomenon when monitored by dynamic imaging, also allows for detailed assessment of hemodynamic parameters and vascular integrity. It is particularly exploited in DSC MRI, in which the transient decrease in signal intensity following the bolus injection of a GBCA is measured by $T_2$- or $T_2^*$-weighted acquisitions (see further below).

1

## 1.3. Dynamic contrast enhanced MRI

The relevance of DCE MRI lies in its ability to visualize and quantify the kinetics of GBCAs within tissues. By monitoring the signal intensity changes in $T_1$-weighted images, DCE MRI facilitates assessment of the distribution and clearance of the contrast agent, and offers insight into vascular properties of the target tissues [1, 2]. In particular, this concerns physiological parameters including blood flow, vessel permeability, and the volume of the extracellular extravascular space (EES), which are critical for understanding tumor biology and the effects of therapeutic interventions.

In normal brain tissue, the intact structure of the BBB prohibits leakage of the GBCAs from the plasma to the interstitial space [3]. However, the BBB may be damaged in tumors, leading to GBCA uptake in the interstitium [4]. To quantify the integrity of the BBB and vascular characteristics, pharmacokinetic models are employed, of which the extended Tofts model (ETM) is the most often applied. The ETM asserts that the tissue signal emanates from two compartments: the blood plasma and the EES [5]. Effectively, it models the contrast agent concentration in tissue over time ($C_t(t)$) through the following expression:

$$C_t(t) = v_p \cdot C_p(t) + K^{trans} \cdot \int_0^t C_p(t') \cdot e^{-k_{ep} \cdot (t-t')} \, dt', \tag{1.1}$$

in which $C_p(t)$ is the contrast concentration in the plasma of an artery feeding the tissue, which is known as the arterial input function (AIF). Conventionally, the AIF is measured from a nearby artery close to the tissue of interest in the acquired DCE images. The volume transfer constant $K^{trans}$ and the rate constant $k_{ep}$ represent the rate of the GBCA diffusing from the plasma to the interstitium and vice versa while $v_p$ reflects the fractional volume of the plasma. These parameters are estimated by fitting this model to the measured data.

The $K^{trans}$ parameter represents the product of the permeability of the capillaries and the surface area available for exchange. A $K^{trans}$ value deviating from zero can be observed in tumor tissue compared to normal brain tissue, which is characteristic of low quality blood vessels supporting the growth of tumors, the neovasculature. This parameter has been used for assessing tumor grade, monitoring angiogenesis over the course of treatment, and evaluating the efficacy of anti-angiogenic therapies [6, 7]. Additionally, the $k_{ep}$ parameter describes the rate at which the contrast agent returns from the EES back into the plasma space. The two parameters combined describe the dynamic transitions of the contrast agent between the plasma and the EES. $k_{ep}$ is typically calculated as the ratio of $K^{trans}$ and the fractional volume of the EES ($v_e$). A higher $k_{ep}$ value may indicate a more efficient exchange between the two compartments, which is assumed to be associated with tumor characteristics, such as cellular density and the quality of the newly formed tumor vasculature. Monitoring changes in $k_{ep}$ can help evaluating treatment response, particularly in therapies aimed at supressing tumor vasculature [8]. Finally, $v_p$ represents the volume of the plasma compartment within the voxel of interest. It is indicative of the blood volume of the tissue and provides

insight into the vascularization of the tumor. High $v_p$ values have been associated with strongly vascularized tumors, such as high-grade gliomas, and may reflect the presence of large or numerous blood vessels within a tumor. Therefore, assessing $v_p$ can be useful for distinguishing between tumor types, grading tumors, and to evaluate the impact of treatment aimed at reducing the tumor's blood supply.

## 1.4. DYNAMIC SUSCEPTIBILITY CONTRAST MRI

DSC MRI also plays an essential role in assessing cerebral hemodynamics and evaluating the microvascular status of brain tumors. It involves the rapid acquisition of $T_2$- or $T_2^*$-weighted images before, during, and after intravenous injection of a bolus of GBCA. The passage of this contrast agent bolus through the cerebral vasculature induces transient changes in the magnetic susceptibility of blood, leading to a decrease in signal intensity on $T_2^*$-weighted images [9]. This phenomenon is grounded in the indicator dilution theory, which poses that the concentration of a tracer (the contrast agent) can be used to infer the volume and flow characteristics of tissue [10]. Accordingly, whole brain maps of cerebral blood volume (CBV) and cerebral blood flow (CBF) can be generated from a DSC analysis. Additionally, the mean transit time (MTT) describing the average time for blood to pass through the capillaries in a brain region can be calculated as the ratio of CBV over CBF.

In DSC MRI, a linear relationship between the contrast concentration and the change of transverse relaxation ($\Delta R_2^*$) is usually assumed. Accordingly, the concentration over time during the passage of the GBCA in a volume of tissue $C(t)$ is often characterized through:

$$C(t) \propto \Delta R_2^* = \frac{-1}{TE} \cdot \ln \frac{S(t)}{S_0}, \tag{1.2}$$

in which $TE$ is the applied echo time, $S(t)$ is the measured signal, and $S_0$ is the baseline signal before contrast administration. CBV is defined by the volume of blood in a given amount of brain tissue. It is indicative of the capillary density and can be derived by the normalized integration of the concentration over time, i.e. the area under curve of $C(t)$ divided by the area under curve of the AIF. The relationship between the tissue response and the AIF can be expressed in terms of the following convolution integral:

$$C(t) = CBF \cdot C_p(t) \circledast R(t), \tag{1.3}$$

in which $R(t)$ is a residue function describing the fraction of tracer remaining in the system at a given time t. Therefore, CBF can be estimated by deconvolving $C(t)$ with the AIF ($C_p(t)$). Lastly, MTT can be computed as the ratio of CBV over CBF [11].

The interpretation of CBV, CBF, and MTT in brain tumor imaging is important for diagnosing, characterizing, and evaluating brain tumors. For instance,

high-grade tumors often show increased CBV due to elevated angiogenesis and vascular density. Alternatively, CBF can vary depending on the tumor's metabolic activity and the integrity of its vascular supply. Moreover, increased MTT might indicate impaired blood flow or increased vascular resistance within the tumor. As such, these parameters enable the differentiation between tumor classification, discrimination of true tumor progression from treatment-induced abnormalities, e.g. radiation necrosis or pseudoprogression, and assessment of treatment effects, such as the efficacy of anti-angiogenic therapy [12, 13].

## 1.5. A combined protocol

DCE and DSC MRI might be individually included in a clinical imaging protocol. However, consecutive application of DCE MRI and DSC MRI could facilitate to combine the best of two worlds.

A fundamental assumption underlying of traditional DSC imaging is that the GBCA remains intravascular, and is not leaking into the EES. However, this assumption may not hold in tumors, in which the integrity of the BBB can be compromised. The leakage of contrast agent into the EES can significantly affect the accuracy of hemodynamic parameter estimation. Typically, this extravasation has a $T_1$ shortening effect which makes that the measured signal is increased compared to the situation without leakage. To mitigate this detrimental effect, an additional preload injection of the contrast agent is often applied [14]. The rationale behind the preload injection is to let the GBCA partially occupy the EES, leading to decrease of the $T_1$-value in advance of the main bolus injection. Thereby, the undesired $T_1$ shortening effect is minimized in the subsequent DSC acquisition, facilitating a more accurate estimation of the DSC parameters.

The preload injection can be exploited for extra information by performing DCE MRI during its injection. This approach leverages the initial GBCA administration as it both functions as the preload for the DSC acquisition and provides the contrast enhancement for DCE acquisition, enabling a comprehensive evaluation of tumor perfusion and vascular permeability in a single MRI protocol. Thus, the consecutive application of DCE MRI and DSC MRI could enhance the efficiency of the imaging procedure, and might enrich the diagnostic and prognostic value of perfusion MRI. This could pave the way for better informed clinical decision-making and personalized therapeutic interventions.

## 1.6. Research challenges

### 1.6.1. Imprecise AIF measurement in DSC MRI

Accurate measurement of the AIF in DSC MRI is pivotal for unbiased haemodynamic parameter estimation. Ideally, the AIF should be obtained in an artery that directly feeds the target tissue. However, this is often impractical due to limited spatial resolution. In brain imaging, the AIF is often determined from larger arteries, such as the internal carotid artery (ICA) or the middle cerebral

artery (MCA), which can be easily localized on DSC images. Several automatic algorithms were proposed for AIF measurement, but still some challenges remain.

One important challenge lies in the uncertain relationship between the change in the transverse relaxation rate ($\Delta R_2^*$) and the actual concentration of the contrast agent. It is common practice to assume that this relation is linear. At the same time, however, there is ample evidence suggesting that this relationship is more accurately described as quadratic [15, 16]. Also, the relation is known to vary with the hematocrit levels in the blood. This complexity introduces inaccuracies in quantifying the perfusion metrics.

What is more, precise delineation of the AIF is hindered by inherent limitations in MRI resolution. The AIF is assumed to be measured inside an artery. However, partial volume effects (PVEs) can lead to a mixture of signals from the different tissue types within a voxel, resulting in nonlinear distortions of the AIF due to different evolutions of the phase of the MRI signal between different compartments [17]. In addition, the signal intensity measured in large arteries may diminish to the point of blending with background noise during the transit of the contrast agent, a phenomenon known as signal depletion [18]. This issue is exacerbated by the clinical preference for using a single, extended echo time, optimized for tracking the bolus passage in the brain's tissue rather than in the arteries. Last but not least, the peak of the time-concentration curve obtained from arterial voxels can be distorted by displacement effects. These effects result from a change in precession frequency induced by the paramagnetic properties of the contrast agent which interferes the spatial localisation of the MRI sequence [19].

In practice, one might select arterial-like signals from tissue surrounding the arteries to eliminate or diminish the above mentioned effects. However, this only guarantees that at best the shape of the measured AIF is reliable, whereas the amplitude may not reflect the real contrast concentration in blood, hindering the absolute measurement of CBV and CBF. Therefore, a solid method to assess the true AIF, revealing the feeding contrast to the tissue, is still needed for accurate DSC analysis.

### 1.6.2. DETRIMENTAL EFFECTS ON THE DCE AIF

The AIF is also fundamental to accurate perfusion parameter estimation in DCE MRI. In comparison to DSC MRI, however, the relation between the MRI signal and the contrast agent concentration is much more stable and well established. Still, PVEs in DCE MRI remain unavoidable even though DCE imaging comes with higher resolution than DSC imaging. Typically, PVEs result in an underestimated concentration of the GBCA. To solve this issue previous studies suggested to normalize the AIF with the contrast agent concentration measured in the superior sagittal sinus (SSS) [20, 21]. Alternatively, the signal from the SSS (also referred to as the venous output function (VOF)) has been directly employed as an input for the pharmacokinetic model [22, 23]. However, it is important to note that normalization techniques are only reliable with minimal contribution of signal

from surrounding tissue to the AIF [20]. Also, biases may be introduced due to the dispersed nature of the concentration-time curve of the VOF compared to the AIF [24].

Furthermore, it is usually assumed that the magnetization of the recorded signal is in the steady state. This assumption is often invalid in arteries with strong blood flow [25]. Here, the continuous influx of "fresh" spins, which have not undergone sufficient excitations to reach a steady state, can lead to an artificially heightened signal at baseline and an underestimation of the $T_1$ signal enhancement. Various approaches have been proposed to mitigate the influence of this inflow effect, including the use of flow phantoms for calibration [26]. However, such calibrations are typically dependent on the specific imaging sequence, subject, and system, limiting their general applicability. As an alternative, measuring the AIF downstream can enhance accuracy but may not be feasible in all imaging scenarios [27]. Alternatively, the AIF can be derived from phase accumulation induced by the GBCA, a technique that is not affected by inflow effects [28]. However, this phase signal is susceptible to phase wrapping and flow-induced phase shifts. While correction methods were developed for specific applications, such as liver DCE imaging [29, 30], their general applicability remains constrained.

### 1.6.3. Leakage effects on DSC parameters

In DSC MRI, a critical assumption underpinning the analysis is that the GBCA remains exclusively within the vasculature. Essentially, it is asserted that the BBB is intact, preventing leakage into the interstitial space. However, in brain tumors, the BBB is often damaged, rendering this assumption invalid. Leakage of the contrast agent into the interstitial space introduces significant biases into the estimated DSC parameters, especially of the CBV [31]. Thus, addressing this leakage artifact is imperative for accurate estimation of the perfusion coefficients.

As mentioned above, a preload injection can help to limit the leakage effect, but it can not entirely prevent the issue. The conventional approach to leakage correction involves a model fitting technique that aims to estimate the leaked, extravascular GBCA's concentration and discounting its effect from the observed tissue signal. The most widely used algorithm nowadays was developed by Boxerman et al. [32]. However, this approach was shown to yield incorrect outcome when the MTT differs between the normal and malignant tissue [33] and if the GBCA induced $T_1$ signal enhancement is larger than 30% [34]. Accordingly, a more robust and sophisticated post processing method is wanted for optimal leakage correction.

## 1.7. Research goals

The primary objective of this dissertation is to develop methodologies for perfusion MRI that address the above-mentioned challenges.

A first aim is to enhance the accuracy and precision of cerebral perfusion

parameters estimated through DSC MRI. I hypothesize that this can be achieved by substituting the conventional DSC-derived AIF with an AIF derived from DCE MRI. In a detailed investigation I will compare the DCE-derived AIF against versions obtained from DSC MRI. Furthermore, perfusion coefficients computed with the conventional DSC AIF will be compared with those calculated using the DCE-derived AIF.

A second goal is to refine AIF measurement from DCE MRI by mitigating adverse influences, specifically addressing the inflow effect and PVE. I will assess the impacts of these confounding factors on the accuracy of DCE AIF measurement through mathematical analysis and simulation studies. Furthermore, I will introduce a method for simultaneously correcting both the inflow effect and PVE, potentially advancing the accuracy of AIF determination in DCE MRI.

The third aim is to improve the correction of leakage effects on parameter estimation in DSC analysis. Leveraging a unique dataset combining DCE and DSC MRI, I will exploit the leakage estimation from DCE MRI for a new correction approach in DSC analysis. The effectiveness of this novel approach will be benchmarked against existing algorithms.

## 1.8. OUTLINE

This dissertation is structured to systematically address the above research challenges and objectives.

In **Chapter 2**, I provide a review of the clinical application of DCE and DSC MRI in patients with glioma. It provides a concise overview of the theoretical foundations, imaging and analysis procedures, and inherent limitations of practically applied methods. Additionally, this chapter discusses the current clinical consensus on the use of perfusion MRI techniques.

**Chapter 3** contains an analysis of AIFs derived from DCE and DSC MRI, relying on consecutive DCE-DSC imaging sequence. A conventional, semi-automatic algorithm is applied to identify the AIF, which is solely based on signal characteristics, bypassing the need for anatomical cues. Furthermore, the potential of employing an AIF from the DCE series as input for the DSC analysis is explored, juxtaposing this approach against conventional DSC based AIF selection techniques.

**Chapter 4** studies the analogous impacts of inflow effects and PVEs on AIF measurements in DCE MRI. Through theoretical analyses and numerical simulations, I assess the feasibility of concurrently mitigating these influences. This newly proposed method is implemented, leveraging an estimated number of pulses experienced by spins in blood to remove the artefacts introduced both by inflow effects and PVE.

In **Chapter 5**, I focus on the development of a novel leakage correction technique for DSC analysis. Utilizing vascular permeability maps and tissue

contrast concentration data from DCE MRI, this method seeks to precisely correct for leakage effects on the DSC parameters estimations. The efficacy of this approach is evaluated against a commercially available method, facilitating a direct comparison of outcomes.

**Chapter 6** offers a comprehensive discussion of my findings, highlighting the strengths and potential limitations of the methodologies introduced. Additionally, I also describe challenges and suggest future directions of research in the field, underscoring the ongoing need for innovation and refinement in perfusion MRI techniques.

# REFERENCES


[1] H. B. W. Larsson *et al.* "Quantitation of blood-brain barrier defect by magnetic resonance imaging and gadolinium-DTPA in patients with multiple sclerosis and brain tumors". In: *Magnetic Resonance in Medicine* 16.1 (Oct. 1990), pp. 117–131. ISSN: 0740-3194. DOI: 10.1002/mrm.1910160111.

[2] P. S. Tofts and A. G. Kermode. "Measurement of the blood-brain barrier permeability and leakage space using dynamic MR imaging. 1. Fundamental concepts". In: *Magnetic Resonance in Medicine* 17.2 (Feb. 1991), pp. 357–367. ISSN: 0740-3194. DOI: 10.1002/mrm.1910170208.

[3] E. R. Kandel *et al. Principles of neural science*. Vol. 4. New York: McGraw-hill, 2000, pp. 1227–1446.

[4] D. Fukumura *et al.* "Hypoxia and acidosis independently up-regulate vascular endothelial growth factor transcription in brain tumors in vivo." In: *Cancer research* 61.16 (Aug. 2001), pp. 6020–4. ISSN: 0008-5472.

[5] P. S. Tofts *et al.* "Estimating kinetic parameters from dynamic contrast-enhanced t1-weighted MRI of a diffusable tracer: Standardized quantities and symbols". In: *Journal of Magnetic Resonance Imaging* 10.3 (Sept. 1999), pp. 223–232. ISSN: 1053-1807. DOI: 10.1002/(SICI)1522-2586(199909)10:3<223::AID-JMRI2>3.0.CO;2-S.

[6] N. Zhang *et al.* "Correlation of volume transfer coefficient K-trans with histopathologic grades of gliomas". In: *Journal of Magnetic Resonance Imaging* 36.2 (Aug. 2012), pp. 355–363. ISSN: 1053-1807. DOI: 10.1002/jmri.23675.

[7] J. P. B. O'Connor *et al.* "DCE-MRI biomarkers in the clinical evaluation of antiangiogenic and vascular disrupting agents". In: *British Journal of Cancer* 96.2 (Jan. 2007), pp. 189–195. ISSN: 0007-0920. DOI: 10.1038/sj.bjc.6603515.

[8] J. Yang *et al.* "MR imaging biomarkers evaluating vascular normalization window after anti-vessel treatment". In: *Oncotarget* 9.15 (Feb. 2018), pp. 11964–11976. ISSN: 1949-2553. DOI: 10.18632/oncotarget.22600.

[9] L. Østergaard. "Principles of cerebral perfusion imaging by bolus tracking". In: *Journal of Magnetic Resonance Imaging* 22.6 (Dec. 2005), pp. 710–717. ISSN: 1053-1807. DOI: 10.1002/jmri.20460.

[10] K. Zierler. "Indicator dilution methods for measuring blood flow, volume, and other properties of biological systems: a brief history and memoir." In: *Annals of biomedical engineering* 28.8 (Aug. 2000), pp. 836–48. ISSN: 0090-6964. DOI: 10.1114/1.1308496.

[11] J. R. Petrella and J. M. Provenzale. "MR Perfusion Imaging of the Brain". In: *American Journal of Roentgenology* 175.1 (July 2000), pp. 207–219. ISSN: 0361-803X. DOI: 10.2214/ajr.175.1.1750207.

[12] A. Romano *et al.* "Clinical applications of dynamic susceptibility contrast perfusion-weighted MR imaging in brain tumours". In: *La radiologia medica* 117.3 (Apr. 2012), pp. 445–460. ISSN: 0033-8362. DOI: 10.1007/s11547-011-0715-4.

[13] R. Fu *et al.* "Diagnostic performance of DSC perfusion MRI to distinguish tumor progression and treatment-related changes: a systematic review and meta-analysis". In: *Neuro-Oncology Advances* 4.1 (Jan. 2022). ISSN: 2632-2498. DOI: 10.1093/noajnl/vdac027.

[14] J. L. Boxerman *et al.* "The Role of Preload and Leakage Correction in Gadolinium-Based Cerebral Blood Volume Estimation Determined by Comparison with MION as a Criterion Standard". In: *American Journal of Neuroradiology* 33.6 (June 2012), pp. 1081–1087. ISSN: 0195-6108. DOI: 10.3174/ajnr.A2934.

[15] M. J. P. Van Osch *et al.* "Measuring the arterial input function with gradient echo sequences". In: *Magnetic Resonance in Medicine* 49.6 (June 2003), pp. 1067–1076. ISSN: 0740-3194. DOI: 10.1002/mrm.10461.

[16] E. Akbudak, M. Kotys, and Conturo T. "Quadraticity and haematocrit dependence of ΔR2* AIF signals at 3T: a blood phantom study under physiologic conditions. Syllabus of the ISMRM workshop on quantitative cerebral perfusion imaging using MRI; a technical perspective." In: *Syllabus of the ISMRM workshop on quantitative cerebral perfusion imaging using MRI; a technical perspective*. Venice, 2004.

[17] M. J. P. Van Osch *et al.* "Correcting partial volume artifacts of the arterial input function in quantitative cerebral perfusion MRI". In: *Magnetic Resonance in Medicine* 45.3 (Mar. 2001), pp. 477–485. ISSN: 0740-3194. DOI: 10.1002/1522-2594(200103)45:3<477::AID-MRM1063>3.0.CO;2-4.

[18] M. Ebinger *et al.* "Reliable perfusion maps in stroke MRI using arterial input functions derived from distal middle cerebral artery branches." In: *Stroke* 41.1 (Jan. 2010), pp. 95–101. ISSN: 1524-4628. DOI: 10.1161/STROKEAHA.109.559807.

[19] M. Rausch *et al.* "Analysis of input functions from different arterial branches with gamma variate functions and cluster analysis for quantitative blood volume measurements." In: *Magnetic resonance imaging* 18.10 (Dec. 2000), pp. 1235–43. ISSN: 0730-725X. DOI: 10.1016/s0730-725x(00)00219-8.

[20] A. E. Hansen *et al.* "Partial volume effect (PVE) on the arterial input function (AIF) in T1-weighted perfusion imaging and limitations of the multiplicative rescaling approach". In: *Magnetic Resonance in Medicine* 62.4 (Oct. 2009), pp. 1055–1059. ISSN: 07403194. DOI: 10.1002/mrm.22098.

[21] J. U. Harrer *et al.* "Comparative study of methods for determining vascular permeability and blood volume in human gliomas". In: *Journal of Magnetic Resonance Imaging* 20.5 (Nov. 2004), pp. 748–757. ISSN: 10531807. DOI: 10.1002/jmri.20182.

[22] V. C. Keil *et al.* "Effects of arterial input function selection on kinetic parameters in brain dynamic contrast-enhanced MRI". In: *Magnetic Resonance Imaging* 40 (July 2017), pp. 83–90. ISSN: 0730725X. DOI: 10.1016/j.mri.2017.04.006.

[23] M. J. Thrippleton *et al.* "Quantifying blood-brain barrier leakage in small vessel disease: Review and consensus recommendations". In: *Alzheimer's & Dementia* 15.6 (June 2019), pp. 840–858. ISSN: 1552-5260. DOI: 10.1016/j.jalz.2019.01.013.

[24] S. P. Cramer *et al.* "Reproducibility and Optimal Arterial Input Function Selection in Dynamic Contrast-Enhanced Perfusion MRI in the Healthy Brain". In: *Journal of Magnetic Resonance Imaging* (Aug. 2022). ISSN: 1053-1807. DOI: 10.1002/jmri.28380.

[25] C. Roberts *et al.* "The effect of blood inflow and B(1)-field inhomogeneity on measurement of the arterial input function in axial 3D spoiled gradient echo dynamic contrast-enhanced MRI." In: *Magnetic resonance in medicine* 65.1 (Jan. 2011), pp. 108–19. ISSN: 1522-2594. DOI: 10.1002/mrm.22593.

[26] M. K. Ivancevic *et al.* "Inflow effect correction in fast gradient-echo perfusion imaging". In: *Magnetic Resonance in Medicine* 50.5 (Nov. 2003), pp. 885–891. ISSN: 07403194. DOI: 10.1002/mrm.10633.

[27] A. Garpebring *et al.* "Effects of inflow and radiofrequency spoiling on the arterial input function in dynamic contrast-enhanced MRI: a combined phantom and simulation study." In: *Magnetic resonance in medicine* 65.6 (June 2011), pp. 1670–9. ISSN: 1522-2594. DOI: 10.1002/mrm.22760.

[28] A. Garpebring *et al.* "Phase-based arterial input functions in humans applied to dynamic contrast-enhanced MRI: potential usefulness and limitations". In: *Magnetic Resonance Materials in Physics, Biology and Medicine* 24.4 (Aug. 2011), pp. 233–245. ISSN: 0968-5243. DOI: 10.1007/s10334-011-0257-8.

[29] R. Materne *et al.* "Assessment of hepatic perfusion parameters with dynamic MRI". In: *Magnetic Resonance in Medicine* 47.1 (Jan. 2002), pp. 135–142. ISSN: 0740-3194. DOI: 10.1002/mrm.10045.

[30] J. Ning *et al.* "Vascular input function correction of inflow enhancement for improved pharmacokinetic modeling of liver DCE-MRI". In: *Magnetic Resonance in Medicine* 79.6 (June 2018), pp. 3093–3102. ISSN: 07403194. DOI: 10.1002/mrm.26988.

[31] C. C. Quarles, B. D. Ward, and K. M. Schmainda. "Improving the reliability of obtaining tumor hemodynamic parameters in the presence of contrast agent extravasation". In: *Magnetic Resonance in Medicine* 53.6 (June 2005), pp. 1307–1316. ISSN: 0740-3194. DOI: 10.1002/mrm.20497.

[32] J. L. Boxerman, K. M. Schmainda, and R. M. Weisskoff. "Relative cerebral blood volume maps corrected for contrast agent extravasation significantly correlate with glioma tumor grade, whereas uncorrected maps do not." In: *AJNR. American journal of neuroradiology* 27.4 (Apr. 2006), pp. 859–67. ISSN: 0195-6108.

[33] R. Leigh *et al.* "Arrival Time Correction for Dynamic Susceptibility Contrast MR Permeability Imaging in Stroke Patients". In: *PLoS ONE* 7.12 (Dec. 2012), e52656. ISSN: 1932-6203. DOI: 10.1371/journal.pone.0052656.

[34] R. Haselhorst *et al.* "Dynamic susceptibility contrast MR imaging of plaque development in multiple sclerosis: Application of an extended blood-brain barrier leakage correction". In: *Journal of Magnetic Resonance Imaging* 11.5 (May 2000), pp. 495–505. ISSN: 1053-1807. DOI: 10.1002/(SICI)1522-2586(200005)11:5<495::AID-JMRI5>3.0.CO;2-S.

# 2

# Perfusion MR Techniques for Preoperative Glioma Characterization

This chapter is a condensed version of the published paper:
Hirschler, L., Sollmann, N., Schmitz-Abecassis, B., ... , **Tseng, C.-H.**, et al. (2023), Advanced MR Techniques for Preoperative Glioma Characterization: Part 1. J Magn Reson Imaging, 57: 1655-1675. https://doi.org/10.1002/jmri.28662

## ABSTRACT

Preoperative clinical MRI protocols for gliomas, brain tumors with dismal outcomes due to their infiltrative properties, still rely on conventional structural MRI, which does not deliver information on tumor genotype and is limited in the delineation of diffuse gliomas. The Glioma MR Imaging 2.0 group of the European Cooperation in Science and Technology wants to raise awareness about the state-of-the-art advanced MRI techniques in gliomas and their possible clinical translation or lack thereof. This review describes current methods, limits, and applications of dynamic susceptibility contrast and dynamic contrast enhanced MRI for the preoperative assessment of glioma, summarizing the level of clinical validation of two techniques.

## 2.1. INTRODUCTION

Gliomas are a heterogeneous group of neuroepithelial tumors arising from the glial cells, with an age-adjusted average rate of 6.03 per 100,000 population [1]. Traditionally, they are divided according to a four-step grading system where a higher grade represents disease with more malignant features and a mostly dismal prognosis. The traditional concept of the World Health Organization (WHO) grading system based on histopathological assessment underwent significant changes in the fifth edition of the WHO Classification of Tumors of the Central Nervous System (CNS), published in 2021 [2]. This current classification introduced revisions to tumor nomenclature and advances the integral role of molecular diagnostics for tumor classification and grading that predicts the prognosis better [3] than the previous 2016 version [4].



Compared with the 2016 version, the WHO 2021 classification incorporates more molecular alterations into the diagnostics and divides gliomas into adult-type diffuse gliomas, pediatric-type diffuse low-grade (LGG) and high-grade (HGG) gliomas, circumscribed astrocytic gliomas, glioneuronal and neuronal tumors, and ependymal tumors. The primary genetic markers used for glioma taxonomy are now considered isocitrate dehydrogenase (IDH) 1 and 2 mutation status, 1p/19q co-deletion, H3F3A alterations, ATRX gene mutations, O6-Methylguanine-DNA Methyltransferase (MGMT) promoter methylation status, loss of CDKN2A, epidermal growth factor receptor (EGFR) amplification, a combined gain of chromosome 7 and loss of chromosome 10, and TERT promoter pathogenic variants. In adults, the term glioblastoma is now reserved only for IDH-wildtype tumors and will always be graded as 4, whereas IDH-mutated astrocytomas present a distinct progressive disease with WHO grade rising from 2 to 4. As a third class, oligodendrogliomas are now distinct from astrocytomas by possessing both IDH mutation and 1p/19q co-deletion and can range form grade 2 to 4 as well. As the genetic profile of a particular tumor affects its metabolic pathways leading to a certain product or a change in the cell's phenotype, advanced MRI techniques can be a very promising noninvasive approach to predict glioma type and behavior.

Preoperative glioma imaging by MRI is essential to localize and delineate the tumor volume and to assess infiltrative behavior or compressive effects on adjacent structures with related complications. The minimal recommendation for such routine structural imaging protocols at 3T consists of $T_1$-weighted imaging (before and after the administration of gadolinium-based contrast agents (GBCA), 1 mm isotropic resolution), $T_2$-weighted imaging (after GBCA administration, < 3 mm slice thickness), $T_2$-weighted fluid-attenuated inversion recovery (FLAIR) imaging (< 3 mm slice thickness), and diffusion-weighted imaging (< 3 mm slice thickness, b-values of 0, 500, and 1000 s/mm$^2$), with further details to be found in Ellingson et al [5].

With the advent of advanced sequences, quantitative imaging of multiple pathophysiological features in the tumor and surrounding tissue became possible [6, 7], providing the opportunity to noninvasively characterize different molecular types of glioma against the background of the WHO 2021 classification [6, 8].

While glioma genotyping based on tissue probes derived from neurosurgical tumor resection or biopsy remains the standard, predicting genotypes by preoperative advanced MRI could aid in clinical decision-making and facilitate individual management tailored to the individual tumor characteristics [6, 9].

In most clinical settings for preoperative glioma assessment, however, only conventional MRI is performed. The untapped potential of advanced MRI seems related to a multitude of obstacles that prevent its wider translation into the clinical routine [10]. A major hurdle is the lack of rigorous validation of advanced MRI-derived biomarkers. Although recommendations for the acceleration of imaging biomarker development in cancer, both for lesion segmentation and imaging biomarker quantification, do exist, almost no regulatory qualifications or specific guidelines of high quality have been adopted [11–13]. Finally, advanced sequences beyond conventional structural MRI may require special hardware and/or software combined with the need for dedicated expertise for acquisition, post-processing, and evaluation [14]. This makes advanced imaging of gliomas time-consuming, often involving manual data handling and dedicated, custom-made processing pipelines.

The purpose of this chapter is to raise awareness and contribute to clinical translations of contrast agent based perfusion MRI techniques, specifically dynamic susceptibility contrast (DSC) and dynamic contrast enhanced (DCE) MRI, by describing the methods and applications for the preoperative assessment of glioma, and summarizing whether these techniques can be routinely used. For each technique, we aimed to provide a concise methodological overview, review the strengths and weaknesses of glioma characterization and tumor heterogeneity mapping, and use this as the basis for assessing the level of technical readiness of each method.

## 2.2. METHODS

This review was initiated through the European Cooperation in Science and Technology (COST) Glioma MR Imaging 2.0 (GliMR) initiative [10], which brought together clinicians, engineers, and physicists with expertise in advanced MRI techniques applied to brain tumor imaging in a series of virtual and onsite meetings from July 2020 through September 2022. We defined the target audience of this review as clinicians (eg, neuroradiologists, neurosurgeons, and (neuro-)oncologists) and researchers without deep knowledge of advanced MRI who want to broaden their routine or experimental protocols for brain tumor imaging. We used the GliMR consortium's technical expertise to aggregate the available evidence and level of validation for cutting-edge MRI methods and the information derivable from these.

These advanced MRI techniques allow (semi)quantitative imaging of tumor composition, metabolism, physiology, or mechanical properties that are not captured in routine clinical protocols. At the same time, we included only acquisition, reconstruction, and postprocessing methods that have already

demonstrated pilot results in brain tumors.

The reviews for the two perfusion techniques were designed to include the following:

- An Overview of the technique with links to detailed reviews and recommendations for implementation and use;
- An overview of the current evidence about the clinical application to brain tumor imaging, focusing on how it can be used for glioma characterization and grading according to the new WHO 2021 classification criteria and its focus on molecular characteristics to distinguish between different molecular glioma subtypes;
- A statement on the level of clinical and technological validation of the method, summarizing the current status and the prospect for near-future improvements;
- A summary of the recommended use.



## 2.3. RESULTS

### 2.3.1. DSC MRI

#### OVERVIEW

DSC MRI entails the acquisition of $T_2$ or $T_2^*$-weighted images with a high temporal resolution during which a GBCA is bolus-injected. A gradient-echo echo planar imaging (GRE-EPI) sequence, heavily $T_2^*$-weighted, is most often used. With GBCA confined to the vessels, as for the brain with an intact blood-brain barrier (BBB), a gradient of susceptibility between the intra- and extravascular tissue is induced, causing a transient shortening of the dynamic $T_2^*$-weighted signal (S(t)). The S(t) is converted into the relaxation rate change ($\Delta R_2^*(t)$), which, when integrated, provides a voxelwise estimate of the relative cerebral blood volume (rCBV) (relative to the rest of the brain). In addition, voxelwise cerebral blood flow (CBF) can be estimated if the $\Delta R_2^*(t)$ from large arteries (i.e., the arterial input function (AIF)) is also separately measured and used, along with the tissue $\Delta R_2^*(t)$. Since rCBV is the most common DSC MRI parameter used to evaluate brain tumors (Figure 2.1), the remaining discussion will focus on rCBV.

Estimation of rCBV can be confounded by the extravasation of GBCA through a disrupted BBB, a common condition in brain tumors. While this "leakage effect" violates the assumption of GBCA vascular compartmentalization, DSC MRI can still be successfully used to estimate brain tumor rCBV if this leakage effect is appropriately considered [15–17]. A recent consensus on DSC MRI data acquisition for brain tumors resulted in two recommended approaches [18]. The first, and most robust approach incorporates a GBCA pre-dose to diminish $T_1$ leakage effects that might occur during the subsequent DSC MRI acquisition. A second GBCA dose is administered during the collection of the DSC MRI data, using either a low (30°) or intermediate (60°) flip angle and field strength-dependent echo times

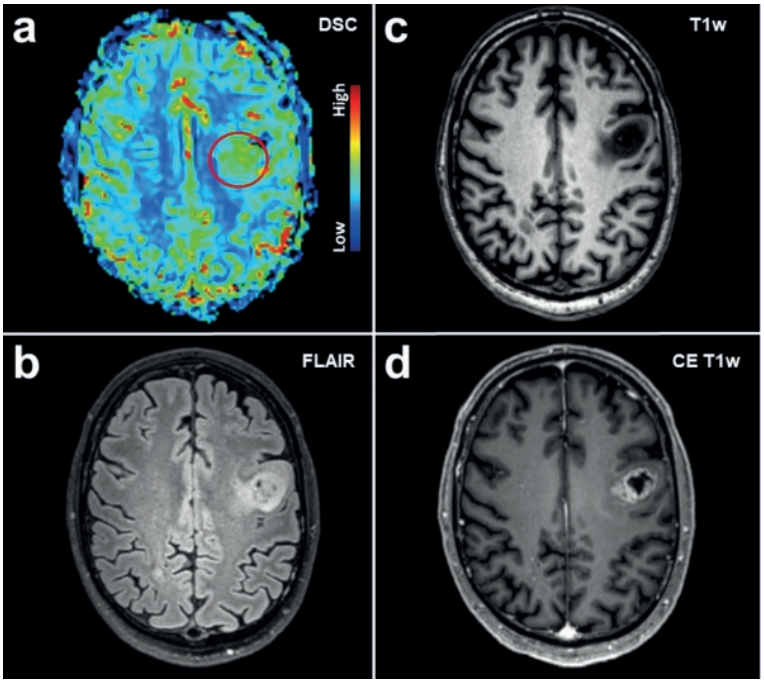


Figure 2.1: Elevated perfusion according to DSC MRI (a) in a 55-year-old male patient with a left frontal HGG that showed high signal on FLAIR; b) imaging and contrast enhancement on $T_1$-weighted imaging (c, axial non-contrast, and d, axial contrast-enhanced images). The borders of the lesion with contrast-enhancing tumor parts, in particular, showed hyperperfusion on DSC MRI (red circle, a).

(TEs) (40–50 msec at 1.5T, 25–35 msec at 3T). The second approach has the advantage of not requiring a GBCA pre-dose while using a low flip angle (30°) and field-strength-dependent TEs (1.5T: 40–50 msec; 3T: 25–35 msec). For both approaches, a repetition time (TR) = 1000–1500 msec is recommended, and the inclusion of a post-processing, the contrast-agent leakage correction method is required. While the Boxerman-Schmainda-Weiskoff (BSW) method [16] for leakage correction is most commonly used, other methods have also been proposed [19–21].

### CLINICAL APPLICATION

Studies have shown that rCBV ratios can predict glioma grade [15, 22–24] and are able to stratify patients into low, intermediate, and high-risk groups, with shorter survival corresponding to higher rCBV [25]. Both intra-tumoral and peri-tumoral rCBV were shown to be reliable for the preoperative distinction of HGG from LGG with excellent sensitivity and accuracy [26]. Similarly, delineations of pre-operative

rCBV "habitats" within both contrast-enhancing and peritumoral regions were found to be highly prognostic for patients who underwent standard-of-care treatment [27].

Possibly, one of the most significant roles of pre-operative rCBV is to assist with ensuring an accurate diagnosis as the heterogeneity of gliomas can lead to misdiagnosis and undergrading. Brain tumor rCBV has been shown helpful in identifying such cases retrospectively [25], or preferably, both can be avoided altogether by identifying the best sites for surgical biopsy [28]. In a more recent case report [29], rCBV class maps (referred to as fractional tumor burden maps), which delineate regions of low, intermediate, and high vascularity (Figure 2.2), confirmed that tissue obtained from areas of zero to low rCBV received a histopathologic diagnosis of non-tumor while the remaining unresectable tissue, with a high pre-operative rCBV, was the site of early and aggressive recurrence. Thus, knowledge of the spatial variation in rCBV in both resected and the remaining tissue is fundamental for an accurate diagnosis and follow-up treatment management.

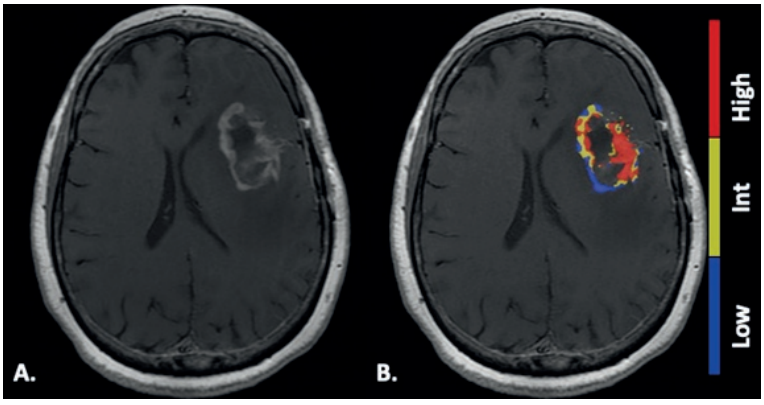


Figure 2.2: Patient with recurrent glioblastoma. A) $T_1$-weighted MRI with CE, B) corresponding map of fractional tumor burden (FTB) showing regions of zero-low (blue), intermediate (yellow), and high rCBV (red)within the contrast agent enhancing region.

Pre-operative rCBV may also play an important role in the success of the 2016 WHO classification that newly includes molecular markers. Despite the known heterogeneities, at both the cellular and molecular levels, patient stratification and treatment are generally determined on the basis of molecular markers present in a single tumor specimen. As a result, the power of this new classification is being profoundly underutilized and may explain why, even with the advances of molecular profiling, the improvements in patient outcome have been modest [30]. As a potential solution, rCBV was able to predict differences in IDH1 mutation and MGMT status [31], and tissue from hypercellular and hypervascular microfoci revealed greater expression of Ki-67, HIF-1a, CD31, and EGFR compared to tumor

background [32]. Therefore, rCBV has the potential to guide surgical biopsy and provide a more accurate diagnosis for both histopathological and molecular analyses.



### VALIDATION

Existing evidence reveals that rCBV is a valuable, and even necessary adjunct to standard MRI. Yet, it has been argued that rCBV remains limited in its clinical adoption due to a lack of standardization, which may explain the variability in reported rCBV thresholds [33]. Still, in recent years several well-curated studies have demonstrated excellent repeatability, cross-site consistency, and market availability, suggesting a high technology readiness level for rCBV.

With DSC MRI data collected twice within 8 days, in HGG patients, rCBV was found to be highly repeatable [34]. The within-patient coefficient of variation was further reduced when using a standardization algorithm that precluded the need for a user-defined reference region, which is required to normalize rCBV to normal brain values. Similar results were found in a multi-site clinical trial, for which rCBV repeatability was again shown to be excellent with standardized rCBV more repeatable than normalized rCBV [35].

With multi-site analysis of a shared DSC MRI dataset, but using several different analysis platforms, rCBV was also able to distinguish high-grade from low-grade glioma in all cases [36]. Moreover, a single threshold, applicable to all platforms, could be identified. This study further suggested that much of the previous variability in reported thresholds may be due to differences in data pre-processing, patient populations, or image acquisition settings, variables that were held fixed in this multi-site study. Moreover, widespread implementation of the recommended acquisition protocol [18] could greatly improve consistency in reported rCBV data, including thresholds by which to distinguish tumor grades. Indeed, two independent sites, using the same acquisition and post-processing methods, were able to arrive at the same threshold to distinguish tumor from treatment effect, validated with spatially matched biopsies [37, 38].

Finally, FDA-cleared and CE-marked platforms for the analysis of rCBV data are now widely available, with studies published that compared platforms [36, 39, 40]. Using one such platform, the ease-of-use and ability to collect and analyze multi-site rCBV data were demonstrated by incorporation into clinical trials, with each showing the utility of rCBV to predict outcomes [35, 41, 42].

Challenges that remain for DSC MRI include optimization of the imaging method itself. For example, GRE-EPI can experience signal dropout in regions near air-tissue interfaces, bone, or resection cavities, making it difficult to evaluate tumors in these regions fully. Technical improvements that enable higher spatial resolution imaging and reduced sensitivity, or correction of the unwanted susceptibility effects, are needed. Also, GRE-EPI retains a high sensitivity to large normal vessels, which can make it difficult to evaluate tumor-specific vascularity in these regions. Approaches that combine GRE-EPI and SE-EPI [15, 17, 24, 43] may

be a solution, as this could offer images with differing vessel size sensitivity and a more complete interpretation. However, such sequences are not yet available for clinical use. Finally, the high temporal resolution required for DSC MRI often precludes whole-brain imaging. Newer methods that incorporate advances in parallel and simultaneous multi-slice imaging may offer a solution [44].



#### SUMMARY

The collection of pre-operative DSC MRI data with the generation of rCBV maps is easy to obtain and has been shown to be invaluable for the diagnosis and treatment management of glioma. Full clinical adoption should be accelerated with the recent consensus recommendation for DSC MRI data acquisition and convergence of analysis methods, thus overcoming previous concerns regarding standardization. The remaining issues include improving image quality and coverage.

### 2.3.2. DCE MRI

#### OVERVIEW

DCE MRI is a perfusion technique that monitors the GBCA-induced $T_1$-shortening effect in blood plasma and tissue, if leakage occurs. The signal records mixed information about blood perfusion, vessel permeability, and a fraction of extracellular extravascular space (EES), and is often used to characterize tumor microvasculature. The signal can be assessed semi-quantitatively by evaluating the contrast arrival time, time to the peak, maximum intensity, the area under the curve, wash-in slope, and wash-out rate. Alternatively, a quantitative analysis is achieved by applying tracer kinetic models [45]. The most frequently applied model in tumor assessment is the extended Tofts model, which asserts that the contrast tracer distributes over two compartments: the intravascular space and the EES, with a bi-directional exchange of the tracer across the blood vessel wall [46]. The model enables numerical estimation of the volume transfer constant between the blood plasma and the EES ($K^{trans}$), the reflux exchange rate from the EES to the blood plasma ($K_{ep}$), the volume fraction of plasma ($v_p$), and the volume fraction of EES ($v_e$) (Figure 2.3). The volume transfer constant, $K^{trans}$, which reflects the vascular permeability, is the most often applied DCE parameter in the context of glioma [47]. General guidelines for applying DCE imaging in pre-clinical research have been summarized in multiple papers [48, 49].

#### CLINICAL APPLICATION

Malignant gliomas are characterized by a remarkable increase in blood vessel formation (angiogenesis) which leads to aberrant vascular structure, abnormal blood flow, and increased permeability in vessels. DCE-driven parameters were investigated to be potential markers of angiogenic activity in gliomas and are therefore being used for tumor monitoring [51]. An extended systematic review [52] summarized 14 studies about the discrimination between LGGs and HGGs and five studies about the differentiation between primary CNS lymphomas and

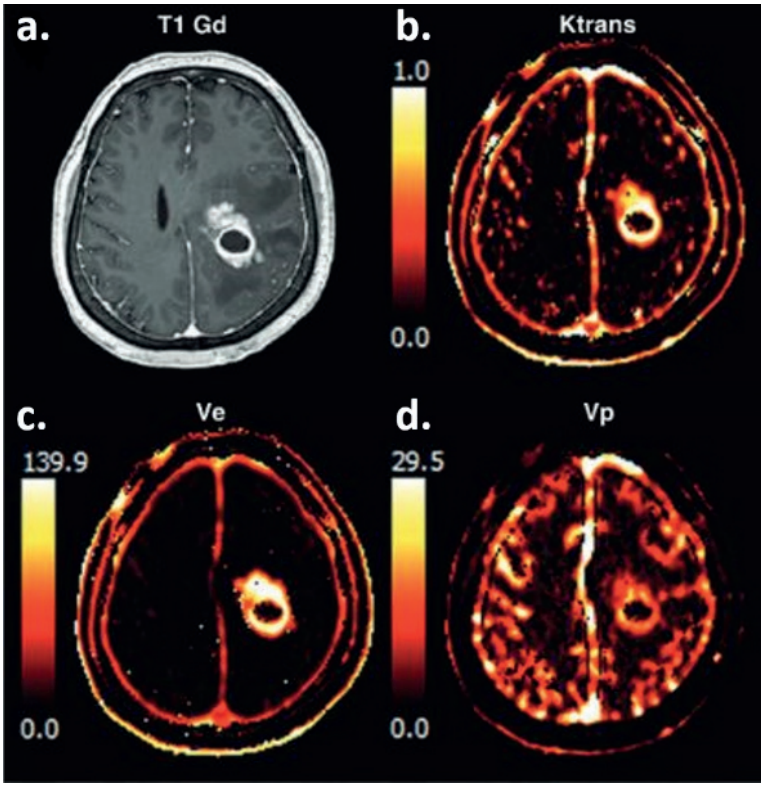


Figure 2.3: The contrast-enhanced $T_1$-weighted image (a) and DCE-derived vascular parameter maps: $K^{trans}$ (b), $v_e$ (c), and $v_p$ (d) of a glioblastoma patient treated with concurrent radiation therapy and temozolomide chemotherapy [50].

HGGs based on DCE parameters. The paper concluded that all these studies demonstrated considerable specificity and sensitivity in relation to the studied aspects, showing high diagnostic accuracy in discriminating between LGGs and HGGs (AUC 0.96) and slightly lower performance for discriminating between primary CNS lymphomas and HGGs (AUC 0.86).

Moreover, studies revealed that DCE-driven parameters were able to predict some of the molecular characteristics used recently for the classification of glioma tumors, including IDH and MGMT methylation. Hu et al reported statistically significant differences in histogram parameters of $K^{trans}$ and $v_e$ between IDH-mutated and IDH-wild-type glioma [53]. Furthermore, Zhang et al found that glioblastoma with MGMT methylation showed significantly higher $K^{trans}$, indicating that MGMT methylation may be involved in glioma-associated angiogenesis characterized by high endothelial permeability vasculatures [47]. The prognostic value of DCE parameters has also been studied, with some studies

showing higher $K^{trans}$ and $v_e$ to be associated with worse overall survival (OS), and Ulyte et al showing that high $v_e$ is a consistent predictor of worse progression-free survival and OS in HGG patients [54].



### VALIDATION

DCE MRI has been studied for over three decades. An overwhelming amount of papers have demonstrated the importance of DCE MRI for diagnosis, prognosis, and therapy monitoring in glioma patients. However, one limitation is that the DCE parameters may vary across vendors and systems, hindering cross-center comparison. The variability of DCE parameters results from several factors including different field strengths, imaging principles, sequence settings, and analysis software. Kim has discussed the sources of variability in quantitating DCE parameters and proposed several possible solutions [55]. Hence, a consensus for the implementation of DCE imaging with reduced bias across multi-centers is still needed to facilitate the integration of the DCE technique into standard-of-care imaging in the clinic.

The selection of pharmacokinetic models is also a key factor that influences the DCE parameters. Complex models with fewer assumptions are physiologically more reliable than simpler models, which often make assumptions to constrain the model. Such assumptions may not be appropriate and could bias estimated parameters from the model. Conversely, complex models are more sensitive to noise than simpler models [56].

### SUMMARY

Preclinical and clinical studies have shown that the quantitative DCE MRI parameters could be image biomarkers in glioma imaging. However, it is not yet possible to use DCE MRI as a regular tool in the clinic due to the variability resulting from differences in scanners, sequences, and software. Besides, improving the acquired DCE image quality would facilitate the implementation of complex models, which are more realistic in pathological conditions, and further provides more reliable and precise DCE parameters.

## 2.4. DISCUSSION

In this review, we has summarized the evidence for clinical use of contrast-based perfusion MRI for preoperative glioma characterization.

DSC is an exemplary case of accelerating the clinical translation of advanced MRI. DSC involves contrast-agent injection, input function delineation, tracer-kinetic modeling, and value normalization. Despite its complexity, DSC is commonly used in glioma imaging[14] owing mainly to the extensive work invested in DSC validation. This work culminated recently by introducing consensus recommendations[18], which provide clear instructions on the measurement and evaluation processes and is backed up by robust validation. Such recommendations

constitute an important step toward clinical acceptance and are missing for nearly all other advanced MRI techniques.

The level of clinical validation also depends on more general determinants. Glioma is a relatively rare disease, making it difficult to collect enough data for statistically robust assessments. The Brain Tumor Segmentation (BraTS) repository initiative partly addresses this by collecting multi-institutional pre-operative multi-parametric MRI scans of patients with glioma [57]. Still, regardless of the level of good-quality evidence, lack of widespread use may boil down to something as simple as limited demand and early adoption from key practitioners due to preference, education, and above all awareness. With increasing demand, shorter time to read exams, and reduced hospital budgets, it may be difficult for the radiologist or end user to stay up to date with the wide range of available methods, or find the time and resources to lead the clinical implementation. For any new technique, adaptation and priority of use will be weighed against the cost and resources of the exam, its associated clinical workup, and the initial implementation and training of bioengineers and neuroradiologists. In practice, this may be a question of healthcare reimbursement policies and insurance coverage, which usually do not include techniques that are not part of the guidelines. Several initiatives are trying to make up for this difference by reviewing the abilities of advanced MRI6; building networks of professionals in glioma imaging, providing educational resources and processing tools for advanced MRI, and connecting with other professionals in neuro-oncology as in GliMR [10]; working on providing open source software for data analysis like the Open Science Initiative For Perfusion Imaging (OSIPI) [58]; or seeking to improve the practical value of quantitative imaging biomarkers as the Quantitative Imaging Biomarkers Alliances (QIBA) does [59].

Despite the promise of improved diagnostic efficiency of the new imaging biomarkers, clinical translation will need to respect the cost–benefit ratio of its use and the patient's health status. This translates to keeping the acquisition duration mostly unchanged and replacing old sequences with newer ones only if the added value compensates for the hurdles associated with introducing new techniques. For example, while DCE measures both the permeability of the BBB and vascularization and is potentially more useful than DSC, it is not straightforward to measure both sequences within a single session. Therefore, DSC is currently prioritized as a quicker and more robust technique that already has well-established guidelines and a much higher level of validation. Overall, GBCA use in gliomas is likely to be reduced in the future due to added burden to costs, logistics, and patient discomfort burdens, as well as safety issues raised by both American and European pharmacological safety agencies. arterial spin labeling (ASL) [60], BBB-ASL [61], and machine-learning-based techniques are on a good path to complement and maybe eventually replace DSC, DCE, and post-contrast $T_1$-weighted scans, respectively, in many glioma patients and especially children.

Even when advanced diagnostic tools are implemented and available to the end user, their clinical use is challenged by an inherent paradox. As imaging techniques

become more advanced, so do their resulting imaging biomarkers, where any metric will move away from a simple binary (yes/no) or cutoff (above/below) value for characterization. With a higher-level technique, the complex biology and function of cancer will arguably be assessed in a more accurate and unique way, but at the cost of more difficult interpretations. Multi-parametric assessment combining several advanced MRI techniques may also further improve glioma characterization and reduce the bias of any single technique toward certain biological or functional properties of the tissue. However, a multi-parametric approach will also add to the complexity of the analysis. As a result, in a busy practice there may be no time, nor may it be technically feasible, for radiologists to process this data. For advanced imaging methods to be widely adopted, a strong focus is required on translating clinically ready technology into commercial software directly embedded in the hospital-wide picture archiving and communication system (PACS). This will allow for standardization and start-to-end automatic pipelines as an alternative to laborious and user-dependent alternatives.

In conclusion, effective treatment of gliomas is still an unmet clinical need that is, in part, reflected by their wide-ranging intra- and inter-individual biological heterogeneity. Targeted therapy, which has demonstrated promising results in other cancers, has largely failed in gliomas. To address this challenge, the perfusion MRI techniques hold the potential to support better clinical decisions for tumor characterization and subsequent treatment. By focusing on what they are currently missing to advance their clinical readiness level, the imaging community can help make advanced MRI for glioma diagnosis and therapy clinically available, personalized, and effective.

# REFERENCES


[1] K. D. Miller *et al.* "Brain and other central nervous system tumor statistics, 2021." In: *CA: a cancer journal for clinicians* 71.5 (Sept. 2021), pp. 381–406. ISSN: 1542-4863. DOI: 10.3322/caac.21693.

[2] D. N. Louis *et al.* "The 2021 WHO Classification of Tumors of the Central Nervous System: a summary". In: *Neuro-Oncology* 23.8 (Aug. 2021), pp. 1231–1251. ISSN: 1522-8517. DOI: 10.1093/neuonc/noab106.

[3] C. Horbinski *et al.* "Clinical implications of the 2021 edition of the WHO classification of central nervous system tumours". In: *Nature Reviews Neurology* 18.9 (Sept. 2022), pp. 515–529. ISSN: 1759-4758. DOI: 10.1038/s41582-022-00679-w.

[4] D. N. Louis *et al.* "The 2016 World Health Organization Classification of Tumors of the Central Nervous System: a summary". In: *Acta Neuropathologica* 131.6 (June 2016), pp. 803–820. ISSN: 0001-6322. DOI: 10.1007/s00401-016-1545-1.

[5] B. M. Ellingson *et al.* "Consensus recommendations for a standardized Brain Tumor Imaging Protocol in clinical trials". In: *Neuro-Oncology* 17.9 (Aug. 2015), pp. 1188–1198. ISSN: 1523-5866. DOI: 10.1093/neuonc/nov095.

[6] M. Smits. "MRI biomarkers in neuro-oncology". In: *Nature Reviews Neurology* 17.8 (Aug. 2021), pp. 486–500. ISSN: 1759-4758. DOI: 10.1038/s41582-021-00510-y.

[7] J. E. Villanueva-Meyer, M. C. Mabray, and S. Cha. "Current Clinical Brain Tumor Imaging". In: *Neurosurgery* 81.3 (Sept. 2017), pp. 397–415. ISSN: 0148-396X. DOI: 10.1093/neuros/nyx103.

[8] J. E. Eckel-Passow *et al.* "Glioma Groups Based on 1p/19q, IDH , and TERT Promoter Mutations in Tumors". In: *New England Journal of Medicine* 372.26 (June 2015), pp. 2499–2508. ISSN: 0028-4793. DOI: 10.1056/NEJMoa1407279.

[9] M. M. J. Wijnenga *et al.* "The impact of surgery in molecularly defined low-grade glioma: an integrated clinical, radiological, and molecular analysis". In: *Neuro-Oncology* 20.1 (Jan. 2018), pp. 103–112. ISSN: 1522-8517. DOI: 10.1093/neuonc/nox176.

[10] P. Clement *et al.* "GliMR: Cross-Border Collaborations to Promote Advanced MRI Biomarkers for Glioma". In: *Journal of Medical and Biological Engineering* 41.2 (Apr. 2021), pp. 115–125. ISSN: 1609-0985. DOI: 10.1007/s40846-020-00582-z.

[11] V. Romeo *et al.* "A Critical Appraisal of the Quality of Glioma Imaging Guidelines Using the AGREE II Tool: A EuroAIM Initiative." In: *Frontiers in oncology* 9 (2019), p. 472. ISSN: 2234-943X. DOI: 10.3389/fonc.2019.00472.

[12] N. M. deSouza *et al.* "Standardised lesion segmentation for imaging biomarker quantitation: a consensus recommendation from ESR and EORTC". In: *Insights into Imaging* 13.1 (Oct. 2022), p. 159. ISSN: 1869-4101. DOI: 10.1186/s13244-022-01287-4.

[13] J. P. B. O'Connor *et al.* "Imaging biomarker roadmap for cancer studies". In: *Nature Reviews Clinical Oncology* 14.3 (Mar. 2017), pp. 169–186. ISSN: 1759-4774. DOI: 10.1038/nrclinonc.2016.162.

[14] E. Manfrini *et al.* "From research to clinical practice: a European neuroradiological survey on quantitative advanced MRI implementation". In: *European Radiology* 31.8 (Aug. 2021), pp. 6334–6341. ISSN: 0938-7994. DOI: 10.1007/s00330-020-07582-2.

[15] K. M. Donahue *et al.* "Utility of simultaneously acquired gradient-echo and spin-echo cerebral blood volume and morphology maps in brain tumor patients". In: *Magnetic Resonance in Medicine* 43.6 (June 2000), pp. 845–853. ISSN: 0740-3194. DOI: 10.1002/1522-2594(200006)43:6<845::AID-MRM10>3.0.CO;2-J.

[16] J. L. Boxerman, K. M. Schmainda, and R. M. Weisskoff. "Relative cerebral blood volume maps corrected for contrast agent extravasation significantly correlate with glioma tumor grade, whereas uncorrected maps do not." In: *AJNR. American journal of neuroradiology* 27.4 (Apr. 2006), pp. 859–67. ISSN: 0195-6108.

[17] E. S. Paulson and K. M. Schmainda. "Comparison of Dynamic Susceptibility-weighted Contrast-enhanced MR Methods: Recommendations for Measuring Relative Cerebral Blood Volume in Brain Tumors". In: *Radiology* 249.2 (Nov. 2008), pp. 601–613. ISSN: 0033-8419. DOI: 10.1148/radiol.2492071659.

[18] J. L. Boxerman *et al.* "Consensus recommendations for a dynamic susceptibility contrast MRI protocol for use in high-grade gliomas". In: *Neuro-Oncology* 22.9 (Sept. 2020), pp. 1262–1275. ISSN: 1522-8517. DOI: 10.1093/neuonc/noaa141.

[19] C. C. Quarles, B. D. Ward, and K. M. Schmainda. "Improving the reliability of obtaining tumor hemodynamic parameters in the presence of contrast agent extravasation". In: *Magnetic Resonance in Medicine* 53.6 (June 2005), pp. 1307–1316. ISSN: 0740-3194. DOI: 10.1002/mrm.20497.

[20] A. Bjornerud *et al.* "T1- and T2*-dominant extravasation correction in DSC-MRI: part I–theoretical considerations and implications for assessment of tumor hemodynamic properties." In: *Journal of cerebral blood flow and metabolism : official journal of the International Society of Cerebral Blood Flow and Metabolism* 31.10 (Oct. 2011), pp. 2041–53. ISSN: 1559-7016. DOI: 10.1038/jcbfm.2011.52.

[21] K. Leu *et al.* "Improved Leakage Correction for Single-Echo Dynamic Susceptibility Contrast Perfusion MRI Estimates of Relative Cerebral Blood Volume in High-Grade Gliomas by Accounting for Bidirectional Contrast Agent Exchange." In: *AJNR. American journal of neuroradiology* 37.8 (Aug. 2016), pp. 1440–6. ISSN: 1936-959X. DOI: 10.3174/ajnr.A4759.

[22] T. Sugahara *et al.* "Correlation of MR imaging-determined cerebral blood volume maps with histologic and angiographic determination of vascularity of gliomas." In: *AJR. American journal of roentgenology* 171.6 (Dec. 1998), pp. 1479–86. ISSN: 0361-803X. DOI: 10.2214/ajr.171.6.9843274.

[23] M. H. Lev *et al.* "Glial tumor grading and outcome prediction using dynamic spin-echo MR susceptibility mapping compared with conventional contrast-enhanced MR: confounding effect of elevated rCBV of oligodendrogliomas [corrected]." In: *AJNR. American journal of neuroradiology* 25.2 (Feb. 2004), pp. 214–21. ISSN: 0195-6108.

[24] K. M. Schmainda *et al.* "Characterization of a first-pass gradient-echo spin-echo method to predict brain tumor grade and angiogenesis." In: *AJNR. American journal of neuroradiology* 25.9 (Oct. 2004), pp. 1524–32. ISSN: 0195-6108.

[25] B. J. McCullough *et al.* "Preoperative relative cerebral blood volume analysis in gliomas predicts survival and mitigates risk of biopsy sampling error." In: *Journal of neuro-oncology* 136.1 (Jan. 2018), pp. 181–188. ISSN: 1573-7373. DOI: 10.1007/s11060-017-2642-2.

[26] R. K. Soliman *et al.* "Preoperative Grading of Glioma Using Dynamic Susceptibility Contrast MRI: Relative Cerebral Blood Volume Analysis of Intra-tumoural and Peri-tumoural Tissue". In: *Clinical Neurology and Neurosurgery* 167 (Apr. 2018), pp. 86–92. ISSN: 03038467. DOI: 10.1016/j.clineuro.2018.01.003.

[27] J. Juan-Albarracín *et al.* "Glioblastoma: Vascular Habitats Detected at Preoperative Dynamic Susceptibility-weighted Contrast-enhanced Perfusion MR Imaging Predict Survival." In: *Radiology* 287.3 (June 2018), pp. 944–954. ISSN: 1527-1315. DOI: 10.1148/radiol.2017170845.

[28] M. Maeda *et al.* "Tumor vascularity in the brain: evaluation with dynamic susceptibility-contrast MR imaging." In: *Radiology* 189.1 (Oct. 1993), pp. 233–238. ISSN: 0033-8419. DOI: 10.1148/radiology.189.1.8372199.

[29] J. M. Connelly *et al.* "Magnetic Resonance Imaging Mapping of Brain Tumor Burden: Clinical Implications for Neurosurgical Management: Case Report". In: *Neurosurgery Open* 2.4 (Dec. 2021). ISSN: 2633-0873. DOI: 10.1093/neuopn/okab029.

[30] N. R. Parker *et al.* "Molecular Heterogeneity in Glioblastoma: Potential Clinical Implications". In: *Frontiers in Oncology* 5 (Mar. 2015). ISSN: 2234-943X. DOI: 10.3389/fonc.2015.00055.

[31] J. Lu, X. Li, and H. Li. "Perfusion parameters derived from MRI for preoperative prediction of IDH mutation and MGMT promoter methylation status in glioblastomas". In: *Magnetic Resonance Imaging* 83 (Nov. 2021), pp. 189–195. ISSN: 0730725X. DOI: 10.1016/j.mri.2021.09.005.

[32] Z. Pedeutour-Braccini *et al.* "Microfoci of malignant progression in diffuse low-grade gliomas: towards the creation of an intermediate grade in glioma classification?" In: *Virchows Archiv* 466.4 (Apr. 2015), pp. 433–444. ISSN: 0945-6317. DOI: 10.1007/s00428-014-1712-5.

[33] P. Patel *et al.* "MR perfusion-weighted imaging in the evaluation of high-grade gliomas after treatment: a systematic review and meta-analysis". In: *Neuro-Oncology* 19.1 (Jan. 2017), pp. 118–127. ISSN: 1522-8517. DOI: 10.1093/neuonc/now148.

[34] M. Prah *et al.* "Repeatability of Standardized and Normalized Relative CBV in Patients with Newly Diagnosed Glioblastoma". In: *American Journal of Neuroradiology* 36.9 (Sept. 2015), pp. 1654–1661. ISSN: 0195-6108. DOI: 10.3174/ajnr.A4374.

[35] K. M. Schmainda *et al.* "Value of dynamic contrast perfusion MRI to predict early response to bevacizumab in newly diagnosed glioblastoma: results from ACRIN 6686 multicenter trial". In: *Neuro-Oncology* 23.2 (Feb. 2021), pp. 314–323. ISSN: 1522-8517. DOI: 10.1093/neuonc/noaa167.

[36] K. Schmainda *et al.* "Multisite Concordance of DSC-MRI Analysis for Brain Tumors: Results of a National Cancer Institute Quantitative Imaging Network Collaborative Project". In: *American Journal of Neuroradiology* 39.6 (June 2018), pp. 1008–1016. ISSN: 0195-6108. DOI: 10.3174/ajnr.A5675.

[37] L. S. Hu *et al.* "Reevaluating the imaging definition of tumor progression: perfusion MRI quantifies recurrent glioblastoma tumor fraction, pseudoprogression, and radiation necrosis to predict survival". In: *Neuro-Oncology* 14.7 (July 2012), pp. 919–930. ISSN: 1522-8517. DOI: 10.1093/neuonc/nos112.

[38] M. A. Prah *et al.* “Spatial discrimination of glioblastoma and treatment effect with histologically-validated perfusion and diffusion magnetic resonance imaging metrics”. In: *Journal of Neuro-Oncology* 136.1 (Jan. 2018), pp. 13–21. ISSN: 0167-594X. DOI: 10.1007/s11060-017-2617-3.

[39] L. Hu *et al.* “Impact of Software Modeling on the Accuracy of Perfusion MRI in Glioma”. In: *American Journal of Neuroradiology* 36.12 (Dec. 2015), pp. 2242–2249. ISSN: 0195-6108. DOI: 10.3174/ajnr.A4451.

[40] M. V. Milchenko *et al.* “Comparison of Perfusion- and Diffusion-weighted Imaging Parameters in Brain Tumor Studies Processed Using Different Software Platforms”. In: *Academic Radiology* 21.10 (Oct. 2014), pp. 1294–1303. ISSN: 10766332. DOI: 10.1016/j.acra.2014.05.016.

[41] K. M. Schmainda *et al.* “Dynamic susceptibility contrast MRI measures of relative cerebral blood volume as a prognostic marker for overall survival in recurrent glioblastoma: results from the ACRIN 6677/RTOG 0625 multicenter trial.” In: *Neuro-oncology* 17.8 (Aug. 2015), pp. 1148–56. ISSN: 1523-5866. DOI: 10.1093/neuonc/nou364.

[42] E. R. Gerstner *et al.* “ACRIN 6684: Assessment of Tumor Hypoxia in Newly Diagnosed Glioblastoma Using 18F-FMISO PET and MRI”. In: *Clinical Cancer Research* 22.20 (Oct. 2016), pp. 5079–5086. ISSN: 1078-0432. DOI: 10.1158/1078-0432.CCR-15-2529.

[43] A. M. Stokes, J. T. Skinner, and C. C. Quarles. “Assessment of a combined spin- and gradient-echo (SAGE) DSC-MRI method for preclinical neuroimaging.” In: *Magnetic resonance imaging* 32.10 (Dec. 2014), pp. 1181–90. ISSN: 1873-5894. DOI: 10.1016/j.mri.2014.08.027.

[44] J. T. Skinner *et al.* “Evaluation of a multiple spin- and gradient-echo (SAGE) EPI acquisition with SENSE acceleration: applications for perfusion imaging in and outside the brain.” In: *Magnetic resonance imaging* 32.10 (Dec. 2014), pp. 1171–80. ISSN: 1873-5894. DOI: 10.1016/j.mri.2014.08.032.

[45] F. Khalifa *et al.* “Models and methods for analyzing DCE-MRI: A review”. In: *Medical Physics* 41.12 (Nov. 2014), p. 124301. ISSN: 00942405. DOI: 10.1118/1.4898202.

[46] P. S. Tofts *et al.* “Estimating kinetic parameters from dynamic contrast-enhanced t1-weighted MRI of a diffusable tracer: Standardized quantities and symbols”. In: *Journal of Magnetic Resonance Imaging* 10.3 (Sept. 1999), pp. 223–232. ISSN: 1053-1807. DOI: 10.1002/(SICI)1522-2586(199909)10:3<223::AID-JMRI2>3.0.CO;2-S.

[47] J. Zhang *et al.* “Clinical Applications of Contrast-Enhanced Perfusion MRI Techniques in Gliomas: Recent Advances and Current Challenges”. In: *Contrast Media & Molecular Imaging* 2017 (2017), pp. 1–27. ISSN: 1555-4309. DOI: 10.1155/2017/7064120.

[48] M. O. Leach *et al.* “Imaging vascular function for early stage clinical trials using dynamic contrast-enhanced magnetic resonance imaging”. In: *European Radiology* 22.7 (July 2012), pp. 1451–1464. ISSN: 0938-7994. DOI: 10.1007/s00330-012-2446-x.

[49] G. Petralia *et al.* “Dynamic contrast-enhanced MRI in oncology: how we do it”. In: *La radiologia medica* 125.12 (Dec. 2020), pp. 1288–1300. ISSN: 0033-8362. DOI: 10.1007/s11547-020-01220-z.

[50] T. J. Yun *et al.* “Glioblastoma Treated with Concurrent Radiation Therapy and Temozolomide Chemotherapy: Differentiation of True Progression from Pseudoprogression with Quantitative Dynamic Contrast-enhanced MR Imaging”. In: *Radiology* 274.3 (Mar. 2015), pp. 830–840. ISSN: 0033-8419. DOI: 10.1148/radiol.14132632.

[51] J. U. Harrer *et al.* “Comparative study of methods for determining vascular permeability and blood volume in human gliomas”. In: *Journal of Magnetic Resonance Imaging* 20.5 (Nov. 2004), pp. 748–757. ISSN: 10531807. DOI: 10.1002/jmri.20182.

[52] S. Okuchi *et al.* “Diagnostic accuracy of dynamic contrast-enhanced perfusion MRI in stratifying gliomas: A systematic review and meta-analysis”. In: *Cancer Medicine* 8.12 (Sept. 2019), pp. 5564–5573. ISSN: 2045-7634. DOI: 10.1002/cam4.2369.

[53] Y. Hu *et al.* “Non-Invasive Estimation of Glioma IDH1 Mutation and VEGF Expression by Histogram Analysis of Dynamic Contrast-Enhanced MRI”. In: *Frontiers in Oncology* 10 (Dec. 2020). ISSN: 2234-943X. DOI: 10.3389/fonc.2020.593102.

[54] A. Ulyte *et al.* “Prognostic value of preoperative dynamic contrast-enhanced MRI perfusion parameters for high-grade glioma patients”. In: *Neuroradiology* 58.12 (Dec. 2016), pp. 1197–1208. ISSN: 0028-3940. DOI: 10.1007/s00234-016-1741-7.

[55] H. Kim. “Variability in Quantitative DCE-MRI: Sources and Solutions.” In: *Journal of nature and science* 4.1 (2018). ISSN: 2377-2700.

[56] C. Duan *et al.* “Are complex DCE-MRI models supported by clinical data?” In: *Magnetic Resonance in Medicine* 77.3 (Mar. 2017), pp. 1329–1339. ISSN: 0740-3194. DOI: 10.1002/mrm.26189.

[57] B. H. Menze *et al.* “The Multimodal Brain Tumor Image Segmentation Benchmark (BRATS)”. In: *IEEE Transactions on Medical Imaging* 34.10 (Oct. 2015), pp. 1993–2024. ISSN: 0278-0062. DOI: 10.1109/TMI.2014.2377694.

[58] L. Bell *et al.* “Open Source Initiative for Perfusion Imaging (OSIPI) : a profile on a community led initiative”. In: *2021 ISMRM & SMRT Annual Meeting & Exhibition*. 2021.

[59] A. Shukla-Dave *et al.* “Quantitative imaging biomarkers alliance (QIBA) recommendations for improved precision of DWI and DCE-MRI derived biomarkers in multicenter oncology trials”. In: *Journal of Magnetic Resonance Imaging* 49.7 (June 2019). ISSN: 1053-1807. DOI: 10.1002/jmri.26518.

[60] D. C. Alsop *et al.* “Recommended implementation of arterial spin-labeled perfusion MRI for clinical applications: A consensus of the ISMRM perfusion study group and the European consortium for ASL in dementia”. In: *Magnetic Resonance in Medicine* 73.1 (Jan. 2015), pp. 102–116. ISSN: 0740-3194. DOI: 10.1002/mrm.25197.

[61] A. Mahroo *et al.* “Robust Multi-TE ASL-Based Blood–Brain Barrier Integrity Measurements”. In: *Frontiers in Neuroscience* 15 (Dec. 2021). ISSN: 1662-453X. DOI: 10.3389/fnins.2021.719676.

# 3

# IMPROVED RELIABILITY OF PERFUSION ESTIMATION IN DYNAMIC SUSCEPTIBILITY CONTRAST MRI BY USING THE ARTERIAL INPUT FUNCTION FROM DYNAMIC CONTRAST ENHANCED MRI

This chapter has been published as:
**Tseng C-H**, Jaspers J, Romero AM, et al. Improved reliability of perfusion estimation in dynamic susceptibility contrast MRI by using the arterial input function from dynamic contrast enhanced MRI. NMR in Biomedicine. 2024; 37(1):e5038. doi:10.1002/nbm.5038.

## ABSTRACT

The arterial input function (AIF) plays a crucial role in estimating quantitative perfusion properties from dynamic susceptibility contrast (DSC) MRI. An important issue, however, is that measuring the AIF in absolute contrast agent concentrations is challenging due to uncertainty in the relation to the measured $R_2^*$-weighted signal, signal depletion at high concentration, and partial volume effects. A potential solution could be to derive the AIF from separately acquired dynamic contrast enhanced (DCE) MRI data. We aim to compare the AIF determined from DCE MRI with the AIF from DSC MRI, and estimated perfusion coefficients derived from DSC data using a DCE-driven AIF with perfusion coefficients determined using a DSC-based AIF. AIFs were manually selected in branches of the middle cerebral artery in both DCE and DSC data in each patient. In addition, a semi-automatic AIF-selection algorithm was applied to the DSC data. The amplitude and full-width-at-half-maximum of the AIFs were statistically compared using the Wilcoxon rank-sum test, applying a 0.05 significance level. Cerebral blood flow (CBF) was derived with different AIF approaches and further compared. The results showed that the AIFs extracted from DSC scans yielded highly variable peaks across arteries within the same patient. The semi-automatic DSC-AIF had significantly narrower width compared to the manual AIFs, and a significantly larger peak than the manual DSC-AIF. Additionally, the DCE-based AIF provided a more stable measurement of relative CBF and absolute CBF values estimated with DCE-AIFs that were compatible with previously reported values. In conclusion, DCE-based AIFs reproduced significantly better across vessels, showed more realistic profiles and delivered more stable and reasonable CBF measurements. The DCE-AIF can, therefore, be considered as an alternative AIF source for quantitative perfusion estimations in DSC MRI.

## 3.1. INTRODUCTION

Over the past three decades, dynamic susceptibility contrast (DSC) MRI has emerged as a powerful tool for studying the brain's haemodynamic characteristics. It is applied to estimate perfusion properties in patients with various pathologies including stroke and cancer patients, e.g. the cerebral blood volume (CBV), cerebral blood flow (CBF) and mean transition time (MTT) [1, 2]. Additionally, timing parameters, such as time-to-bolus-peak, were found to have important clinical value [3]. The estimation of tissue perfusion properties is based on indicator dilution theory [4] and is driven by the measurement of the arterial input function (AIF). The AIF represents the time varying contrast agent concentration measured in arterial blood supplying the tissue under investigation. Ideally, it should be measured directly in the artery supplying the tissue of interest. However, in practice it is usually derived from a large artery, such as internal carotid artery or middle cerebral artery (MCA).



An issue in estimating the perfusion properties is that the relation between the $\Delta R_2^*$ weighted DSC signal and the contrast agent concentration is uncertain. For practical reasons it is often assumed that contrast-induced changes in $R_2^*$ are linearly proportional to the contrast agent concentration. However, some studies showed that the relation is rather more quadratic than linear as well as dependent on the haematocrit level in blood [5–8]. Moreover, three effects can severely affect the shape of the measured AIF. First, the AIF is assumed to be measured in pure blood, which will never be the case as limited spatial resolution leads to mixing of structures, known as partial volume effects [9]. Such partial volume effects can lead to highly non-linear distortions of the measured AIF. Second, the signal in large arteries tends to reach the noise floor during the passage of contrast agents, leading to signal depletion [10]. This is due to the commonly applied choice of a single, long echo time in clinical practice that is optimal for capturing the bolus passage in brain tissue. Third, the time-concentration curve from voxels inside an artery, especially the peak, can become distorted due to displacement effects resulting from the increase of the local precession frequency induced by the paramagnetic contrast agent within the artery [11].

Dynamic contrast enhanced (DCE) MRI is another perfusion technique enabling estimation of cerebral haemodynamics, which is based on the $R_1$-effects induced by the contrast agent. Importantly, the relation between the $R_1$ relaxation rate and contrast concentration in blood has been comprehensively studied and is more stable under different conditions than $R_2^*$ based measurements [12]. As such, DCE imaging holds the potential to provide a more accurate AIF measurement in absolute units (i.e. in mM). Furthermore, the Spoiled Gradient Recalled (SPGR) imaging sequence that is commonly used for DCE MRI provides somewhat higher spatial resolution reducing partial volume effects. Still there are two issues when measuring the AIF with DCE MRI. First, fresh, unsaturated protons can flow into the imaging volume, while they are assumed to be saturated, leading to underestimation of the contrast agent concentration: this is referred to as 'inflow effects' [13, 14]. Lately, however, several approaches were proposed to ameliorate inflow effects [15–17]. Second, concomitant $T_2^*$ effects induced by high contrast

concentration may confound the measured $R_1$-weighted signal enhancement [18]. This effect can be diminished by using a sufficiently short echo time for the DCE sequence.

We hypothesized that a DCE-based AIF measurement might improve perfusion measurement in DSC MRI compared to using a DSC-based AIF measurements. Of course, the need for two contrast agent based MRI scans, might make such an approach clinically impractical at first sight. However, a preload contrast injection is frequently applied in DSC MRI in order to saturate the extravascular space to minimise errors by contrast agent leakage [19, 20]. Therefore, this preloading stage might be exploited by performing DCE-image acquisition from which a potentially improved AIF could be obtained. In addition to AIF-determination, these data could also be used for leakage quantification and estimating vascular permeability, but it is not the focus of the current study.

In this study, we aimed to compare the AIFs measured from DCE and DSC MRI as well as the effect of the different AIF approaches on the estimation of perfusion properties. To do so, we performed combined DCE and DSC imaging in patients suffering from diffuse gliomas as included in an ongoing study into effects of radiotherapy. The characteristics of the AIFs from both DCE and DSC imaging were systematically studied. Furthermore, perfusion parameters were compared when using the two different AIFs.

## 3.2. METHODS

### 3.2.1. PATIENT COHORT

Data in this study was acquired as part of an associated clinical study in the Netherlands: the Radiotherapy in isocitrate dehydrogenase (IDH) mutated Glioma: Evaluation of Late outcomes (RIGEL) study (trial identifier: NCT04304300). The first ten patients who had histologically confirmed, IDH mutated glioma (WHO grade 2 or 3) and of whom the relevant imaging data were available were included in this sub-study. Informed consent was obtained from all individual participants. Postoperative radiation therapy and chemotherapy were given to every patient after surgical tumor resection. MRI was performed before and approximately 4 months after radiation therapy. From one patient DSC and DCE images were obtained before and after radiation therapy, from two patients scans were only made post-treatment, and from seven patients the pre-treatment images were included. Table 3.1 collates the relevant information of our patient cohort.

### 3.2.2. IMAGING AND INJECTION PROTOCOL

Imaging was performed on a 3T MRI system (Signa Premier, GE Healthcare, Wisconsin, USA) with a 48-channel head coil in the Erasmus MC (Rotterdam, the Netherlands).

Prior to contrast-enhanced imaging, a high resolution $T_1$-weighted image was acquired using an inversion recovery preparation, 3D fast spoiled gradient echo

Table 3.1: Patient cohort

| Patient number | Age | Sex | | Tumor hemisphere | | MRI timing | |
|---|---|---|---|---|---|---|---|
| N=10 | 36.1±10.3 | Male | 7 | Right | 8 | Pre-treatment | 7 |
| | | Female | 3 | Left | 2 | Post-treatment | 2 |
| | | | | | | Both | 1 |



sequence (brain volume imaging, BRAVO) with repetition time (TR)/echo time (TE): 7.6/3.1 ms, inversion time: 450 ms, flip angle: 12°; FOV: 240 × 240 × 175 $mm^3$, matrix size: 256 × 256 × 176, in-plane resolution: 0.94 × 0.94 $mm^2$.

In each patient, 7.5 ml of Gadobutrol (Gadovist®, Bayer, Germany), corresponding to a standard dose for a 75 kg patient, followed by a 15 mL saline flush were automatically injected with a 22g cannula via the antecubital vein at 5 mL/s by a power injector (Spectris Solaris EP, MEDRAD, Pennsylvania, USA) during which DCE imaging was performed. Immediately after DCE acquisition, a second bolus of contrast agent with the same dose and protocol was injected during which DSC imaging was done. The contrast agent injections were started 20 seconds after commencing the DCE and DSC acquisitions.

DCE images were acquired using a differential subsampling with Cartesian ordering (DISCO) sequence [21] with TR/TE: 2.7/0.9 ms, flip angle: 14°; FOV: 220 × 220 × 142 $mm^3$, matrix size: 128 × 128, 72 slices, in-plane resolution: 1.7 × 1.7 $mm^2$, slice thickness: 2 mm, temporal resolution: 2 s, yielding 183 dynamics at a total scan time of 6 minutes and 20 seconds. DSC images were obtained with a $T_2^*$-weighted gradient-echo echo-planar imaging sequence with TR/TE: 2000/45 ms, FOV: 220 × 220 × 140 $mm^3$, matrix size: 100 × 100, 29 slices, in-plane resolution: 2.2 × 2.2 $mm^2$, slice thickness: 5 mm, temporal resolution: 2 s, yielding 50 dynamics in total.

### 3.2.3. PRE-PROCESSING

All image processing was done with in-house created software in MATLAB R2020a (The MathWorks, Inc., Natick, Massachusetts, United States). Head motion between the dynamic scans (both DCE and DSC images) was visually checked by monitoring the three cross sectional lines of central coronal, sagittal and axial slices across time. In case misalignment of the boundaries in these orthogonal slices was observed, this was corrected by performing image registration of the entire series to the first volume. Registration was done by a 3D rigid transformation optimizing the normalized mutual information as implemented in SPM12 [22]. Subsequently all DSC volumes were resampled to 72 slices and registered to the first DCE volume with the same registration approach. Finally, all volumes were resampled to share the same image coordinates and voxel size.

### 3.2.4. AIF SELECTION

AIF measurements were obtained in three ways. From the DCE data, the DCE-AIF was determined via manual selection based on the criteria described below. From the DSC data, AIFs were obtained by two different approaches: 1) projection of the manually selected voxels from the DCE images onto the DSC images followed by a manual correction step (see below); 2) a semi-automatic identification from the DSC series. The latter two AIFs will be referred to as the *manual DSC-AIF* and the *semi-automatic DSC-AIF*, respectively.



#### DCE-AIF MEASUREMENT

In every dataset, five different arteries belonging to the territory of the MCA were visually identified based on clearly observable signal changes during the upslope of the contrast agent passage. In each such artery, a group of voxels were delineated inside the artery. Such ROIs were placed in the central part of vessels to limit partial volume effects as much as feasible. Subsequently, the selected ROIs were projected onto the entire DCE time series. The resulting concentration-time curves were not reviewed based on visual quality in any way.

#### DSC-AIF MEASUREMENT

First, the selected voxels of the five arteries in the DCE images were copied onto all the registered DSC images. These copied ROIs could subsequently be slightly adjusted to make sure that these were all located inside the artery. This step was added to compensate for small misregistrations when deemed necessary. The resulting ROI was then projected on the entire DSC series. Again, the resulting concentration-time curves were not reviewed for visual quality.

Secondly, a semi-automatic technique for AIF-selection was applied based on a clustering approach favouring early bolus arrival time, large area under curve and small residual error of a fit with a gamma function [23]. Initial experiments were performed first to optimize the search region and the optimal number of selected voxels by the algorithm. The tuning procedure is illustrated in the supplementary material (Figure S3.1). Subsequently, the optimal settings were applied in the same five slices of the DCE-AIF determination. In each slice, the algorithm automatically identified a group of voxels in which the signal resembled an AIF, irrespective whether they resided inside an artery. No further corrections were applied to the selected voxels.

The signals in each ROI (manual selection) and groups of voxels (semi-automatic selection) were averaged to yield mean time-intensity curves. Thus, for each type of AIF (DCE-AIF, manual DSC-AIF, semi-automatic DSC-AIF), five such curves were generated for each patient. The mean time-intensity curves were subsequently normalised by dividing them by the average signal of the first five time points (i.e. baseline points) to produce signal ratio curves which were used to derive contrast concentration-time curves. Figure 3.1 summarizes our AIF selection procedure.

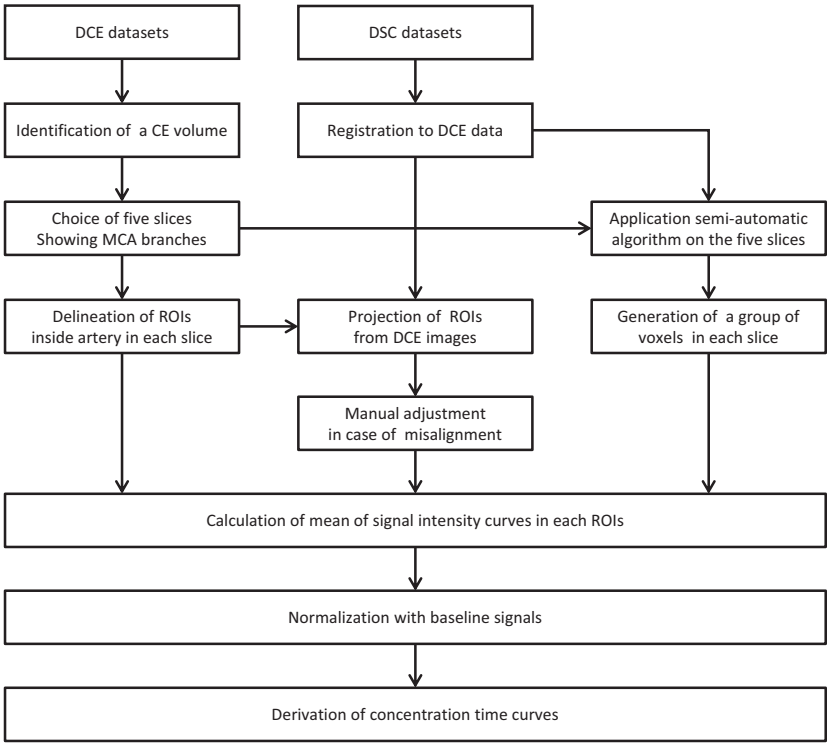


**CE: Contrast Enhanced, MCA: Middle Cerebral Artery, ROI: Region of Interest*

Figure 3.1: Flowchart of our AIF selection procedure.

### 3.2.5. AIF CALCULATION FROM DCE IMAGES

A previously published approach [17] was applied to compensate for potential underestimation of contrast concentration due to inflow effects. Specifically, a parameterized version of Orton's AIF model [24], constrained by a fixed area under the first passage reflecting the known injection dose, was first fitted to the DCE signal ratio curve to estimate the number of excitation pulses experienced by the protons. Subsequently, the estimated number of pulses was used to calculate the contrast agent concentration at each time point so that the underestimation from the inflow effect was corrected for. The inflow-compensated signal ratio curves

from the DCE images were transformed into contrast concentration-time curves by assuming a linear relation between the concentration and the $T_1$-relaxivity [25]; the longitudinal relaxivity in plasma (asserting a haematocrit level of 0.45) at 3.0 T was assumed to be 4.5 $L \cdot (mM \cdot s)^{-1}$ for gadobutrol at 37°C [12], and the initial $T_1$ value of blood was set to 1.6 s [26].



### 3.2.6. AIF CALCULATION FROM DSC IMAGES

The DSC-driven AIFs were first translated into concentration-time curves by the most commonly used conversion model. As such the $\Delta R_2^*$ was assumed to be linearly related to the contrast agent concentration. We initially computed:

$$\Delta R_2^*(t) = \frac{-1}{TE} \cdot \ln Sr(t) \tag{3.1}$$

in which $TE$ is the echo time of DSC sequence, and $Sr(t)$ is the signal ratio curve. Subsequently, relying on the linearity assumption, we determined the contrast agent concentration. We applied a proportionality constant of 16.5 $(mM \cdot s)^{-1}$ which we derived from the linear approximation of a quadratic model at contrast concentrations ranging from 0-10 mM [8]. Dividing $\Delta R_2^*$ by this constant yielded the contrast concentration for the manual and the semi-automatic DSC-AIFs.

### 3.2.7. QUANTITATIVE ASSESSMENT OF AIF CURVES

For each method in every patient, the mean and variance of the peak values and the full width of half maximums (FWHMs) of the AIFs were determined and compared between the methods. Differences were statistically assessed using the Wilcoxon rank-sum test. P-values smaller than 0.05 were considered as statistical significant. Scatter plots and Bland-Altman plots were created for comparison of differences between methods.

### 3.2.8. PERFUSION COEFFICIENTS

CBF was calculated from the DSC data based on a conventional tracer kinetic model [27], in which the relationship between the tissue response and the AIF is defined through a convolution integral:

$$\frac{1 - Hct_{LV}}{\rho \cdot (1 - Hct_{SV})} \cdot C_t(t) = CBF \cdot (C_a(t) * R(t)) \tag{3.2}$$

in which $\rho$ is the assumed density of brain tissue set to 1.04 g/ml and $Hct_{LV}$ and $Hct_{SV}$ are the presumed hematocrit levels in large and small vessels of 0.45 and 0.25 respectively, as used in Rempp et al.[28], $C_t(t)$ is the time-concentration curve in tissue, $C_a(t)$ is the AIF and $R(t)$ is the tissue residue function. The latter function describes the fraction of a hypothetical instantaneous bolus of tracer that is still present in the tissue at time t and is obtained by deconvolving $C_t(t)$ with $C_a(t)$. The maximum value of the deconvolution outcome represents the CBF value

in the concerning voxel. The block-circulant deconvolution method was applied for this calculation, which has been proven to be less sensitive to delay-effects between AIF and tissue passage curves [29].

The relative CBF (rCBF) was used to compare the stability and reliability of the various AIF types in perfusion estimation. A group of voxels was manually selected in normal appearing white matter in a region contralaterally with respect to the tumor location. The rCBF map was produced by dividing all CBF values with the mean of the selected region. The coefficient of variation (CV) in rCBF was computed using the three AIFs measured across the different slices (i.e. rCBF maps were calculated based on the AIFs determined from the five different arteries). The CV in each voxel was then derived by calculating the ratio of the standard deviation and the mean.

In addition, the mean of the AIFs in each patient were used to estimate an absolute (i.e. quantitative) CBF measure (aCBF). As such, tissue concentration maps were generated by normalizing $\Delta R_2^*$ (t) with a previously reported relaxivity value $r_2^*$ in tissue:

$$C(t) = \frac{\Delta R_2^*}{r_2^*} \tag{3.3}$$

in which $r_2^*$ was set equal to 85 $(\text{mM}\cdot\text{s})^{-1}$ [30]. Subsequently, aCBF maps were produced by deconvolving the tissue concentration-time curves with the AIFs. This aCBF was registered to the $T_1$-weighted image via SPM12 for further processing. Tissue probability maps were derived by applying the SPM12 segmentation function on the $T_1$-weighted image. The hemisphere from which the tumor was removed was masked in each patient. Finally, aCBF values of the remaining, normal appearing grey matter (GM) and white matter (WM) were sampled and compared to values reported in literature.

## 3.3. RESULTS

### 3.3.1. EXAMPLE DCE- AND DSC-AIFS

One representative example of AIF-selection is shown in Figure 3.2. The selected region was determined based on the DCE image containing the MCA (Figure 3.2a) and projected onto the registered, corresponding DSC slice (Figure 3.2b). Observe that the DCE-AIFs across voxels appear much more consistent and exhibit less variation in peak height than the DSC-AIFs (Figure 3.2d). The selected arterial-like voxels from the semi-automatic algorithm applied on the same slice are shown in Figure 3.2c and the AIF calculations from every individually selected voxel is plotted in Figure 3.2d. Figure 3.2f shows the characteristics of the AIFs obtained from the three approaches. While overlapping the peaks of two manual approaches, the shapes of the DCE-AIF and the manual DSC-AIF appear very similar, especially during the first passage of the contrast bolus. Instead, the semi-automatic DSC-AIF demonstrated higher peak values in combination with a more narrow width compared to the manual DSC-AIF. Further results related to the optimization of the

semi-automatic DSC-AIF estimation are included as supplementary material.

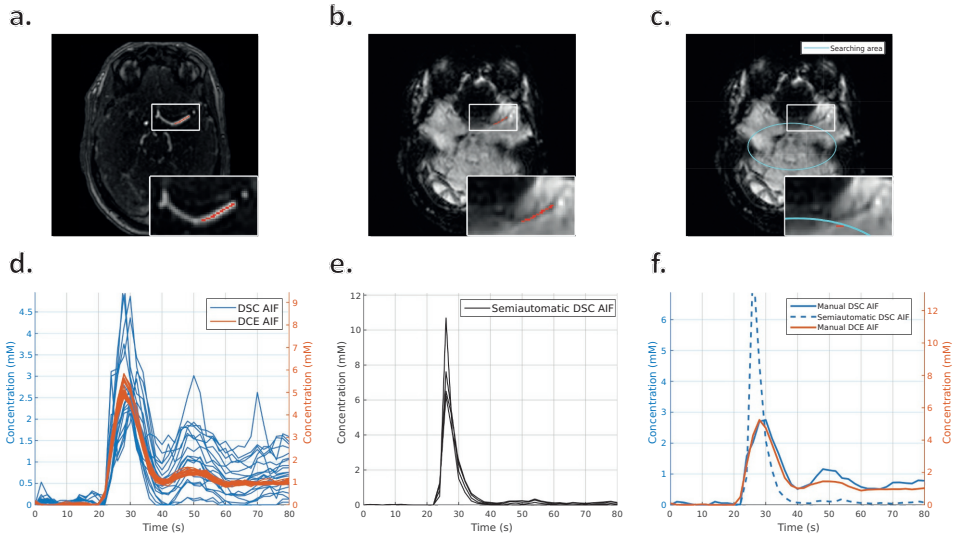


Figure 3.2: Illustration of AIF measurements in a single artery of an example patient. The ROI was manually selected in the DCE images (a) and subsequently projected onto the registered DSC images (b). A semi-automatic detection algorithm was applied to the same plane; detected voxels are indicated in red (c). Contrast concentration changes measured in the voxels from the selected regions in (a) and (b) are plotted in (d). Blue lines are measurements from DSC MRI (left y axis); red lines represent measurements from DCE MRI (right y axis). AIF curves from the automatically detected DSC voxels (c) are shown in (e). The mean DCE-AIF and the two mean DSC-AIFs are compared in (f). The peak of the DCE-AIF was aligned with the peak of the manual DSC-AIF to demonstrate the highly correlated shape of these two AIFs.

The DCE- and DSC-AIFs derived from different vessels (or slices) are plotted in Figure 3.3. Overall the DCE-based AIFs visually exhibited better reproducibility than the DSC-based AIFs in all patients. Only two patients are shown for illustration purposes, one with relatively small variation of the DSC-AIF peak heights (Figure 3.3b,c) and one with larger variation in both the peak height and tail shape (Figure 3.3e,f) which is more representative for the other patients.

### 3.3.2. QUANTITATIVE ANALYSIS

The mean and the standard deviation of the peak values and FWHM from the AIFs are summarized in Table 3.2. The CV of the peak values from all DSC-AIFs were larger than those of the DCE-AIFs. The peak value of the DCE-AIF was significantly higher than the peak value of the manual DSC-AIF (p-value: 0.00008). The peak value of the semi-automatic DSC-AIF was significantly higher than the peak value

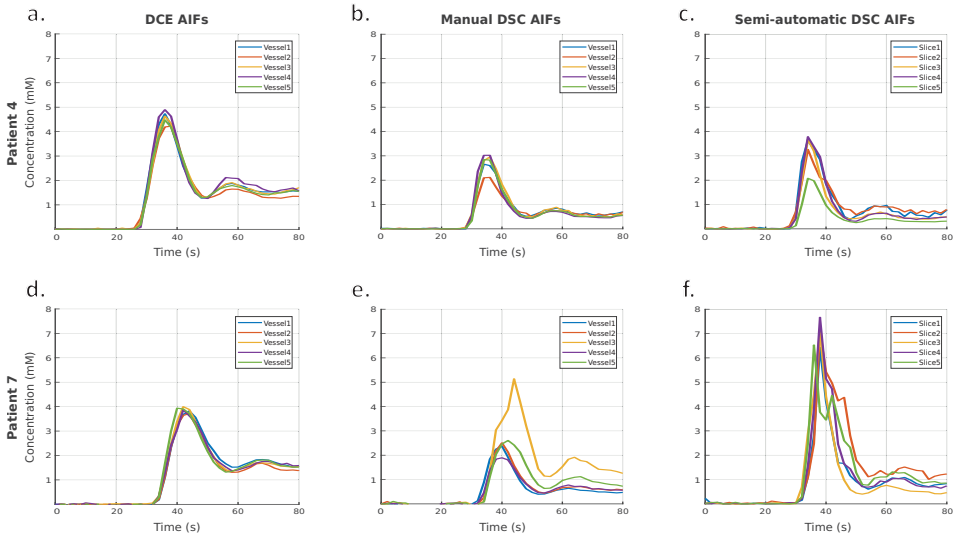


Figure 3.3: AIFs measured in five arteries (see legend) in two representative patients (top and bottom) using three approaches. The DCE-driven AIFs (a, d) indeed show less variation than both the manual (b, e) and semi-automatic (c, f) DSC-AIFs.

of the DCE-AIF (p-value: 0.03) and of the manual DSC-AIF (p-value: 0.00008). There was no significant difference between the mean FWHM of the DCE-AIF and the mean FWHM of the manual DSC-AIF. The mean FWHM of the DCE-AIF was significantly larger than the mean FWHM of the semi-automatic DSC-AIF (p-value: 0.0004). Likewise the FWHM of the manual DSC-AIF was significantly larger than the FWHM of the semi-automatic DSC-AIF (p-value: 0.0008). Scatter plots and Bland-Altman plots for comparison of the FWHM values are shown in Figure 3.4. The mean FWHM difference between the DCE-AIF and the manual DSC-AIF was 0.5±1.6 s (CI(95 % ) = [-2.5, 3.6]). The mean FWHM difference between the DCE-AIF and the semi-automatic DSC-AIF was 3.2±1.6 s (CI(95 % ) = [0.1, 6.3]). Finally, the mean FWHM difference between the two DSC-AIF methods was 2.7±1.2 s (CI(95 % ) = [0.3, 5.1]).

### 3.3.3. CBF ANALYSIS

The CV map of the rCBF with different types of AIFs in a representative patient is shown in Figure 3.5. The mean CV of whole brain rCBFs calculated with the different AIFs in every patient is listed in Table 3.3. One can observe that the DCE-AIF provided a more stable rCBF measurement, i.e. showing smaller relative variance than the DSC-AIFs did. Means and standard deviations of the sampled aCBF values in the GM and WM masks across individuals are collated in Table 3.4. The average aCBFs in GM and WM over all patients were 51.5 ml/100g/min and 24.0 ml/100g/min with the DCE-AIFs, 110.0 ml/100g/min and 44.2 ml/100g/min

| | DCE-AIF | | Manual DSC-AIF | | Semi-automatic DSC-AIF | |
|---|---|---|---|---|---|---|
| | Peak(mM) | FWHM(s) | Peak(mM) | FWHM(s) | Peak(mM) | FWHM(s) |
| Patient 1 | 9.4±1.1 | 6.5±0.7 | 2.5±0.7 | 5.9±1.2 | 7.4±2.1 | 4.6±1.1 |
| Patient 2 | 5.3±0.3 | 7.8±0.4 | 2.8±1.0 | 10.3±1.4 | 7.4±1.7 | 5.7±2.1 |
| Patient 3 | 6.4±0.3 | 6.7±0.4 | 2.6±0.1 | 6.8±1.9 | 5.2±1.3 | 3.9±0.5 |
| Patient 3 † | 5.7±0.5 | 8.9±1.6 | 2.7±0.6 | 8.5±1.4 | 5.8±1.5 | 5.7±1.9 |
| Patient 4 † | 4.6±0.3 | 9.0±0.3 | 2.8±0.4 | 9.0±0.6 | 3.4±0.7 | 7.4±0.8 |
| Patient 5 | 4.4±0.4 | 10.5±3.1 | 2.6±0.7 | 10.1±1.3 | 6.0±1.9 | 6.1±1.1 |
| Patient 6 | 4.5±0.5 | 9.4±2.2 | 2.5±0.7 | 8.4±0.9 | 3.8±0.4 | 6.8±0.3 |
| Patient 7 † | 4.0±0.1 | 10.3±0.5 | 2.9±1.3 | 10.1±1.4 | 7.0±0.6 | 5.6±0.9 |
| Patient 8 | 4.6±0.5 | 13.0±2.1 | 3.0±0.7 | 8.8±1.7 | 6.8±1.5 | 6.0±2.7 |
| Patient 9 | 5.5±0.7 | 10.1±2.0 | 3.0±0.7 | 9.6±0.8 | 6.8±1.4 | 7.6±2.3 |
| Patient 10 | 6.7±0.3 | 8.9±0.8 | 2.6±0.7 | 7.9±1.5 | 5.1±1.9 | 6.3±2.8 |
| Average | 5.6±1.7 | 9.2±1.9 | 2.7±0.2 | 8.7±1.4 | 5.9±1.4 | 6.0±1.1 |

Note: Data are reported as mean ± standard deviation.
† Patient received radiation therapy

Table 3.2: Mean peak values and FWHM and corresponding standard deviations for the different patients and AIF measurement methods.

with the manual DSC-AIFs, and 72.5 ml/100g/min and 28.4 ml/100g/min with the semi-automatic DSC-AIFs, respectively. Patient 6 was excluded from the calculation of the group average because severe ringing artefacts were observed (Figure S3.2). Additional results related to CBV estimation are presented in the supplementary material.

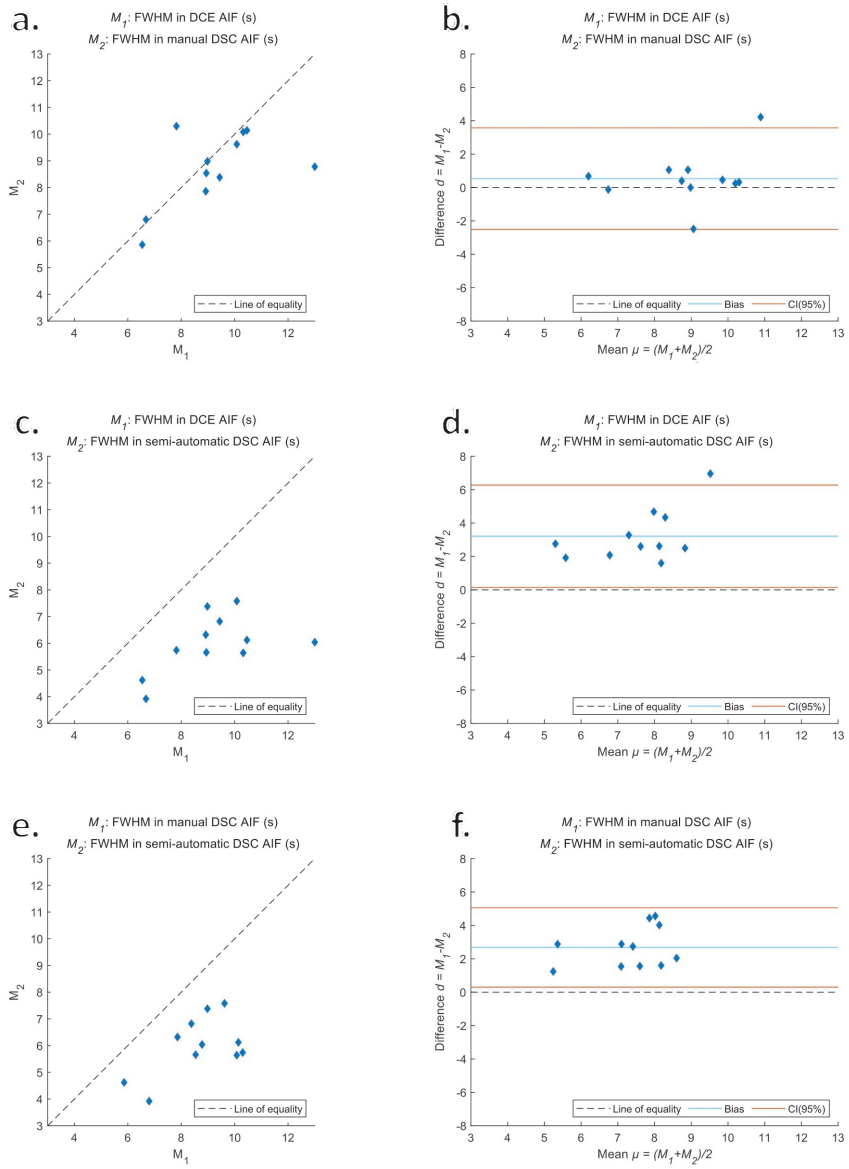


Figure 3.4: Scatter plot (a, c, e) and Bland-Altman plot (b, d, f) of FWHMs calculated from the DCE-AIF, the manual DSC-AIF, and the semi-automatic DSC-AIF.

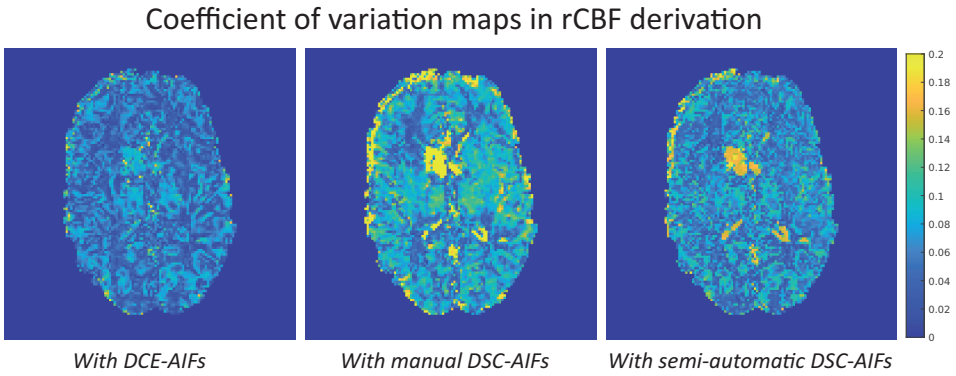


Figure 3.5: Representative CV map (for a single patient) derived from rCBF values computed from the DSC series using the DCE-AIFs (left), the manual DSC-AIFs (middle) and the semi-automatic DSC-AIFs (right). Observe that the DSC-AIFs introduced larger relative variation than the DCE-AIF did.

Table 3.3: Mean CV of rCBFs in whole brain for the different patients and AIF measurement methods

| | Mean CV of rCBF | | |
|---|---|---|---|
| | DCE-AIF | Manual DSC-AIF | Semi-automatic DSC-AIF |
| Patient 1 | 0.043 | 0.059 | 0.063 |
| Patient 2 | 0.028 | 0.038 | 0.083 |
| Patient 3 | 0.048 | 0.128 | 0.073 |
| Patient 3 † | 0.046 | 0.056 | 0.062 |
| Patient 4 † | 0.026 | 0.035 | 0.038 |
| Patient 5 | 0.025 | 0.035 | 0.055 |
| Patient 6 | 0.024 | 0.032 | 0.046 |
| Patient 7 † | 0.025 | 0.032 | 0.044 |
| Patient 8 | 0.039 | 0.051 | 0.085 |
| Patient 9 | 0.020 | 0.028 | 0.052 |
| Patient 10 | 0.039 | 0.064 | 0.072 |
| Average | 0.033 | 0.051 | 0.061 |

† Patient received radiation therapy

Table 3.4: Mean aCBF and corresponding standard deviation in each patient and the average over all patients.

| | Absolute CBF(mL/100g/min) | | | | | |
|---|---|---|---|---|---|---|
| | DCE-AIF | | Manual DSC-AIF | | Semi-automatic DSC-AIF | |
| | GM | WM | GM | WM | GM | WM |
| Patient 1 | 45.3±20.3 | 20.4±10.7 | 149.8±60.7 | 68.7±35.0 | 79.1±35.4 | 35.2±18.9 |
| Patient 2 | 60.8±28.7 | 21.9±11.8 | 92.2±44.0 | 33.3±17.8 | 63.8±31.1 | 22.8±12.9 |
| Patient 3 | 54.9±24.2 | 21.4±11.0 | 154.0±60.1 | 61.0±30.6 | 98.8±42.3 | 37.4±19.7 |
| Patient 3 † | 44.0±20.5 | 16.1±8.3 | 89.9±41.3 | 33.2±17.2 | 63.9±30.0 | 23.1±12.2 |
| Patient 4 † | 53.7±25.6 | 20.5±10.1 | 98.9±46.8 | 37.8±18.6 | 96.0±45.7 | 36.9±17.6 |
| Patient 5 | 51.4±25.1 | 19.4±11.0 | 85.0±41.1 | 32.1±18.3 | 59.3±29.3 | 21.7±13.0 |
| Patient 6 | 109.4±58.6 | 58.6±35.7 | 190.9±82.8 | 72.3±56.0 | 152.3±77.1 | 53.9±43.3 |
| Patient 7 † | 49.0±24.0 | 19.6±9.7 | 68.8±33.6 | 27.6±13.8 | 42.9±21.3 | 16.8±8.7 |
| Patient 8 | 47.4±21.1 | 22.4±12.0 | 112.1±47.4 | 52.5±28.0 | 68.6±29.7 | 31.9±17.6 |
| Patient 9 | 66.7±31.4 | 24.1±13.0 | 117.4±53.9 | 42.7±23.1 | 67.4±29.7 | 24.3±17.6 |
| Patient 10 | 41.4±19.3 | 16.8±8.3 | 131.8±55.6 | 53.18±26.3 | 84.7±32.7 | 33.8±13.3 |
| Average * | 51.5±7.8 | 24.0±3.9 | 110.0±28.3 | 44.2±13.9 | 72.5±17.2 | 28.4±7.4 |

Note: Data are reported as mean ± standard deviation.
* Patient 6 was excluded when deriving the average over the group as a large ringing-artefact was observed.
† Patient received radiation therapy

## 3.4. DISCUSSION

This paper studied the potential of replacing an AIF from DSC imaging with an AIF from DCE to improve the precision of estimating DSC-based perfusion properties. The DCE-driven AIF showed much more stable peak estimation and smoother curves compared to the DSC-AIFs. In effect, less variation in calculated perfusion parameters could be expected, which was confirmed by the reduced rCBF variance.



We attribute the better reproducibility of the DCE-driven AIF stems from absence of detrimental effects, such as susceptibility artefacts, large partial volume effects, signal depletion and voxel displacement which do affect the DSC data. Some previous studies introduced an additional slice or sequence targeting specifically the AIF measurement, to be succeeded by a more comprehensive DSC series [31–33]. Instead of doing this, we exploited the preload injection to perform DCE MRI. As such it facilitated acquisition of a quantitative AIF, i.e. representing contrast agent concentration instead of change in $R_2^*$ over time.

There is no agreement in the literature on a standardized approach to measure the AIF for perfusion estimation in DSC MRI due to several controversies [34]. Specifically, the AIF has been measured in arteries and veins, globally and locally, inside and outside arteries, individually and population-based, and manually or automatically. All these approaches were aimed at minimizing partial volume effects, signal depletion, AIF dispersion or any other confounding effects on the measured AIFs. Eventually, the chosen approach will be a compromise of these detrimental effects. Several semi-automatic and automatic measurement methods were proposed to avoid operational bias and simplify the procedure [23, 35–37]. Some of these approaches are widely available in commercial software. We used an open-source semi-automatic DSC-AIF algorithm, which detects the arterial voxels using a clustering algorithm with criteria as described by other researchers: early bolus arrival, large area under curve, and good fitting with a gamma variate function. However, the resulting AIFs had a higher peak with a narrower width in comparison with the manual AIFs. This probably resulted from the algorithm favoring a larger area under curve, as this might minimize partial volume effect. However, van Osch et al. [9] suggested that the partial volume effect may induce not only underestimation of AIF peak, but also lead to overestimations.

Previously, You et al. concluded that DCE based pharmacokinetic parameters derived using a DSC-AIF yielded better diagnostic accuracy and reliability for differentiating high grade astrocytoma from low grade astrocytoma than those derived with a DCE-AIF [38], i.e. the opposite to this study. Another study from the same group yielded a similar conclusion that the DSC-AIF helped differentiation of glioblastoma from primary central nervous system lymphoma compared to the DCE-AIF [39]. However, in these studies there was a mismatch in temporal resolution of the DCE and DSC acquisition, which was 4 seconds and 1.6 seconds, respectively. Furthermore, there was no correction for inflow effects performed on the DCE-AIF measurement, which could cause underestimation of the peak concentration. Indeed, in a later study from the group [40], the temporal resolution was proven to be the key factor for obtaining high quality DCE-AIF measurements

and yielding better reproducibility of DCE parameters.

Most commonly a linear relation is assumed between the transverse relaxation change and the contrast concentration when deriving the DSC-AIF, as we did in this study. Yet, others argued that the relationship between the contrast concentration and the signal change in blood is better modeled by a quadratic expression, albeit dependent on the hematocrit level [5–8]. In practice, however, the hematocrit level is not always known. Furthermore, this will vary across the vasculature, e.g. there will be a higher hematocrit level in the smallest vessels. Also, the "arterial" voxels often combines both blood and tissue signals with unknown proportion, which increases the linearity of the relation between contrast concentration and the signal changes [7]. These issues complicate the application of the quadratic model. In order to calculate aCBF based on the DSC-AIFs, we used an assumed proportionality ($r_2^*$) for DSC-AIFs derived by a linear approximation of the quadratic model which was adjusted for hematocrit level [8]: 16.5 $(\text{mM}\cdot\text{s})^{-1}$. Alternatively, it was theoretically assumed to be 5.9 $(\text{mM}\cdot\text{s})^{-1}$ in Calamante et al. [41] and Pedersen et al. [42]. Lind and her colleagues derived a linear constant equal to 89 $(\text{mM}\cdot\text{s})^{-1}$ by combining quantitative susceptibility mapping with DSC measurements [43]. Furthermore, Knutsson proposed an approximated value: 20 $(\text{mM}\cdot\text{s})^{-1}$ by linear fitting the quadratic model (with the contrast concentration from 0 to 10 mM) [44]. These figures signify that there is no consensus regarding an optimal $r_2^*$ constant for quantifying AIF in DSC MRI. By applying the AIF derived from the DCE images, we could bypass such quantification issues.

The smaller variation in rCBF estimates using the DCE-AIFs in our opinion reflects that this approach is more reliable and consistent than when using the DSC-AIFs. In practice, only one vessel (or slice) is chosen as the AIF source. Therefore, location independency of the AIF is preferred for optimal consistency and to yield reduced operation bias in perfusion imaging. The average aCBF estimated with DCE-AIFs in healthy GM and WM were 51.5±7.8 and 24.3±3.9 (unit: ml/100g/min), respectively. These are close to CBF values obtained by previous MRI [44–48], CT [49] and PET [50–52] studies. The average aCBF obtained with the DSC-AIFs was larger than most reported ranges, both for GM as well as for WM. One should notice that a wide range of perfusion values can be found in literature. Therefore, we should be cautious not to overinterpret these numbers. However, the obtained CBF values when using DCE-AIFs seem to be more in line with literature values. Clearly, only a comparison to a true gold standard measured simultaneously would be conclusive.

The rCBV is a biomarker that is often applied clinically to characterize brain tumors and to monitor treatment response [53–57]. Since it is calculated as the ratio between the area under the tissue concentration curve and the integral under the curve of the first bolus passage of the AIF, it is directly affected by the choice for a particular AIF. Essentially, the area under the first contrast passage acts as a scaling factor of the CBV. This also implies that when calculating the ratio of CBVs from a tumorous region and a collateral ROI, such effects will cancel out. CBF-values can, however, be more non-linearly dependent on the shape of the

AIF. Statistics on the area under the first passage of our AIFs is included in the supplementary material. It confirms the larger variation of the DSC-AIFs compared to the DCE-AIFs.

Our results may indicate that clinical research could be improved as follows. First, DCE imaging could enhance perfusion analysis from DSC MRI by providing a more reliable AIF. Such a DCE sequence can be acquired with minimal loss of imaging time, since the AIF can be measured during injection of the preload bolus. In our study, we employed a longer DCE sequence, since we also aim to improve leakage quantification by combining DCE and DSC analysis in our future work; this is however not necessary when the only goal is to measure the AIF. For that purpose the same scan-duration as the DSC sequence could be chosen. Second, having a DCE-AIF in absolute concentration units, could allow for making CBV, CBF and MTT measurements from DSC MRI more quantitative. Clearly, a remaining obstacle would be the lack of a suitable transformation, linear or nonlinear, to convert the DSC tissue signal into physical contrast concentration units. When the relaxivities of different tissue-types such as GM, WM, tumor and necrotic tissue could be estimated, however, then an accurate aCBF map in every individual could be generated.



There are several limitations of our study. First, the employed echo time (45 ms) is longer than what currently is advised (i.e. 25-35 ms)[58]. Moreover, we did not have a ground truth AIF in our study as this can only be obtained by arterial blood sampling. Also, a ground truth CBF was not available for similar reasons. In addition, the aCBF was derived with a particular $r_2^*$ value for tissue and blood (to convert the DSC signal to contrast agent concentration). While the $r_2^*$ in both tissue and blood is still under debate, clearly our results will vary with different $r_2^*$ values for tissue or blood. Finally, the injection dose was not adjusted according to patient weight, but fixed at 7.5 ml for all patients. This bias was corrected by using an AIF model with normalized area under the bolus peak.

## 3.5. CONCLUSION

We conclude that the DCE-based AIFs are efficiently obtained during the preload contrast agent injection prior to DSC imaging. DCE-based AIFs reproduce better across vessels than the DSC-based AIFs, and can therefore improve the reliability of assessing perfusion parameters from DSC MRI. In addition, the quantitative nature of DCE-AIFs demonstrates great potential for truly quantifying perfusion parameter estimates from DSC MRI.

## 3.6. SUPPLEMENTARY MATERIALS

### 3.6.1. OPTIMIZATION OF THE SEMI-AUTOMATIC DSC-AIF ALGORITHM

In its default setting the semi-automatic DSC-AIF algorithm searches for arterial-like voxels in a central elliptic region in a chosen slice and the algorithm stops when 4 to 6 voxels have been automatically detected. One such group and corresponding

AIF curves are shown in Figure S3.1a and b respectively. Figure S3.1c represents the search result while increasing the voxel number limit to between 10 to 20 voxels. The detected AIFs show wider peaks, including bimodal profiles (Figure S3.1d). In Figure S3.1e, the elliptic search area was positioned in region of the manually annotated DCE-AIF voxels (see Figure 3.2). The detected AIFs appear more noisy and contain more fluctuations than the AIF with default search region (Figure S3.1f). Because of the poor AIF profiles with these modified settings, the original approach was applied throughout the paper.



### 3.6.2. THE AREA UNDER FIRST CONTRAST PASSAGE

Table S3.1 collates the CV of the areas under first contrast passage of the AIFs, i.e. the ratio of the standard deviation and the mean value calculated over five measurements in each patient. These data show that the area under the first contrast agent passage curve of DCE-AIF has less variation than the area under first passage of DSC-AIFs, both within and between patients. In effect, the CBV would show less variation with the DCE-AIFs.

Table S3.1: CV of area under the first bolus peak for the different patients and measurement methods.

| | DCE-AIF | Manual DSC-AIF | Semi-automatic DSC-AIF |
|---|---|---|---|
| Patient 1 | 0.10 | 0.41 | 0.19 |
| Patient 2 | 0.03 | 0.37 | 0.19 |
| Patient 3 | 0.02 | 0.09 | 0.23 |
| Patient 3 † | 0.12 | 0.27 | 0.13 |
| Patient 4 † | 0.04 | 0.10 | 0.24 |
| Patient 5 | 0.22 | 0.33 | 0.27 |
| Patient 6 | 0.15 | 0.26 | 0.07 |
| Patient 7 † | 0.05 | 0.36 | 0.18 |
| Patient 8 | 0.10 | 0.14 | 0.28 |
| Patient 9 | 0.09 | 0.29 | 0.27 |
| Patient 10 | 0.10 | 0.18 | 0.45 |
| Average | 0.09 | 0.26 | 0.23 |

† Patient received radiation therapy

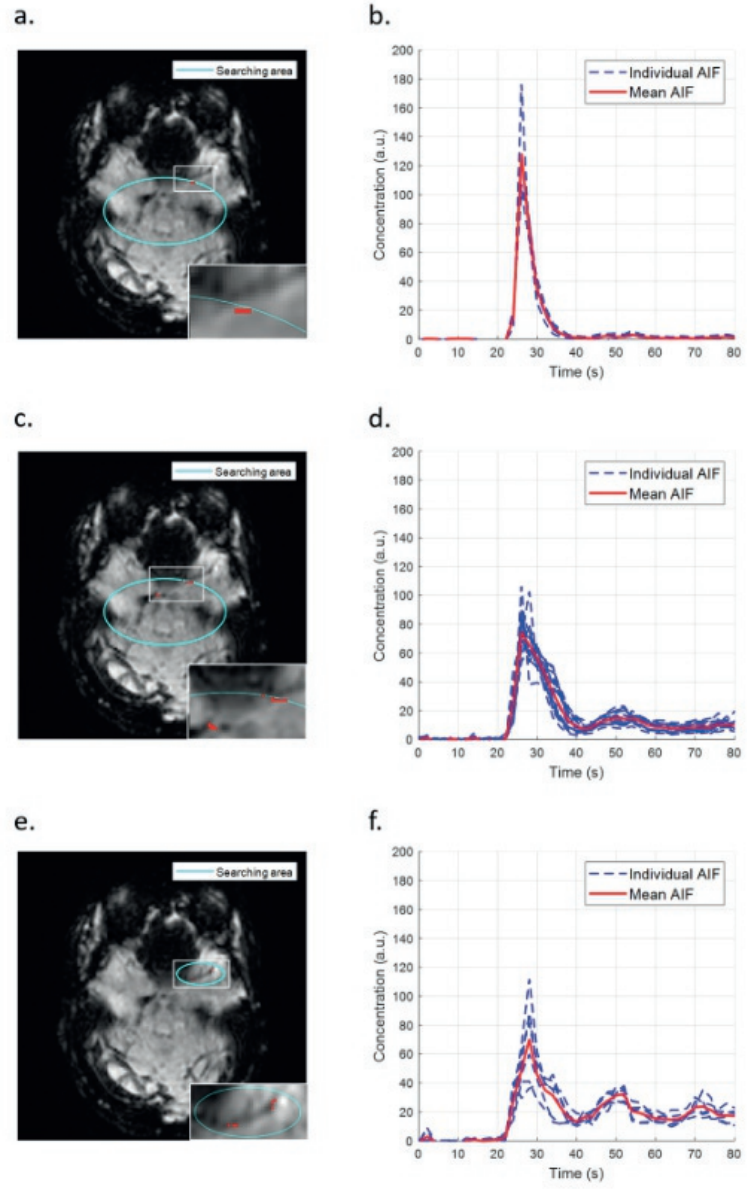


Figure S3.1: The optimizing process of the applied semi-automatic algorithm and the corresponding detected AIF curves.

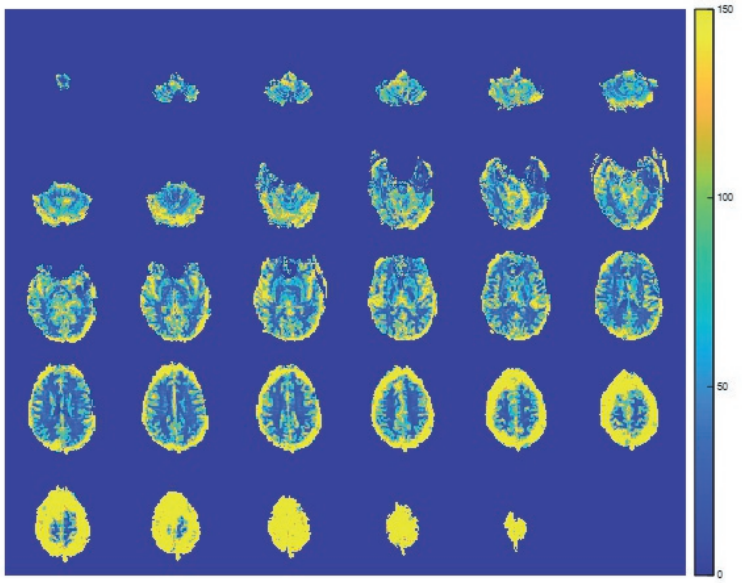


Figure S3.2: The aCBF map from patient 6. An overall overestimation and 'ring artefact' were observed.

# REFERENCES


[1] L. Østergaard *et al.* "High resolution measurement of cerebral blood flow using intravascular tracer bolus passages. Part I: Mathematical approach and statistical analysis". In: *Magnetic Resonance in Medicine* 36.5 (Nov. 1996), pp. 715–725. ISSN: 07403194. DOI: 10.1002/mrm.1910360510.

[2] F. Calamante. "Perfusion MRI using dynamic-susceptibility contrast MRI: quantification issues in patient studies." In: *Topics in magnetic resonance imaging : TMRI* 21.2 (Apr. 2010), pp. 75–85. ISSN: 1536-1004. DOI: 10.1097/RMR.0b013e31821e53f5.

[3] A. Huang, C.-W. Lee, and H.-M. Liu. "Time to peak and full width at half maximum in MR perfusion: valuable indicators for monitoring moyamoya patients after revascularization". In: *Scientific Reports* 11.1 (Dec. 2021), p. 479. ISSN: 2045-2322. DOI: 10.1038/s41598-020-80036-3.

[4] K. Zierler. "Indicator dilution methods for measuring blood flow, volume, and other properties of biological systems: a brief history and memoir." In: *Annals of biomedical engineering* 28.8 (Aug. 2000), pp. 836–48. ISSN: 0090-6964. DOI: 10.1114/1.1308496.

[5] M. J. P. Van Osch *et al.* "Measuring the arterial input function with gradient echo sequences". In: *Magnetic Resonance in Medicine* 49.6 (June 2003), pp. 1067–1076. ISSN: 0740-3194. DOI: 10.1002/mrm.10461.

[6] E. Akbudak, M. Kotys, and Conturo T. "Quadraticity and haematocrit dependence of ΔR2* AIF signals at 3T: a blood phantom study under physiologic conditions. Syllabus of the ISMRM workshop on quantitative cerebral perfusion imaging using MRI; a technical perspective." In: *Syllabus of the ISMRM workshop on quantitative cerebral perfusion imaging using MRI; a technical perspective*. Venice, 2004.

[7] B. Kjølby, L. Østergaard, and V. Kiselev. "Theoretical model of intravascular paramagnetic tracers effect on tissue relaxation". In: *Magnetic Resonance in Medicine* 56.1 (July 2006), pp. 187–197. ISSN: 0740-3194. DOI: 10.1002/mrm.20920.

[8] D. Van Dorth *et al.* "Dependency of R2 and R2* relaxation on Gd-DTPA concentration in arterial blood: Influence of hematocrit and magnetic field strength". In: *NMR in Biomedicine* 35.5 (May 2022). ISSN: 0952-3480. DOI: 10.1002/nbm.4653.

[9] M. J. P. Van Osch *et al.* "Correcting partial volume artifacts of the arterial input function in quantitative cerebral perfusion MRI". In: *Magnetic Resonance in Medicine* 45.3 (Mar. 2001), pp. 477–485. ISSN: 0740-3194. DOI: 10.1002/1522-2594(200103)45:3<477::AID-MRM1063>3.0.CO;2-4.

[10] M. Ebinger *et al.* "Reliable perfusion maps in stroke MRI using arterial input functions derived from distal middle cerebral artery branches." In: *Stroke* 41.1 (Jan. 2010), pp. 95–101. ISSN: 1524-4628. DOI: 10.1161/STROKEAHA.109.559807.

[11] M. Rausch *et al.* “Analysis of input functions from different arterial branches with gamma variate functions and cluster analysis for quantitative blood volume measurements.” In: *Magnetic resonance imaging* 18.10 (Dec. 2000), pp. 1235–43. ISSN: 0730-725X. DOI: 10.1016/s0730-725x(00)00219-8.

[12] Y. Shen *et al.* “T1 relaxivities of gadolinium-based magnetic resonance contrast agents in human whole blood at 1.5, 3, and 7 T.” In: *Investigative radiology* 50.5 (May 2015), pp. 330–8. ISSN: 1536-0210. DOI: 10.1097/RLI.0000000000000132.

[13] C. Roberts *et al.* “The effect of blood inflow and B(1)-field inhomogeneity on measurement of the arterial input function in axial 3D spoiled gradient echo dynamic contrast-enhanced MRI.” In: *Magnetic resonance in medicine* 65.1 (Jan. 2011), pp. 108–19. ISSN: 1522-2594. DOI: 10.1002/mrm.22593.

[14] A. Garpebring *et al.* “Effects of inflow and radiofrequency spoiling on the arterial input function in dynamic contrast-enhanced MRI: a combined phantom and simulation study.” In: *Magnetic resonance in medicine* 65.6 (June 2011), pp. 1670–9. ISSN: 1522-2594. DOI: 10.1002/mrm.22760.

[15] H. Wang and Y. Cao. “Correction of arterial input function in dynamic contrast-enhanced MRI of the liver.” In: *Journal of magnetic resonance imaging : JMRI* 36.2 (Aug. 2012), pp. 411–21. ISSN: 1522-2586. DOI: 10.1002/jmri.23636.

[16] K. Murase. “Efficient method for calculating kinetic parameters using T1-weighted dynamic contrast-enhanced magnetic resonance imaging.” In: *Magnetic resonance in medicine* 51.4 (Apr. 2004), pp. 858–62. ISSN: 0740-3194. DOI: 10.1002/mrm.20022.

[17] J. J. N. Van Schie *et al.* “Estimating the arterial input function from dynamic contrast-enhanced MRI data with compensation for flow enhancement (I): Theory, method, and phantom experiments”. In: *Journal of Magnetic Resonance Imaging* 47.5 (May 2018), pp. 1190–1196. ISSN: 10531807. DOI: 10.1002/jmri.25906.

[18] C. de Bazelaire *et al.* “Combined T2* and T1 measurements for improved perfusion and permeability studies in high field using dynamic contrast enhancement”. In: *European Radiology* 16.9 (Sept. 2006), pp. 2083–2091. ISSN: 0938-7994. DOI: 10.1007/s00330-006-0198-1.

[19] C. C. Quarles *et al.* “A theoretical framework to model DSC-MRI data acquired in the presence of contrast agent extravasation”. In: *Physics in Medicine and Biology* 54.19 (Oct. 2009), pp. 5749–5766. ISSN: 0031-9155. DOI: 10.1088/0031-9155/54/19/006.

[20] J. L. Boxerman *et al.* “The Role of Preload and Leakage Correction in Gadolinium-Based Cerebral Blood Volume Estimation Determined by Comparison with MION as a Criterion Standard”. In: *American Journal of Neuroradiology* 33.6 (June 2012), pp. 1081–1087. ISSN: 0195-6108. DOI: 10.3174/ajnr.A2934.

[21] M. Saranathan *et al.* “DIfferential subsampling with cartesian ordering (DISCO): A high spatio-temporal resolution dixon imaging sequence for multiphasic contrast enhanced abdominal imaging”. In: *Journal of Magnetic Resonance Imaging* 35.6 (June 2012), pp. 1484–1492. ISSN: 10531807. DOI: 10.1002/jmri.23602.

[22] K. J. Friston *et al.* “Statistical parametric maps in functional imaging: A general linear approach”. In: *Human Brain Mapping* 2.4 (1994), pp. 189–210. ISSN: 10659471. DOI: 10.1002/hbm.460020402.

[23] D. Peruzzo *et al.* “Automatic selection of arterial input function on dynamic contrast-enhanced MR images”. In: *Computer Methods and Programs in Biomedicine* 104.3 (Dec. 2011), e148–e157. ISSN: 01692607. DOI: 10.1016/j.cmpb.2011.02.012.

[24] M. R. Orton *et al.* "Computationally efficient vascular input function models for quantitative kinetic modelling using DCE-MRI." In: *Physics in medicine and biology* 53.5 (Mar. 2008), pp. 1225–39. ISSN: 0031-9155. DOI: 10.1088/0031-9155/53/5/005.

[25] N. Wake *et al.* "Accuracy and precision of quantitative DCE-MRI parameters: How should one estimate contrast concentration?" In: *Magnetic Resonance Imaging* 52 (Oct. 2018), pp. 16–23. ISSN: 0730725X. DOI: 10.1016/j.mri.2018.05.007.

[26] X. Zhang *et al.* "In vivo blood T1 measurements at 1.5 T, 3 T, and 7 T". In: *Magnetic Resonance in Medicine* 70.4 (Oct. 2013), pp. 1082–1086. ISSN: 07403194. DOI: 10.1002/mrm.24550.

[27] L. Østergaard *et al.* "High resolution measurement of cerebral blood flow using intravascular tracer bolus passages. Part II: Experimental comparison and preliminary results". In: *Magnetic Resonance in Medicine* 36.5 (Nov. 1996), pp. 726–736. ISSN: 07403194. DOI: 10.1002/mrm.1910360511.

[28] K. A. Rempp *et al.* "Quantification of regional cerebral blood flow and volume with dynamic susceptibility contrast-enhanced MR imaging." In: *Radiology* 193.3 (Dec. 1994), pp. 637–641. ISSN: 0033-8419. DOI: 10.1148/radiology.193.3.7972800.

[29] O. Wu *et al.* "Tracer arrival timing-insensitive technique for estimating flow in MR perfusion-weighted imaging using singular value decomposition with a block-circulant deconvolution matrix". In: *Magnetic Resonance in Medicine* 50.1 (July 2003), pp. 164–174. ISSN: 07403194. DOI: 10.1002/mrm.10522.

[30] E. Lind *et al.* "Assessment of MRI contrast agent concentration by quantitative susceptibility mapping (QSM): application to estimation of cerebral blood volume during steady state." In: *Magma (New York, N.Y.)* 30.6 (Dec. 2017), pp. 555–566. ISSN: 1352-8661. DOI: 10.1007/s10334-017-0637-9.

[31] E. Kellner *et al.* "Arterial input function measurements for bolus tracking perfusion imaging in the brain." In: *Magnetic resonance in medicine* 69.3 (Mar. 2013), pp. 771–80. ISSN: 1522-2594. DOI: 10.1002/mrm.24319.

[32] E. Kellner *et al.* "Arterial input function in a dedicated slice for cerebral perfusion measurements in humans." In: *Magma (New York, N.Y.)* 31.3 (June 2018), pp. 439–448. ISSN: 1352-8661. DOI: 10.1007/s10334-017-0663-7.

[33] L. Knutsson *et al.* "Dynamic susceptibility contrast MRI with a prebolus contrast agent administration design for improved absolute quantification of perfusion." In: *Magnetic resonance in medicine* 72.4 (Oct. 2014), pp. 996–1006. ISSN: 1522-2594. DOI: 10.1002/mrm.25006.

[34] F. Calamante. "Arterial input function in perfusion MRI: a comprehensive review." In: *Progress in nuclear magnetic resonance spectroscopy* 74 (Oct. 2013), pp. 1–32. ISSN: 1873-3301. DOI: 10.1016/j.pnmrs.2013.04.002.

[35] K. Murase *et al.* "Determination of arterial input function using fuzzy clustering for quantification of cerebral blood flow with dynamic susceptibility contrast-enhanced MR imaging." In: *Journal of magnetic resonance imaging : JMRI* 13.5 (May 2001), pp. 797–806. ISSN: 1053-1807. DOI: 10.1002/jmri.1111.

[36] T. J. Carroll, H. A. Rowley, and V. M. Haughton. "Automatic Calculation of the Arterial Input Function for Cerebral Perfusion Imaging with MR Imaging". In: *Radiology* 227.2 (May 2003), pp. 593–600. ISSN: 0033-8419. DOI: 10.1148/radiol.2272020092.

[37] K. Mouridsen *et al.* “Automatic selection of arterial input function using cluster analysis”. In: *Magnetic Resonance in Medicine* 55.3 (Mar. 2006), pp. 524–531. ISSN: 0740-3194. DOI: 10.1002/mrm.20759.

[38] S.-H. You *et al.* “Differentiation of High-Grade from Low-Grade Astrocytoma: Improvement in Diagnostic Accuracy and Reliability of Pharmacokinetic Parameters from DCE MR Imaging by Using Arterial Input Functions Obtained from DSC MR Imaging”. In: *Radiology* 286.3 (Mar. 2018), pp. 981–991. ISSN: 0033-8419. DOI: 10.1148/radiol.2017170764.

[39] K. M. Kang *et al.* “Differentiation between glioblastoma and primary CNS lymphoma: application of DCE-MRI parameters based on arterial input function obtained from DSC-MRI”. In: *European Radiology* 31.12 (Dec. 2021), pp. 9098–9109. ISSN: 0938-7994. DOI: 10.1007/s00330-021-08044-z.

[40] W. H. Lim *et al.* “Assessing the reproducibility of high temporal and spatial resolution dynamic contrast-enhanced magnetic resonance imaging in patients with gliomas”. In: *Scientific Reports* 11.1 (Dec. 2021), p. 23217. ISSN: 2045-2322. DOI: 10.1038/s41598-021-02450-5.

[41] F. Calamante, E.-j. P. A. Vonken, and M. J. P. van Osch. “Contrast agent concentration measurements affecting quantification of bolus-tracking perfusion MRI.” In: *Magnetic resonance in medicine* 58.3 (Sept. 2007), pp. 544–53. ISSN: 0740-3194. DOI: 10.1002/mrm.21362.

[42] M. Pedersen *et al.* “Quantitative cerebral perfusion using the PRESTO acquisition scheme”. In: *Journal of Magnetic Resonance Imaging* 20.6 (Dec. 2004), pp. 930–940. ISSN: 10531807. DOI: 10.1002/jmri.20206.

[43] E. Lind *et al.* “Dynamic contrast-enhanced QSM for perfusion imaging: a systematic comparison of ΔR2*- and QSM-based contrast agent concentration time curves in blood and tissue”. In: *Magnetic Resonance Materials in Physics, Biology and Medicine* 33.5 (Oct. 2020), pp. 663–676. ISSN: 0968-5243. DOI: 10.1007/s10334-020-00831-x.

[44] L. Knutsson *et al.* “Effects of blood ΔR2* non-linearity on absolute perfusion quantification using DSC-MRI: Comparison with Xe-133 SPECT”. In: *Magnetic Resonance Imaging* 31.5 (June 2013), pp. 651–655. ISSN: 0730725X. DOI: 10.1016/j.mri.2012.12.001.

[45] T. J. Carroll *et al.* “Quantification of cerebral perfusion using the “bookend technique”: an evaluation in CNS tumors”. In: *Magnetic Resonance Imaging* 26.10 (Dec. 2008), pp. 1352–1359. ISSN: 0730725X. DOI: 10.1016/j.mri.2008.04.010.

[46] M. Günther, M. Bock, and L. R. Schad. “Arterial spin labeling in combination with a look-locker sampling strategy: Inflow turbo-sampling EPI-FAIR (ITS-FAIR)”. In: *Magnetic Resonance in Medicine* 46.5 (Nov. 2001), pp. 974–984. ISSN: 07403194. DOI: 10.1002/mrm.1284.

[47] W. Shin *et al.* “Quantitative cerebral perfusion using dynamic susceptibility contrast MRI: evaluation of reproducibility and age- and gender-dependence with fully automatic image postprocessing algorithm.” In: *Magnetic resonance in medicine* 58.6 (Dec. 2007), pp. 1232–41. ISSN: 0740-3194. DOI: 10.1002/mrm.21420.

[48] E. T. Petersen *et al.* “The QUASAR reproducibility study, Part II: Results from a multi-center Arterial Spin Labeling test-retest study.” In: *NeuroImage* 49.1 (Jan. 2010), pp. 104–13. ISSN: 1095-9572. DOI: 10.1016/j.neuroimage.2009.07.068.

[49] H. Okazawa *et al.* "Quantitative Comparison of the Bolus and Steady-State Methods for Measurement of Cerebral Perfusion and Oxygen Metabolism: Positron Emission Tomography Study Using 15O-Gas and Water". In: *Journal of Cerebral Blood Flow & Metabolism* 21.7 (July 2001), pp. 793–803. ISSN: 0271-678X. DOI: 10.1097/00004647-200107000-00004.

[50] K. L. LEENDERS *et al.* "CEREBRAL BLOOD FLOW, BLOOD VOLUME AND OXYGEN UTILIZATION". In: *Brain* 113.1 (1990), pp. 27–47. ISSN: 0006-8950. DOI: 10.1093/brain/113.1.27.

[51] H. Ito *et al.* "Database of normal human cerebral blood flow, cerebral blood volume, cerebral oxygen extraction fraction and cerebral metabolic rate of oxygen measured by positron emission tomography with 15O-labelled carbon dioxide or water, carbon monoxide and oxygen: a multicentre study in Japan." In: *European journal of nuclear medicine and molecular imaging* 31.5 (May 2004), pp. 635–43. ISSN: 1619-7070. DOI: 10.1007/s00259-003-1430-8.

[52] E. Rostrup *et al.* "Cerebral hemodynamics measured with simultaneous PET and near-infrared spectroscopy in humans." In: *Brain research* 954.2 (Nov. 2002), pp. 183–93. ISSN: 0006-8993. DOI: 10.1016/s0006-8993(02)03246-8.

[53] M. Law *et al.* "Low-grade gliomas: dynamic susceptibility-weighted contrast-enhanced perfusion MR imaging–prediction of patient clinical response." In: *Radiology* 238.2 (Feb. 2006), pp. 658–67. ISSN: 0033-8419. DOI: 10.1148/radiol.2382042180.

[54] P. Kickingereder *et al.* "Relative cerebral blood volume is a potential predictive imaging biomarker of bevacizumab efficacy in recurrent glioblastoma." In: *Neuro-oncology* 17.8 (Aug. 2015), pp. 1139–47. ISSN: 1523-5866. DOI: 10.1093/neuonc/nov028.

[55] L. C. Bell *et al.* "Evaluating the Use of rCBV as a Tumor Grade and Treatment Response Classifier Across NCI Quantitative Imaging Network Sites: Part II of the DSC-MRI Digital Reference Object (DRO) Challenge." In: *Tomography (Ann Arbor, Mich.)* 6.2 (2020), pp. 203–208. ISSN: 2379-139X. DOI: 10.18383/j.tom.2020.00012.

[56] K. M. Schmainda *et al.* "Dynamic susceptibility contrast MRI measures of relative cerebral blood volume as a prognostic marker for overall survival in recurrent glioblastoma: results from the ACRIN 6677/RTOG 0625 multicenter trial." In: *Neuro-oncology* 17.8 (Aug. 2015), pp. 1148–56. ISSN: 1523-5866. DOI: 10.1093/neuonc/nou364.

[57] O. M. Henriksen *et al.* "High-Grade Glioma Treatment Response Monitoring Biomarkers: A Position Statement on the Evidence Supporting the Use of Advanced MRI Techniques in the Clinic, and the Latest Bench-to-Bedside Developments. Part 1: Perfusion and Diffusion Techniques." In: *Frontiers in oncology* 12 (2022), p. 810263. ISSN: 2234-943X. DOI: 10.3389/fonc.2022.810263.

[58] J. L. Boxerman *et al.* "Consensus recommendations for a dynamic susceptibility contrast MRI protocol for use in high-grade gliomas". In: *Neuro-Oncology* 22.9 (Sept. 2020), pp. 1262–1275. ISSN: 1522-8517. DOI: 10.1093/neuonc/noaa141.

# 4

# ARTERIAL INPUT FUNCTION ESTIMATION COMPENSATING FOR INFLOW AND PARTIAL VOLUMING IN DYNAMIC CONTRAST ENHANCED MRI

This chapter has been published as:
**Tseng C-H**, Nagtegaal MA, van Osch MJP, et al. Arterial input function estimation compensating for inflow and partial voluming in dynamic contrast-enhanced MRI. NMR in Biomedicine. 2024; 37(12):e5225. doi:10.1002/nbm.5225.

## ABSTRACT

Both inflow and partial volume effects (PVE) are sources of error when measuring the arterial input function (AIF) in dynamic contrast enhanced (DCE) MRI. This is relevant as errors in the AIF can propagate into pharmacokinetic parameter estimations from the DCE data. A method was introduced for flow correction by estimating and compensating the number of the perceived pulse of spins during inflow. We hypothesized that PVE has a similar impact on concentration time curves as inflow. Therefore, we aimed to study the efficiency of this method to compensate for both effects simultaneously. We first simulated an AIF with different levels of inflow and PVE contamination. The peak, full width at half maximum (FWHM) and area under curve (AUC) of the reconstructed AIFs were compared with the true (simulated) AIF. In clinical data, PVE was artificially included in AIFs by averaging the signal in voxels surrounding a manually selected point in an artery. Subsequently, the artificial partial volume AIFs were corrected and compared to the AIF from the selected point. Additionally, corrected AIFs from the internal carotid artery (ICA), middle cerebral artery (MCA) and the venous output function (VOF) estimated from the superior sagittal sinus (SSS) were compared. As such we aimed to investigate the effectiveness of the correction method with different levels of inflow and PVE in clinical data. The simulation data demonstrated that the corrected AIFs had only marginal bias in peak value, FWHM and AUC. Also, the algorithm yielded highly correlated reconstructed curves over increasingly larger neighbourhoods surrounding selected arterial points in clinical data. Furthermore, AIFs measured from ICA and MCA produced similar peak height and FWHM, whereas a significantly larger peak and lower FWHM was found compared to the VOF. Our findings indicate that the proposed method has high potential to compensate for PVE and inflow simultaneously. The corrected AIFs could thereby provide a stable input source for DCE analysis.

## 4.1. INTRODUCTION

Dynamic contrast enhanced (DCE) MRI is an often used imaging method for estimating vascular properties, especially in oncological applications [1]. Essentially, a gadolinium-based contrast agent (GBCA) is intravenously administered, while dynamic $T_1$-weighted images are acquired for several minutes at a medium temporal resolution (on the order of a few seconds). In normal brain tissue, an intact blood brain barrier (BBB) prevents leakage of GBCA into tissue. However, impairment of the BBB resulting from disease processes can lead to leakage of GBCA from vessels to the extravascular space. To identify such BBB damage and quantify its extent, parameters including the time to the peak [2], maximum intensity [3], the area under curve (AUC) [4], wash-in slope, wash-out rate, and signal enhancement ratio [5], can be derived from the DCE signal-intensity curve [6]. Alternatively, tracer kinetic models enable estimation of vascular properties (as summarized by Khalifa et al. [7]). The extended Tofts model (ETM) is the most frequently applied model in tumor assessment. It assumes that the GBCA distributes in two compartments: the blood plasma and the extravascular extracellular space (EES), adopting a bi-directional exchange of the tracer across the BBB [8]. By fitting this model to the measured signal intensity, vascular parameters are obtained, e.g. the volume transfer constant ($K^{trans}$), reflux exchange rate from EES to plasma ($K_{ep}$), fraction volume of plasma ($V_p$), and fraction volume of EES ($V_e$). These quantitative parameters were shown to provide relevant clinical information about the vasculature [9, 10].

The arterial input function (AIF) plays a crucial role in the estimation of the aforementioned pharmacokinetic model parameters as it serves as the input to the model. The AIF describes the contrast agent concentration in an artery feeding the tissue of interest as a function of time. The use of a population-average AIF has been proposed to simplify the fitting procedure and enhance the reproducibility of the parameter estimations [11]. However, a population-average AIF ignores the natural variation in individual subjects, which can erroneously propagate to vascular parameter estimations [12, 13].

Simultaneously, there are also known issues with measuring a subject specific AIF. In general, it is preferred that the AIF is obtained near the tissue of interest to reduce travel time (delay) and dispersion, so that the shape and amplitude of AIFs is accurately represented [14]. However, in the smaller arteries and even in the larger brain-feeding arteries, limited spatial resolution can result in mixing of signals: the partial volume effect (PVE) [15, 16]. As a consequence, signals from the artery and surrounding tissue are combined, which generally results in underestimation of the GBCA concentration. To deal with this, previous studies have suggested either to normalize the AIF with the concentration measured in the superior sagittal sinus (SSS) [16, 17], i.e. the venous output function (VOF), or to use the VOF itself as an input to the pharmacokinetic model [18, 19]. Nonetheless, Hansen et al. [16] pointed out that normalization methods are only valid when the contribution of the tissue signal is limited. Furthermore, Cramer et al. [20] found that using the VOF might lead to biased pharmacokinetic analysis due to the increased dispersion of the concentration-time curve.

Inflow effects have shown to affect the AIF, especially when it is measured in a larger artery, away from the site of interest [21]. In general, it is assumed that the recorded signal reflects the steady state magnetization. In tissue this is often a valid assumption, but this may not hold in arteries. Here, "fresh" spins continuously arrive in the image volume, which have received insufficient excitations to reach steady state. Effectively, this results in a hyperintense signal in the baseline images and underestimation of the $T_1$ signal enhancement induced by the GBCA. Several methods for reducing the impact of inflow effects were proposed. For instance, a flow phantom could be used to calibrate the effect [22]. However, such calibration is often sequence, subject, and system dependent. Measuring the AIF downstream could significantly improve the accuracy, but this may not be applicable to all in vivo imaging situations [23]. As an alternative, the AIF can be measured from phase accumulation induced by higher magnetic susceptibility of GBCA. This approach is insensitive to inflow effects that merely act on the magnitude of the signal [24]. At the same time, however, this signal can suffer from phase wrapping and flow-induced phase shift. Yet, other correction methods were designed for particular applications, e.g. liver DCE imaging [25, 26], and therefore are not generally applicable.



Recently, a method was proposed for correcting inflow effects by first estimating the perceived pulse number and then correcting for the inflow effect [27]. However, PVEs were not considered. In the current paper we aim to assess the efficacy of this algorithm to compensate for *both* inflow *and* PVEs simultaneously. We hypothesize that PVE can be interpreted as an underestimation of the perceived pulse number due to its similar impact on concentration-time curves. Simulation data was used to evaluate the correction method and clinical datasets were applied to verify the applicability in practice.

## 4.2. THEORY

In this section we define the theory that was initially applied merely for modeling and correcting of inflow, c.q. a low number of perceived pulses. The full derivation of the introduced equations can be found in the appendix of van Schie et al. [27].

### 4.2.1. SIGNAL EXPRESSION

In a spoiled gradient echo sequence, the signal can be expressed as an excitation of the longitudinal magnetization $M_z(n)$ followed by $T_2^*$ decay:

$$S(n) = \sin\alpha \cdot M_z(n) \cdot \exp\left(\frac{-TE}{T_2^*}\right), \tag{4.1}$$

in which $\alpha$ is the flip angle, $TE$ is the echo time, $T_2^*$ is the tissue specific $T_2^*$-decay time, and $n$ represents the perceived number of RF-pulses by the spins, which directly reflects the degree of saturation. Clearly, the $T_2^*$-decay term may be neglected while the applied echo time is sufficiently small ($TE \ll T_2^*$).

The expression for $M_z(n)$ is:

$$M_z(n) = M_0 \cdot \left( \left( 1 - \frac{1 - E_1}{1 - \cos\alpha \cdot E_1} \right) \cdot (\cos(\alpha) \cdot E_1)^n + \frac{1 - E_1}{1 - \cos\alpha \cdot E_1} \right), \tag{4.2}$$

where

$$E_1 = \exp\left( \frac{-TR}{T_1} \right) \tag{4.3}$$

with $M_0$ the net magnetization in equilibrium, $TR$ the repetition time, and $T_1$ the longitudinal relaxation time. Notice that when the spins have received enough excitation pulses, which is usually achieved in stationary tissue due to a sufficiently large number of start-up excitations, the longitudinal magnetization reaches a steady state, in which $M_z(n)$ can be simplified as:

$$M_z(n) = M_0 \cdot \left( \frac{1 - E_1}{1 - \cos\alpha \cdot E_1} \right). \tag{4.4}$$

The magnetic unit won't alter with increasing perceived pulse number n at some point. Notice that this 'sufficient' pulse number to saturate the magnetization is depended on the applied repetition time and flip angle. The MRI signal in an artery, however, frequently does not reach the steady state, because spins enter the field of view with an inadequate number of excitation pulses, albeit still abiding to Equation (4.2). As a consequence, a higher signal is obtained from these spins that are in a transient state compared to what would have been measured had they been in a steady state. This leads to the phenomenon of inflow artefacts due to flow enhancement.

### 4.2.2. GBCA-INDUCED SIGNAL CHANGE

Under the influence of the GBCA, relaxation rates are modulated by the contrast concentration $C$ in plasma:

$$\frac{1}{T_1} = \frac{1}{T_{10}} + (1 - Hct) \cdot r_1 \cdot C, \tag{4.5}$$

and

$$\frac{1}{T_2^*} = \frac{1}{T_{20}^*} + (1 - Hct) \cdot r_2^* \cdot C, \tag{4.6}$$

in which $T_{10}$ and $T_{20}^*$ represent the initial longitudinal and transverse relaxation time, respectively, $Hct$ is the hematocrit level, and $r_1$ and $r_2^*$ denote the longitudinal and transverse relaxivity of the GBCA. As a result of this, the magnetization and the measured signal become functions of both $C$ and perceived pulse number ($n$): $M_z(C, n)$ and $S(C, n)$.

The signal ratio, denoted as $D$, characterizes the relative change between the

post-contrast and pre-contrast signal intensities, which can be expressed as:

$$D(C,n) = \frac{S(C,n)}{S(0,n)} = \frac{M_z(C,n)}{M_z(0,n)} \cdot e^{-TE \cdot r_2^* \cdot C}. \tag{4.7}$$

This signal ratio expression contains only two unknown terms that are the contrast concentration ($C$) and the perceived pulse number ($n$).

### 4.2.3. AIF MODEL

The AIF model from Orton et al. [28] was integrated in this approach to facilitate the correction for inflow. This AIF model is defined as a sum of two functions, one describing the first passage of the contrast agent and the other describing the wash-out phase of the GBCA during the tail of the AIF. The bolus peak $C_B(t)$ is defined by:

$$C_B(t-t_0) = a_B \cdot \mu_B^2 \cdot (t-t_0) \cdot e^{-\mu_B \cdot (t-t_0)}, \tag{4.8}$$

in which $a_B$ represented the area under the first bolus peak (that is related to the total injected concentration, see below), $\mu_B$ the decay rate and $t_0$ is the bolus arrival time. The tail function is expressed as a convolution of the bolus peak and a body transfer function $G(t)$:

$$G(t) = a_G \cdot e^{-\mu_G \cdot t}, \tag{4.9}$$

where $a_G$ determined the starting level of this function and $\mu_G$ governed the decay rate reflecting kidney function. Thus, the complete AIF is modeled as follows:

$$C_{\text{Orton}}(t,\theta) = C_B(t-t_0) + C_B(t-t_0) * G(t), \tag{4.10}$$

in which $\theta$ contains all parameters for the AIF:

$$\theta = [a_B, \mu_B, a_G, \mu_G, t_0]. \tag{4.11}$$

### 4.2.4. CORRECTION METHOD

This section summarizes the correction method. For further details we refer to the comprehensive description in van Schie et al. [27].

Previously, it was observed that the area under the first bolus peak is related to the ratio of contrast agent dose and cardiac output [22]. Furthermore, both dose and cardiac output are generally proportional to body weight [29]. Accordingly, the parameter representing the area under the first bolus peak of the AIF model ($a_B$) was assumed to be constant across subjects. This constant was set to 50.58 $\text{mM} \cdot \text{s}^{-1}$ for a standard dosage (0.1 mmol/kg) [27, 28], and was scaled linearly with the dose per body mass. Consequently, any discrepancies between the model and a measured signal-ratio curve were attributed to inflow effects, which was subsequently accounted for by estimating the perceived pulse number $n$.

To correct the measured AIF signal curve, the following minimization problem

was solved:

$$(\hat{\theta}, \hat{n}) = \arg\min_{\theta,n} \| D_{\text{meas}}(t) - D(C_{\text{Orton}}(t,\theta), n) \|_2, \tag{4.12}$$

in which $D_{\text{meas}}(t)$ is the measured signal ratio curve, and $D(C_{\text{Orton}}(t,\theta), n)$ is the fitted signal ratio curve incorporating Orton's AIF-model. While doing so, the free model parameters in $\theta$ (Equation (4.11)) and the perceived pulse number $n$ were estimated. The estimated parameters were constrained to be positive, and were determined using a nonlinear least squares regression method.

Essentially, the estimation of $n$ involved comparing the full measured time-series data to the AIF-model, rather than considering each time point separately. However, in practice some information might not be represented in the model, such as the presence of a second peak. To address this, the concentration ($C(t)$) at each time point was subsequently re-estimated using the estimated pulse number ($\hat{n}$), by solving C in:

$$D(C(t), \hat{n}) = D_{\text{meas}}(t). \tag{4.13}$$

In effect this yielded the final AIF concentration curve compensating for inflow effects and in this study we will study whether this also compensates for PVE.

## 4.3. MATERIALS AND METHODS

### 4.3.1. SIMULATION

The AIF model in Section 4.2.3 was used to generate a standardized AIF concentration curve using population-averaged parameters: $a_B$=50.58 mM$\cdot$s$^{-1}$, $\mu_B$=0.3 s$^{-1}$, $a_G$=0.02 s$^{-1}$, $\mu_G$=0.003 s$^{-1}$ and $t_0$=15 s [28]. The AIF curve first served to compute an MR signal curve according to Equation (4.1) (via Equation (4.2) and (4.3)) with $T_1$ and $T_2^*$ modulated by the contrast concentration. In this computation these constants were applied: $Hct$: 0.45, $T_{10}$ in blood: 1.8 s [30], $T_{20}^*$ in blood: 0.02 s [31], $r_1$: 4.5 (mM$\cdot$s)$^{-1}$ for gadobutrol [32], and a theoretical $r_2^*$: 5.9 (mM$\cdot$s)$^{-1}$ [33, 34].This was done for a variety of perceived pulse numbers n, yielding different MR signal curves $S(C,n)$, each of which was normalized according to Equation (4.7). Notice that $T_2^*$ decay was included, even though a small echo time was applied for the in vivo experiments. Inflow simulations ignoring $T_2^*$ decay were also explored to verify its influence.

For tissue, the steady state signal ($S'(\infty)$) was modeled assuming a certain constant $T_1$ and $T_2^*$: 1.2 s and 0.08 s, respectively, and setting $n$ equal to infinity in Equation (4.1). Finally, a linear combination of the AIF-signal and the tissue-signal was applied to include PVE into the simulations:

$$S_P(f,n) = (1-f)\cdot S(n) + f \cdot S'(\infty), \tag{4.14}$$

with PVE fraction $f$. Thus, our partial volume model mixes a constant background signal $S'(\infty)$ into the (foreground) AIF signal. In the appendix it is shown that the AIF signal under the influence of inflow (i.e. varying n) can be rewritten and

approximated to obtain a similar representation. As a consequence, flow has a highly comparable impact on the time concentration curve as PVE does.

White Gaussian noise was added to the resulting signal intensity curves to achieve a signal-to-noise ratio (SNR) equal to 40 decibels, i.e. the same as the SNR of the baseline signals measured in the ICA in our clinical data. Finally, the simulated signal-intensity curves were transformed into signal ratio curves $D_{\text{simu}}(t)$ by normalizing with the averaged baseline signal (before contrast agent arrival).

### 4.3.2. VALIDATION



First, simulations were run with only inflow effects incorporated: the PVE fraction ($f$) in Equation (4.14) was set to 0, and $n \in \{40, 60, 80, 100, 120, 140\}$. For each $n$, ten thousand simulations were performed with different noise realizations yielding signal ratio curves $D_{\text{simu}}(t)$. The correction algorithm was applied to each simulated signal curve to estimate the perceived pulse number which was then used to reconstruct the AIF concentration curve (Section 4.2.4). Finally, the reconstructed AIF was supersampled 20 times to 0.1 seconds temporal resolution using piecewise cubic interpolation [35], from which the peak value, full width at half maximum (FWHM) and AUC were computed; these values were compared with the ground truth values calculated from the simulated AIF (through the same interpolation procedure).

Then, partial voluming was included by increasing the PVE fraction ($f$) from 10% up to 50% for different $n$ (see above); again ten thousand noise realizations with SNR equal to 40 decibels were obtained for each setting. Subsequently, the correction algorithm was applied. To show the interaction between the correction for inflow and PVE, we both employed the true simulated pulse number (without PVE correction) and the estimated perceived pulse number to reconstruct the AIFs. Furthermore, the peak value and FWHM of both the uncorrected as well as the corrected AIFs were compared with the ground truth values.

### 4.3.3. CLINICAL DATA ACQUISITION

#### PATIENT COHORT

Data in this study were acquired as part of an associated clinical study in Netherlands: the Radiotherapy in Isocitrate dehydrogenase (IDH) mutated Glioma: Evaluation of Late outcomes (RIGEL) study (trial identifier: NCT04304300). The first ten patients who had histologically confirmed, IDH mutated glioma (WHO grade 2 or 3) and of whom the relevant imaging data were available were included in this sub-study. Informed consent was obtained from all subjects. Postoperative radiation therapy and chemotherapy were given to every patient after surgical tumor resection. MRI was performed before and approximately 4 months after radiation therapy. From three patients DCE images were obtained before and after radiation therapy, from two patients scans were only made post-treatment, and from five patients only pre-treatment data were included.

#### IMAGING AND INJECTION PROTOCOL

Imaging was performed on a 3T MRI system (Signa Premier, GE Healthcare, Waukesha, WI, USA) using a 48-channel head coil in the Erasmus MC (Rotterdam, Netherlands).

DCE images were acquired using a differential subsampling with cartesian ordering sequence [36] with TR/TE: 2.7/0.9 ms, flip angle: 14°; FOV: 220 × 220 × 144 $mm^3$; matrix size: 128 × 128, 72 slices; in-plane resolution: 1.7 mm × 1.7 mm; reconstructed resolution: 0.9 mm x 0.9 mm; slice thickness: 2 mm, temporal resolution: 2 s, to obtain 183 image volumes in total. The entire DCE sequence took 6 minutes and 6 seconds. Some other sequences were also applied for clinical purposes, but these are not relevant for this paper.

In each patient, 7.5 ml of Gadobutrol (Gadovist®, Bayer, Germany), corresponding to a standard dose for a 75 kg patient were automatically injected by a power injector. The contrast agent injections were started 20 seconds after start of the DCE imaging to allow acquiring sufficient averages of the contrast-free baseline signal.



#### PRE-PROCESSING

All image processing were done with in-house created scripts in Matlab (version R2021b; MathWorks, Inc., Natick, Massachusetts, United States). Head motion between the dynamic scans was visually checked by monitoring the three cross-sectional lines of the central coronal, sagittal and axial slices across time. Slight misalignment of the boundaries was observed in three cases; this was corrected by performing 3D rigid registration of the entire series to the first volume. We did not apply registration in the case without observed movement to avoid introducing interpolation errors.

### 4.3.4. AIF MEASUREMENT

#### REGION OF INTEREST SELECTION

In all patients of this study, regions in an artery were selected in the hemisphere contralateral to the tumor, to avoid any possible effects of the tumor on the AIF measurement. These regions-of-interest (ROIs) were manually delineated on a DCE volume after bolus arrival in which the arteries could be easily identified. Specifically, ROIs were drawn in the internal carotid artery (ICA) and segments of middle cerebral artery (MCA). Sampling of the AIF signals was performed before registration to the $T_1$ map to avoid additional blurring.

#### ARTIFICIALLY INCREASED PVE

To test whether the inflow correction method can also correct for PVE, one voxel of interest was placed at the center of the ICA in a proximal imaging plane for each patient. Then, the signal-time curve of this voxel was averaged with those of surrounding voxels by applying an increasing kernel size from 3-by-3 to 9-by-9

voxels applied within plane. This was done to mimic increasing PVE at a fixed inflow effect.

### DOWNSTREAM SAMPLING THE AIF

The inflow effect is expected to diminish gradually from ICA to MCA due to increased exposure to excitation pulses. However, simultaneously it can be expected that PVE becomes more severe, since the diameter of the arteries become smaller. To test the sensitivity of our correction algorithm to these mixed effects, we measured the AIF in the ICA ($AIF_{ICA}$), the M1 ($AIF_{M1}$) and the M2 ($AIF_{M2}$) segments of the MCA. Accordingly, groups of 9 voxels were selected in the ICA and the M1 and M2 segments of the MCA in each patient, for measuring the AIF from upstream to downstream in the same arterial territory. Subsequently, the signal over the ROI was averaged for each dynamic to obtain a signal-time intensity curve reflecting the AIF.



### CONCENTRATION ESTIMATION

Signal ratio curves $D_{meas}(t)$ were first derived by dividing the time-signal intensity curves from each region by the mean of the first ten baseline signals. Then, the correction algorithm described in Section 4.2.4 was applied to the AIF signal ratio curves, estimating the perceived pulse number. Finally, we used the estimated pulse number to reconstruct the AIFs.

### AIF ALTERNATIVE

Conforming to an often applied practical approach, we also measured the VOF from the SSS ($VOF_{SSS}$). As with the AIFs, ROIs consisting of 9 voxels inside the SSS were manually delineated in an axial slice after which mean signal-time intensity curves were obtained. Subsequently, contrast concentration curves were calculated as described in Section 4.2.1, asserting that the spins were in steady state and assuming $T_{10}$= 1.8 s for blood.

### EVALUATION

For assessing the influence of artificially increasing PVE, the estimated pulse number from each kernel was compared with the estimated pulse number of the central voxel. Also, the root mean square error was calculated from the difference between the corrected AIF and the one from the central voxel (serving as the gold standard reference) and further normalized with the peak value of the central voxel to deliver the normalized root mean square error (NRMSE).

The $AIF_{ICA}$, $AIF_{M1}$, $AIF_{M2}$ and $VOF_{SSS}$ were compared based on the peak values, the FWHMs and the products of the peak value and FWHM (i.e. the peak FWHM product, PFP), which is related to area under first bolus peak. Differences were statistically assessed using the Wilcoxon test. P-values smaller than 0.05 were considered as statistical significant.

# 4.4. RESULTS

## 4.4.1. SIMULATION

Figure 4.1 shows the employed Orton's AIF model as calculated from population-averaged parameters (a), MR signal ratio curves including only inflow effects (b), and the signal ratio curves affected both by inflow effects and PVE (c). Notice that no noise was added, so that the graphs show only the effects of inflow and PVE.

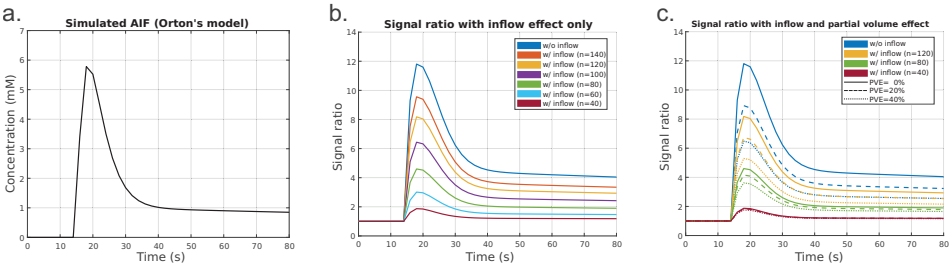


Figure 4.1: Simulated AIF concentration curve from Orton's model (a), signal ratio curves from simulated AIF concentration curves with inflow effect only (b) and likewise with partial voluming added (c). Notice that PVE led to similar underestimation of the AIF curves as inflow.

## 4.4.2. VALIDATION

In the following experiments, Gaussian noise was added before deriving signal ratio curves. Error percentages of the estimated pulse number, reconstructed peak value, FWHM and AUC from simulated data that only included inflow effects, are shown in Figure 4.2. A bias of a few percents (less than 3%) was observed in all the plotted parameters. The variance increased when stronger inflow effects, i.e. lower n, were simulated. Figure S4.1 collates the same estimations while $T_2^*$ effects were not included in the simulations. No bias has been detected in this simulation.

As PVEs were introduced, the estimated pulse numbers gradually decreased when the partial volume fraction increased (Figure 4.3a). Simultaneously, only little influence on peak values and FWHMs was observed on the corrected AIFs, showing that the inflow correction method also compensated most of the PVE (Figure 4.3b,c). This complementary correction becomes even more biased when applying the real (input) pulse number to correct the AIFs, i.e. reflecting 'perfect' correction for only the inflow effects (Figure 4.3d,e).

## 4.4.3. CORRECTION IN CLINICAL DATA

### ARTIFICIALLY INCREASED PVE

Figure 4.4 shows three representative examples of PVE compensation in different patients. Clearly, the AIFs were faithfully reconstructed even with large simulated partial voluming. A decrease in estimated pulse number with increasing

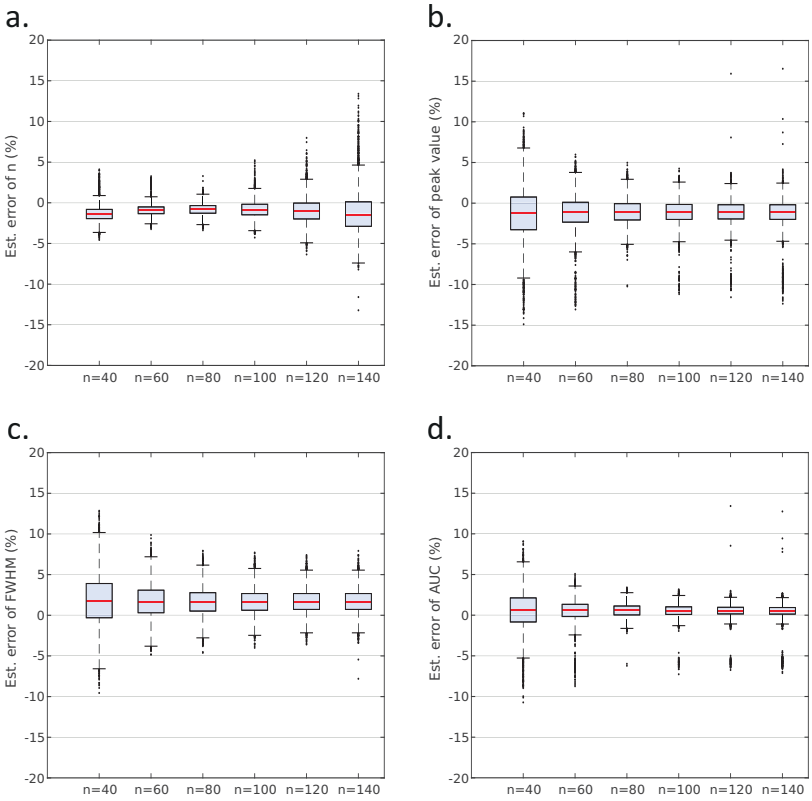


Figure 4.2: Error percentage of estimated pulse number (a), peak value (b), FWHM (c) and AUC (d) of compensated AIFs while inflow and $T_2^*$ effect is simulated.

PVE fraction was observed in every patient (Table 4.1). Furthermore, the NRMSE generally stayed small, albeit moderately higher with larger kernel sizes. Supplementary Figure S4.2 shows the detrimental effect on the signal curves and the reconstructions when a nearby vessel is include with a different enhancement time (i.e. arrival of the peak).

### AIF MEASUREMENTS UPSTREAM AND DOWNSTREAM

A box plot of estimated pulse numbers for the AIFs and the VOF is included in supplementary Figure S4.3. Unsurprisingly, the VOF received markedly more excitation pulses than the AIFs did. Figure 4.5 shows the peak values, FWHMs and PFPs of the three AIFs and the VOF for all subjects. The peak values in the $VOF_{SSS}$ were significantly lower than in the $AIF_{ICA}$ (p-value: 0.03), and in the $AIF_{M1}$ (p-value: 0.04). The peak values in the $VOF_{SSS}$ and $AIF_{M2}$ were not significantly different (p-value: 0.05). Significantly larger FWHMs were observed in the $VOF_{SSS}$ compared to the $AIF_{ICA}$ (p-value: 0.02) and the $AIF_{M1}$ (p-value: 0.03). There was

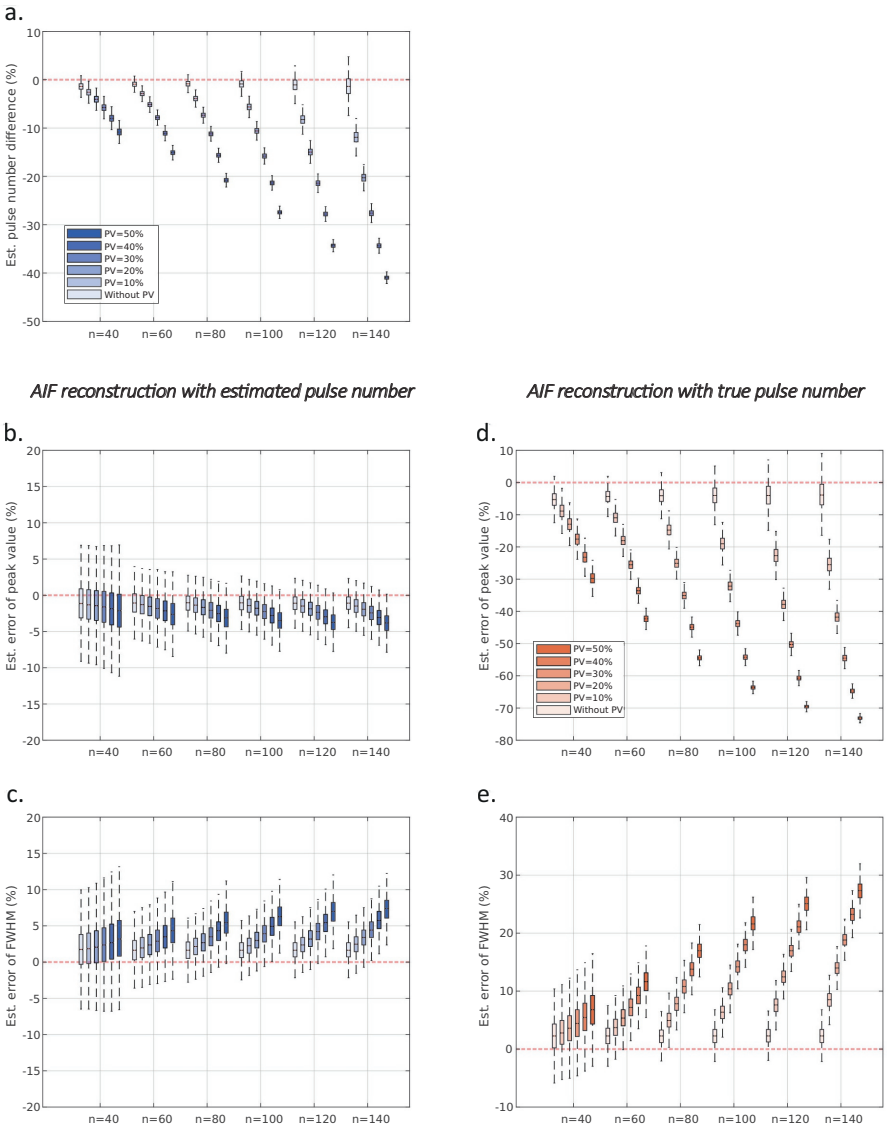


Figure 4.3: Variation in the estimated pulse number (a) when partial volume correction is included in simulated signal ratio curves; the peak value (b) and FWHM (c) of the reconstructed AIF using the estimated pulse number; error in peak value (d) and FWHMs (e) when using the true pulse number, i.e. without partial volume correction during AIF reconstruction.

no significant difference between the FWHMs from the $VOF_{SSS}$ and $AIF_{M1}$ (p-value: 0.10). Other comparisons, e.g. the PFPs, yielded no significant differences.

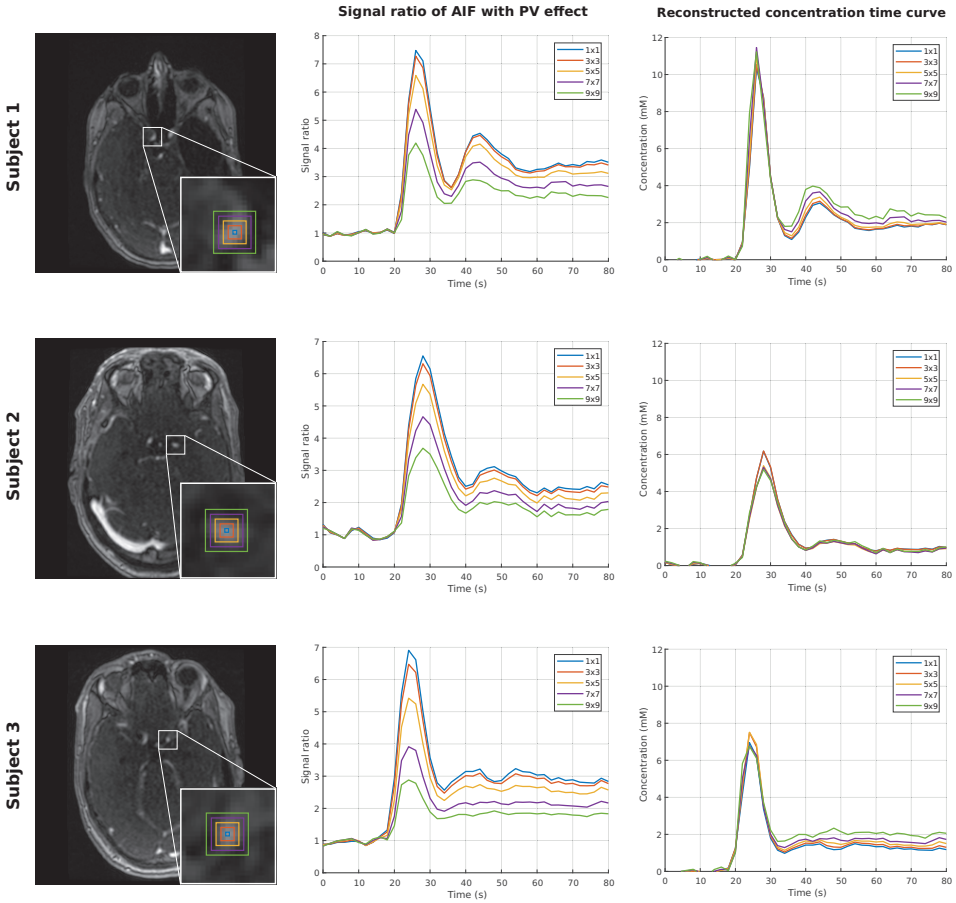


Figure 4.4: Simulation and compensation of increasing PVE in the ICA in three different subjects (top to bottom). Left column depicts a cross-section of the artery and the regions over which PVE is simulated (colored squares). Mean signal ratio curves within the kernel's footprint and reconstructed AIF concentration curves are shown in middle and right columns, respectively. Notice that only first 40 time points of the series are plotted for clarity reasons.

## 4.5. DISCUSSION

In this paper we studied the potential of a method to simultaneously correct the AIF measured in DCE MRI for PVE and inflow effects. This was inspired by the observation that PVE induces a similar shape and amplitude changes of the AIF as inflow does. In the Appendix we mathematically underpin that the two effects indeed have a similar effect on the AIF measurement, which also implies that they cannot be separated. Our results show that the correction algorithm sustains combined correction for both inflow effect and PVE.

Table 4.1: Difference in estimated pulse number ($n_d$) and normalized root mean square error (NRMSE) of reconstructed AIFs with increasing PVE (i.e. applied kernel size) in comparison to data from the central arterial voxel.

| | $n_d$ (%) | | | | NRMSE | | | |
|---|---|---|---|---|---|---|---|---|
| | **3x3** | **5x5** | **7x7** | **9x9** | **3x3** | **5x5** | **7x7** | **9x9** |
| Subject 1 | −0.7 | −5.3 | −14.2 | −26.6 | 0.008 | 0.016 | 0.032 | 0.055 |
| Subject 2 | −2.4 | −8.8 | −22.3 | −33.0 | 0.003 | 0.008 | 0.039 | 0.046 |
| Subject 3 | −6.0 | −16.2 | −32.4 | −44.1 | 0.023 | 0.038 | 0.074 | 0.098 |
| Subject 3* | −2.3 | −9.0 | −26.0 | −35.1 | 0.007 | 0.028 | 0.068 | 0.092 |
| Subject 4* | −0.6 | −1.4 | −11.2 | −22.4 | 0.004 | 0.019 | 0.036 | 0.080 |
| Subject 5 | −6.6 | −12.0 | −16.6 | −26.7 | 0.023 | 0.036 | 0.054 | 0.145 |
| Subject 6 | −2.8 | −6.7 | −21.9 | −30.7 | 0.003 | 0.021 | 0.016 | 0.023 |
| Subject 6* | 4.3 | −3.2 | −8.0 | −17.9 | 0.035 | 0.011 | 0.025 | 0.023 |
| Subject 7* | −3.1 | −10.6 | −21.2 | −30.2 | 0.004 | 0.016 | 0.033 | 0.043 |
| Subject 8 | −4.9 | −13.1 | −24.9 | −33.4 | 0.004 | 0.010 | 0.028 | 0.039 |
| Subject 8* | −0.3 | −6.5 | −16.0 | −24.5 | 0.006 | 0.012 | 0.025 | 0.034 |
| Subject 9 | −5.0 | −11.7 | −25.8 | −36.4 | 0.004 | 0.015 | 0.022 | 0.033 |
| Subject 10 | −4.7 | −13.3 | −22.5 | −32.0 | 0.007 | 0.022 | 0.029 | 0.040 |

*Patient received radiation therapy

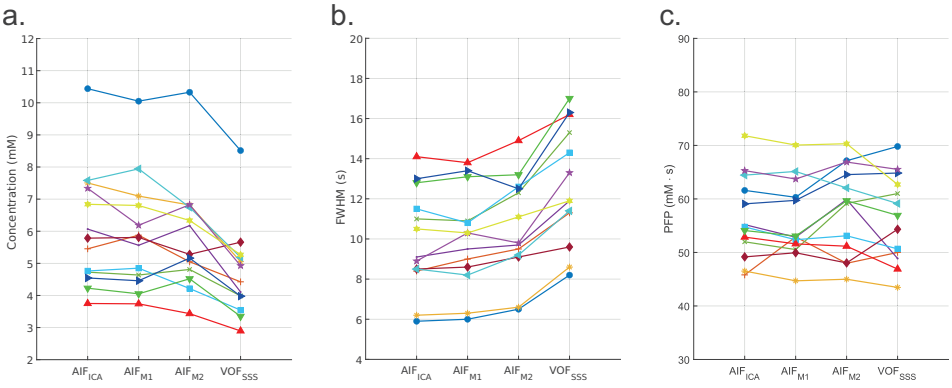


Figure 4.5: Peak values (a), FWHMs (b) and PFPs (c) from $AIF_{ICA}$, $AIF_{M1}$, $AIF_{M2}$ (applying inflow and partial voluming correction), and $VOF_{SSS}$ (without any correction). Colors denote independent measurements. The $VOF_{SSS}$ had significantly lower peak value and higher FWHM than the $AIF_{ICA}$ and $AIF_{M1}$.

While inflow correction has been widely studied, PVE on AIF measurement remains a challenging issue. Practically, the temporal resolution is often maximized for obtaining high quality AIFs and high accuracy and precision of permeability estimates [37]. While doing so, the imaging resolution may be sacrificed in order to accelerate the image acquisition, inherently resulting in mixing the arterial signal

with tissue signals. A recent study emphasizes the importance of PVE correction for enhanced reproducibility of pharmacokinetic coefficients derived from DCE MRI [20]. To our knowledge, ours is the first study investigating the feasibility of correcting inflow effect and PVE simultaneously. To comprehensively verify the potential of the correction method, we performed realistic simulations, and also checked the method in an array of AIF measurements in clinical datasets. The studied method accurately reconstructed the AIF with marginal bias except for some unrealistic cases. This shows that the correction method has great potential for use in clinical DCE analysis.

When simulating only inflow effects, the method yielded a small bias (less than 3%) in the peak value and the width of the AIF (Figure 4.2 b, c), irrespective of the extent of the inflow effect. The remaining bias results from $T_2^*$ effects that *were* included in simulated signals. Indeed, Figure S4.1 in the supplementary file shows the outcomes on simulated signals generated without any $T_2^*$ effects which do not exhibit a bias. At the same time the interquartile range of the peak value and the AIF width increased for more severe inflow effects. This reflects that with strong inflow (small $n$) a small error in the number of estimated pulses has a relatively large effect on the AIF parameters. Intuitively, this makes sense since closer to steady state (i.e. with small inflow) variation in the number of pulses affects the signal less, as such resulting in a more stable estimation of the AIF. At the same time a small number of pulses suppresses the contrast of the signal ratio curves as can be observed in Figure 4.1b. This could also hinder the estimation of the number of pulses, and affect the peak height and FWHM estimations.

When including PVE but applying the correct number of pulses (i.e. perfect correction of only the inflow effects), the peak value and AIF width became significantly affected by PVE, especially when approaching steady state (see Figure 4.3d,e). This shows the dilemma in clinical use of DCE imaging, in which an AIF is preferably derived from arteries as close as possible to the tissue of interest, which would minimize inflow effects, but at the same time concerns arteries affected by PVE due to their small size. Taking both effects into account, the proposed method yielded only a small bias both in the peak value and FWHM of the reconstructed AIF concentration curves (c.f. Figure 4.3b,c). This remaining (mild) bias might be due to unaccounted differences between partial volume and inflow effects. Especially the stability of the estimation (i.e. the constantly small width and bias of the distributions), independent of PVE/degree of inflow gives the technique high potential for clinical application.

Our experiments about mimicking PVE by averaging the signal over larger numbers of voxels surrounding a central arterial voxel confirm the robustness of the proposed approach as larger PVE hardly affected the outcome. Robustness against such varying partial voluming is useful as it can be difficult to accurately delineate a region in an artery in clinical DCE data. Simultaneously, however, it is important to ascertain that surrounding tissue exhibits the same enhancement timing as the studied artery. In particular, we observed that as the averaging region in this experiment started to overlap with a region exhibiting a later

enhancement, the outcome became increasingly biased. The combination of such distinct enhancement profiles gave a distorted bolus peak profile, which resulted in erroneous correction. Thus, one should avoid applying our correction to AIF measurements in neighbourhoods with different vessels as they may show varied enhancement timing, yielding a wrong outcome.

Measuring the AIF from the ICA is associated with the less PVE compared with the MCA, but there are stronger inflow effects. Practically, the ICA may not always be covered by the image volume due to imaging limitations, e.g. restrictions in scan time. In that case, the MCA could be an alternative, which inherently goes at the expense of larger PVE. We studied both AIF sources to demonstrate the capability of our method with different combinations of inflow effect and PVE. We did not find a significant difference in peak value and FWHM between the measurements in the ICA and MCA (for both the M1 and M2 segments). Yet, a small decreasing trend in the AIF peak and an increasing trend in the FWHM from M1 to M2 segment of the MCA seems visible in our data (Figure 4.5). Essentially, this corresponds with our simulation results in which mild inflow effects combined with larger PVE caused increasing (albeit marginal) bias (Figure 4.3). Accordingly, we propose to practically apply the correction method to an AIF from the most upstream fragment of the covered vascular system as that should give the most reliable outcome.



VOF measurement in the SSS has also been considered as a useful alternative to arterial measurement due to limited inflow and PVE effects [38]. Indeed, by applying the correction algorithm to the measured signal ratio curve from the SSS, a large number of excitation pulses was estimated (Figure S4.3). This signified that the spins were close to steady state. However, significantly lower peak values and increased FWHMs were found when comparing the VOF from the SSS with the AIF in the ICA or M1 segment of the MCA. This showed that the shape of the VOF was not in agreement with the AIF. We attribute this difference to increased dispersion of the contrast agent, limiting the usefulness of the SSS measurement as input of a DCE analysis. This corresponds with the results from Cramer et al. [20], which reported that the VOF measured in the SSS had a lower peak value than AIFs with PVE corrections; also it was found that the VOF yielded low reproducibility, even though the VOF is theoretically less prone to inflow artifact and PVE.

There are several limitations to our study. First, we didn't have a real ground truth AIF. Clearly, such true AIF can only be measured from blood sampling for which we did not have ethical approval. Furthermore, the method assumed a fixed area under first bolus peak to estimate the underestimation of inflow and PVE. This might in reality vary across subjects and/or vessel of interest. However, it was previously reported in Parker et al. [11] that the relative standard error in this parameter is only 5.4%. In addition, we assumed that local extravasation of contrast agent can be neglected. The extravasation might affect the ROI-signal in which the AIF is determined when the leakage is substantial or for large degrees of PVE. As such the ROI for the AIF should not be selected near tumor tissue, but for example on the contralateral side of the brain. Finally, we did not study the effect

of the AIF on the estimation of pharmacokinetic model parameters like the $K^{trans}$ in tumor regions, since we did not observe any clear leakage of contrast in the $T_1$ weighted images in any of our patients (comparing the signal in the baseline DCE images with those after contrast injection).

## 4.6. CONCLUSION

This study demonstrated the potential of a method to simultaneously correct the AIF for inflow effect and PVE. The method relies on interpreting larger PVE as increasing inflow effect. Although the SSS is less susceptible to the referred effects, it was found not to be an appropriate source for the input function as it showed increased dispersion of the GBCA. As a result, this would lead to overestimation of vascular permeability coefficients compared to the AIFs. Instead, applying the studied approach of deriving AIFs from arteries with proper correction of inflow and PVE could be a better strategy for DCE analysis.



## 4.7. APPENDIX

In this appendix, we aim to mathematically show that the PVE has a similar effect as the inflow effect on DCE-AIF measurement.

Our derivation starts with writing out the expression for the spoiled gradient echo signal as a function of the excitation pulse number n, by combining Equations (4.1-4.3):

$$S(n) = \sin\alpha \cdot M_0 \cdot \left( \left( 1 - \frac{1 - e^{\frac{-TR}{T_1}}}{1 - \cos\alpha \cdot e^{\frac{-TR}{T_1}}} \right) \cdot \left( \cos(\alpha) \cdot e^{\frac{-TR}{T_1}} \right)^n + \frac{1 - e^{\frac{-TR}{T_1}}}{1 - \cos\alpha \cdot e^{\frac{-TR}{T_1}}} \right) \cdot e^{\frac{-TE}{T_2^*}}. \tag{A.1}$$

Observe that in this expression the term $M_0 \cdot (1 - e^{\frac{-TR}{T_1}})/(1 - \cos\alpha \cdot e^{\frac{-TR}{T_1}})$ is equal to the steady state magnetization given in Equation (4.4). Furthermore, the $T_1$ and $T_2^*$ parameters are modulated by the contrast agent concentration as defined in Equations (4.5) and (4.6), respectively. Taking these aspects into account, Equation (A.1) can be rewritten as:

$$S(C,n) = \sin\alpha \cdot \left( \left( M_0 - M_z(C,\infty) \right) \cdot (\cos\alpha \cdot e^{\frac{-TR}{T_{1(C)}}})^n + M_z(C,\infty) \right) \cdot e^{\frac{-TE}{T_{2(C)}^*}}, \tag{A.2}$$

In steady state, i.e. with very large n, this expression simplifies to $S(C,\infty) = \sin\alpha \cdot M_z(C,\infty) \cdot e^{\frac{-TE}{T_{2(C)}^*}}$. Based on this, by reshuffling the terms the former

equation yields:

$$\begin{aligned} S(C,n) = & M_0 \cdot \sin\alpha \cdot (\cos\alpha \cdot e^{\frac{-TR}{T_1(C)}})^n \cdot e^{\frac{-TE}{T_2^*(C)}} \\ & + (1 - (\cos\alpha \cdot e^{\frac{-TR}{T_1(C)}})^n) \cdot S(C,\infty). \end{aligned} \tag{A.3}$$

In the $T_1$-weighted DCE sequence, the echo time is usually small ($\approx$ 1 ms), so that $e^{\frac{-TE}{T_2^*(C)}} \approx 1$. Additionally, $(\cos\alpha \cdot e^{\frac{-TR}{T_1(C)}})^n$ can be conceived as a weighting factor w(C,n) that ranges from 0 (for large n) to 1 (for small n). As a result the above equation can be approximated by

$$S(C,n) \approx w(C,n) \cdot M_0 \cdot \sin\alpha + \big(1 - w(C,n)\big) \cdot S(C,\infty). \tag{A.4}$$

In this last equation, $M_0 \cdot \sin(\alpha)$ is a constant term Thus, the AIF signal ($S(C,n)$) indeed approximates the steady state AIF with large n, while a constant signal is increasingly mixed in with decreasing n. This equation is compatible with Equation (4.14). As such, flow can be considered as a PVE in which a fraction w(C,n) of the background signal $M_0 \cdot \sin(\alpha)$ is combined with the foreground AIF.

## 4.8. SUPPLEMENTARY MATERIALS

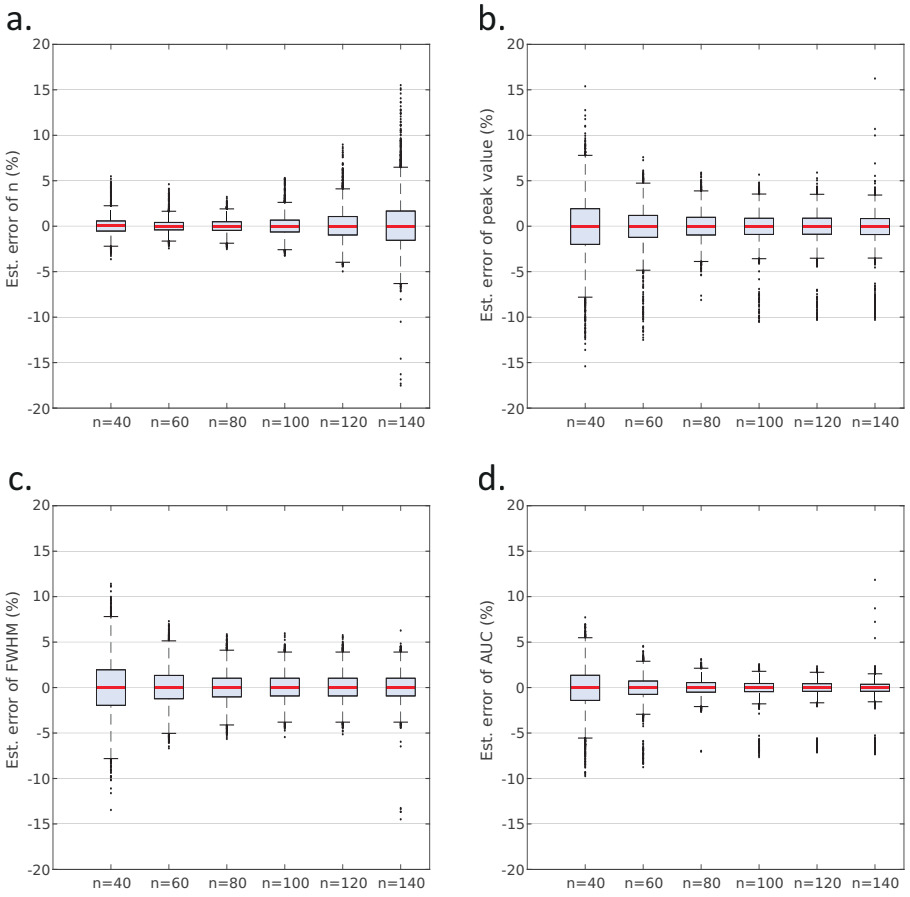


Figure S4.1: Error percentage of estimated pulse number (a), peak value (b), FWHM (c) and AUC (d) of compensated AIFs while inflow correction without simulating $T_2^*$ effects.

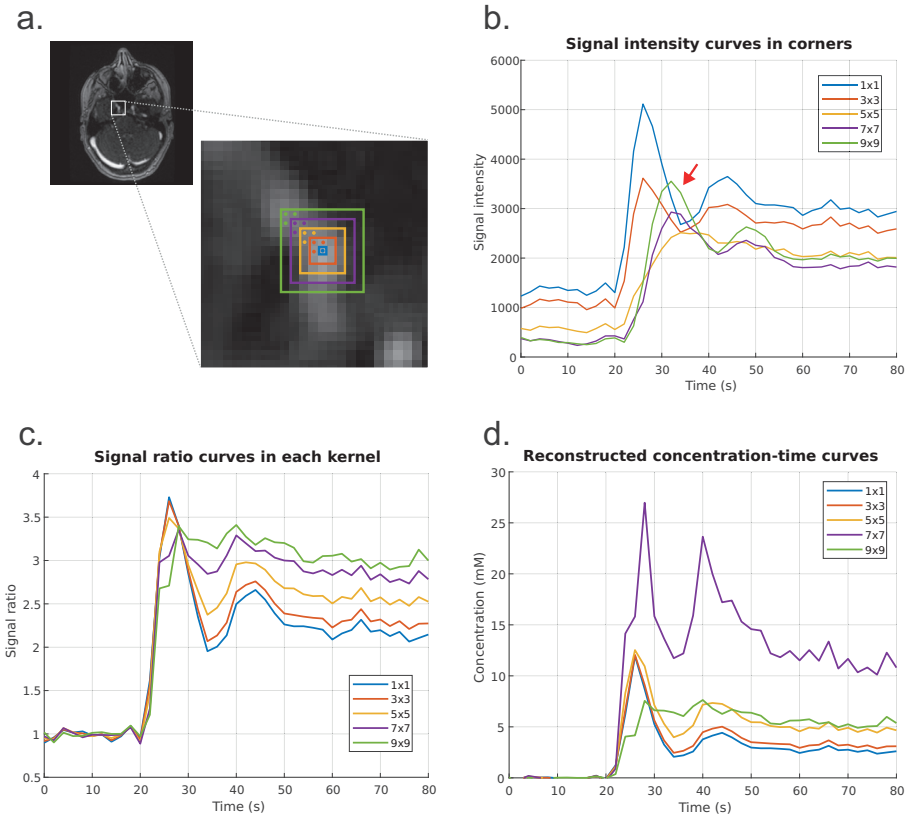


Figure S4.2: This figure demonstrates that averaging over surrounding voxels with delayed enhancement makes the inflow and PVE correction erroneous. In particular, the central arterial voxel and the corners of the kernels (as indicated by the points in the image) were studied (a). Mean signal-intensity curves in corners of large kernels showed apparently delayed enhancement (red arrow in b). The signal ratio curves in large kernels were thereby distorted by averaging over these voxels (c), leading to errors in the reconstructed AIF concentration-time curves (d).

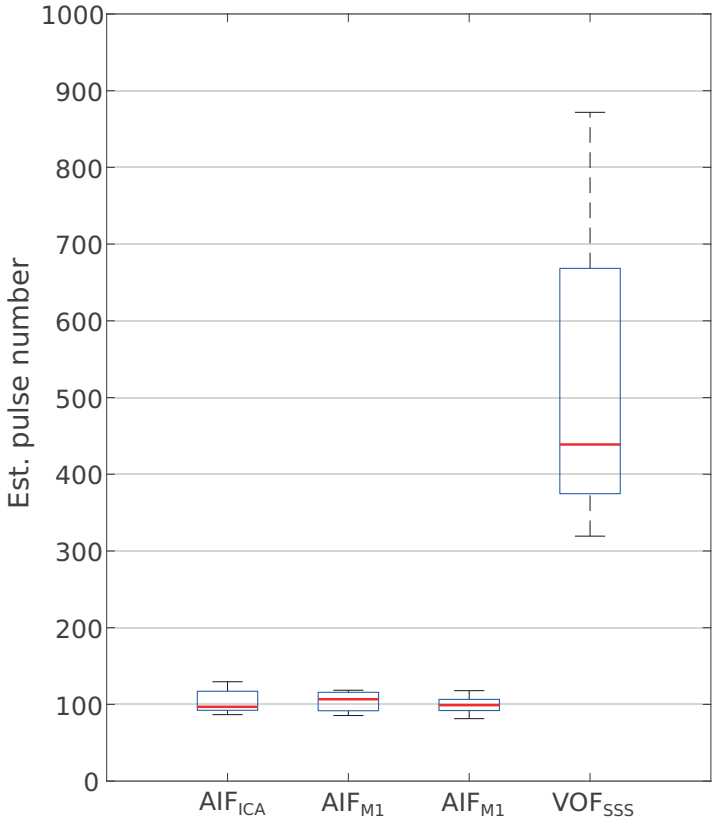


Figure S4.3: Boxplot of the estimated pulse number in the AIFs and the VOF in all subjects. The AIFs showed relatively similar estimates while there is increasing PVE accompanied by decreasing inflow effect. In contrast, the estimations for the VOF exhibit large interquartile range. This is related to the larger estimated pulse number, making that the magnetization is approximating the steady state. In that case a deviation in pulse number has little effect on the AIF shape, which hinders the pulse number estimation.

# REFERENCES


[1] T. Yankeelov and J. Gore. "Dynamic Contrast Enhanced Magnetic Resonance Imaging in Oncology:Theory, Data Acquisition,Analysis, and Examples". In: *Current Medical Imaging Reviews* 3.2 (May 2007), pp. 91–107. ISSN: 15734056. DOI: 10.2174/157340507780619179.

[2] N. Tuncbilek, H. M. Karakas, and S. Altaner. "Dynamic MRI in indirect estimation of microvessel density, histologic grade, and prognosis in colorectal adenocarcinomas". In: *Abdominal Imaging* 29.2 (Mar. 2004), pp. 166–172. ISSN: 0942-8925. DOI: 10.1007/s00261-003-0090-2.

[3] N. Tuncbilek, H. M. Karakas, and O. O. Okten. "Dynamic contrast enhanced MRI in the differential diagnosis of soft tissue tumors". In: *European Journal of Radiology* 53.3 (Mar. 2005), pp. 500–505. ISSN: 0720048X. DOI: 10.1016/j.ejrad.2004.04.012.

[4] M. Medved *et al.* "Semiquantitative analysis of dynamic contrast enhanced MRI in cancer patients: Variability and changes in tumor tissue over time". In: *Journal of Magnetic Resonance Imaging* 20.1 (July 2004), pp. 122–128. ISSN: 1053-1807. DOI: 10.1002/jmri.20061.

[5] V. A. Arasu *et al.* "Can Signal Enhancement Ratio (SER) Reduce the Number of Recommended Biopsies without Affecting Cancer Yield in Occult MRI-detected Lesions?" In: *Academic Radiology* 18.6 (June 2011), pp. 716–721. ISSN: 10766332. DOI: 10.1016/j.acra.2011.02.008.

[6] C. Lavini *et al.* "Pixel-by-pixel analysis of DCE MRI curve patterns and an illustration of its application to the imaging of the musculoskeletal system". In: *Magnetic Resonance Imaging* 25.5 (June 2007), pp. 604–612. ISSN: 0730725X. DOI: 10.1016/j.mri.2006.10.021.

[7] F. Khalifa *et al.* "Models and methods for analyzing DCE-MRI: A review". In: *Medical Physics* 41.12 (Nov. 2014), p. 124301. ISSN: 00942405. DOI: 10.1118/1.4898202.

[8] P. S. Tofts *et al.* "Estimating kinetic parameters from dynamic contrast-enhanced t1-weighted MRI of a diffusable tracer: Standardized quantities and symbols". In: *Journal of Magnetic Resonance Imaging* 10.3 (Sept. 1999), pp. 223–232. ISSN: 1053-1807. DOI: 10.1002/(SICI)1522-2586(199909)10:3<223::AID-JMRI2>3.0.CO;2-S.

[9] M. Essig *et al.* "Perfusion MRI: The Five Most Frequently Asked Technical Questions". In: *American Journal of Roentgenology* 200.1 (Jan. 2013), pp. 24–34. ISSN: 0361-803X. DOI: 10.2214/AJR.12.9543.

[10] S. Okuchi *et al.* "Diagnostic accuracy of dynamic contrast-enhanced perfusion MRI in stratifying gliomas: A systematic review and meta-analysis". In: *Cancer Medicine* 8.12 (Sept. 2019), pp. 5564–5573. ISSN: 2045-7634. DOI: 10.1002/cam4.2369.

[11] G. J. M. Parker *et al.* "Experimentally-derived functional form for a population-averaged high-temporal-resolution arterial input function for dynamic contrast-enhanced MRI." In: *Magnetic resonance in medicine* 56.5 (Nov. 2006), pp. 993–1000. ISSN: 0740-3194. DOI: 10.1002/mrm.21066.

[12] M. Rijpkema *et al.* "Method for quantitative mapping of dynamic MRI contrast agent uptake in human tumors". In: *Journal of Magnetic Resonance Imaging* 14.4 (Oct. 2001), pp. 457–463. ISSN: 1053-1807. DOI: 10.1002/jmri.1207.

[13] E. Ashton *et al.* "Scan-rescan variability in perfusion assessment of tumors in MRI using both model and data-derived arterial input functions". In: *Journal of Magnetic Resonance Imaging* 28.3 (Sept. 2008), pp. 791–796. ISSN: 10531807. DOI: 10.1002/jmri.21472.

[14] F. Calamante. "Bolus dispersion issues related to the quantification of perfusion MRI data". In: *Journal of Magnetic Resonance Imaging* 22.6 (Dec. 2005), pp. 718–722. ISSN: 1053-1807. DOI: 10.1002/jmri.20454.

[15] M. J. P. Van Osch *et al.* "Correcting partial volume artifacts of the arterial input function in quantitative cerebral perfusion MRI". In: *Magnetic Resonance in Medicine* 45.3 (Mar. 2001), pp. 477–485. ISSN: 0740-3194. DOI: 10.1002/1522-2594(200103)45:3<477::AID-MRM1063>3.0.CO;2-4.

[16] A. E. Hansen *et al.* "Partial volume effect (PVE) on the arterial input function (AIF) in T1-weighted perfusion imaging and limitations of the multiplicative rescaling approach". In: *Magnetic Resonance in Medicine* 62.4 (Oct. 2009), pp. 1055–1059. ISSN: 07403194. DOI: 10.1002/mrm.22098.

[17] J. U. Harrer *et al.* "Comparative study of methods for determining vascular permeability and blood volume in human gliomas". In: *Journal of Magnetic Resonance Imaging* 20.5 (Nov. 2004), pp. 748–757. ISSN: 10531807. DOI: 10.1002/jmri.20182.

[18] V. C. Keil *et al.* "Effects of arterial input function selection on kinetic parameters in brain dynamic contrast-enhanced MRI". In: *Magnetic Resonance Imaging* 40 (July 2017), pp. 83–90. ISSN: 0730725X. DOI: 10.1016/j.mri.2017.04.006.

[19] M. J. Thrippleton *et al.* "Quantifying blood-brain barrier leakage in small vessel disease: Review and consensus recommendations". In: *Alzheimer's & Dementia* 15.6 (June 2019), pp. 840–858. ISSN: 1552-5260. DOI: 10.1016/j.jalz.2019.01.013.

[20] S. P. Cramer *et al.* "Reproducibility and Optimal Arterial Input Function Selection in Dynamic Contrast-Enhanced Perfusion MRI in the Healthy Brain". In: *Journal of Magnetic Resonance Imaging* (Aug. 2022). ISSN: 1053-1807. DOI: 10.1002/jmri.28380.

[21] C. Roberts *et al.* "The effect of blood inflow and B(1)-field inhomogeneity on measurement of the arterial input function in axial 3D spoiled gradient echo dynamic contrast-enhanced MRI." In: *Magnetic resonance in medicine* 65.1 (Jan. 2011), pp. 108–19. ISSN: 1522-2594. DOI: 10.1002/mrm.22593.

[22] M. K. Ivancevic *et al.* "Inflow effect correction in fast gradient-echo perfusion imaging". In: *Magnetic Resonance in Medicine* 50.5 (Nov. 2003), pp. 885–891. ISSN: 07403194. DOI: 10.1002/mrm.10633.

[23] A. Garpebring *et al.* "Effects of inflow and radiofrequency spoiling on the arterial input function in dynamic contrast-enhanced MRI: a combined phantom and simulation study." In: *Magnetic resonance in medicine* 65.6 (June 2011), pp. 1670–9. ISSN: 1522-2594. DOI: 10.1002/mrm.22760.

[24] A. Garpebring *et al.* "Phase-based arterial input functions in humans applied to dynamic contrast-enhanced MRI: potential usefulness and limitations". In: *Magnetic Resonance Materials in Physics, Biology and Medicine* 24.4 (Aug. 2011), pp. 233–245. ISSN: 0968-5243. DOI: 10.1007/s10334-011-0257-8.

[25] R. Materne *et al.* "Assessment of hepatic perfusion parameters with dynamic MRI". In: *Magnetic Resonance in Medicine* 47.1 (Jan. 2002), pp. 135–142. ISSN: 0740-3194. DOI: 10.1002/mrm.10045.

[26] J. Ning *et al.* "Vascular input function correction of inflow enhancement for improved pharmacokinetic modeling of liver DCE-MRI". In: *Magnetic Resonance in Medicine* 79.6 (June 2018), pp. 3093–3102. ISSN: 07403194. DOI: 10.1002/mrm.26988.

[27] J. J. N. Van Schie *et al.* "Estimating the arterial input function from dynamic contrast-enhanced MRI data with compensation for flow enhancement (I): Theory, method, and phantom experiments". In: *Journal of Magnetic Resonance Imaging* 47.5 (May 2018), pp. 1190–1196. ISSN: 10531807. DOI: 10.1002/jmri.25906.

[28] M. R. Orton *et al.* "Computationally efficient vascular input function models for quantitative kinetic modelling using DCE-MRI." In: *Physics in medicine and biology* 53.5 (Mar. 2008), pp. 1225–39. ISSN: 0031-9155. DOI: 10.1088/0031-9155/53/5/005.

[29] G. de Simone *et al.* "Stroke Volume and Cardiac Output in Normotensive Children and Adults". In: *Circulation* 95.7 (Apr. 1997), pp. 1837–1843. ISSN: 0009-7322. DOI: 10.1161/01.CIR.95.7.1837.

[30] X. Zhang *et al.* "In vivo blood T1 measurements at 1.5 T, 3 T, and 7 T". In: *Magnetic Resonance in Medicine* 70.4 (Oct. 2013), pp. 1082–1086. ISSN: 07403194. DOI: 10.1002/mrm.24550.

[31] A. Petrovic *et al.* "Time related changes of T1, T2, and T2* of human blood in vitro". In: *Forensic Science International* 262 (May 2016), pp. 11–17. ISSN: 03790738. DOI: 10.1016/j.forsciint.2016.02.032.

[32] Y. Shen *et al.* "T1 relaxivities of gadolinium-based magnetic resonance contrast agents in human whole blood at 1.5, 3, and 7 T." In: *Investigative radiology* 50.5 (May 2015), pp. 330–8. ISSN: 1536-0210. DOI: 10.1097/RLI.0000000000000132.

[33] F. Calamante, E.-j. P. A. Vonken, and M. J. P. van Osch. "Contrast agent concentration measurements affecting quantification of bolus-tracking perfusion MRI." In: *Magnetic resonance in medicine* 58.3 (Sept. 2007), pp. 544–53. ISSN: 0740-3194. DOI: 10.1002/mrm.21362.

[34] M. Pedersen *et al.* "Quantitative cerebral perfusion using the PRESTO acquisition scheme". In: *Journal of Magnetic Resonance Imaging* 20.6 (Dec. 2004), pp. 930–940. ISSN: 10531807. DOI: 10.1002/jmri.20206.

[35] F. N. Fritsch and R. E. Carlson. "Monotone Piecewise Cubic Interpolation". In: *SIAM Journal on Numerical Analysis* 17.2 (Apr. 1980), pp. 238–246. ISSN: 0036-1429. DOI: 10.1137/0717021.

[36] M. Saranathan *et al.* "DIfferential subsampling with cartesian ordering (DISCO): A high spatio-temporal resolution dixon imaging sequence for multiphasic contrast enhanced abdominal imaging". In: *Journal of Magnetic Resonance Imaging* 35.6 (June 2012), pp. 1484–1492. ISSN: 10531807. DOI: 10.1002/jmri.23602.

[37] W. H. Lim *et al.* “Assessing the reproducibility of high temporal and spatial resolution dynamic contrast-enhanced magnetic resonance imaging in patients with gliomas”. In: *Scientific Reports* 11.1 (Dec. 2021), p. 23217. ISSN: 2045-2322. DOI: 10.1038/s41598-021-02450-5.

[38] J. R. Ewing *et al.* “Patlak plots of Gd-DTPA MRI data yield blood–brain transfer constants concordant with those of 14-C-sucrose in areas of blood–brain opening”. In: *Magnetic Resonance in Medicine* 50.2 (Aug. 2003), pp. 283–292. ISSN: 0740-3194. DOI: 10.1002/mrm.10524.

# 5

# LEAKAGE CORRECTION IN DYNAMIC SUSCEPTIBILITY CONTRAST MRI: A COMBINED ANALYSIS WITH DYNAMIC CONTRAST ENHANCED IMAGING

This chapter has been submitted to *Magnetic Resonance in Medicine* as:
**Tseng C-H**, van Osch MJP, Pruis IJ, et al. Leakage correction in dynamic susceptibility contrast MRI: a combined analysis with dynamic contrast enhanced imaging.

## ABSTRACT

Gadolinium-based contrast agent (GBCA) leakage in dynamic susceptibility contrast (DSC) MRI can significantly affect cerebral blood volume (CBV) estimation in brain tumors. Conventional leakage correction methods, such as the Boxerman–Schmainda–Weisskoff (BSW) approach, have limitations. In this proof of concept study, we aimed to develop a novel leakage correction method for DSC MRI that utilizes vascular parameters derived from dynamic contrast enhanced (DCE) MRI to estimate and correct for GBCA leakage.

Simulations were performed to evaluate the accuracy and precision of the proposed method. Subsequently, the method was tested with clinical data from ten patients with various types of brain tumors. The BSW correction method was applied as a reference approach.

In the simulations vascular parameters were estimated over a wide range of settings exhibiting minimal bias. Furthermore, the corrected $\Delta R_2^*$ curves closely aligned with the ground truth, effectively eliminating leakage contamination. In the clinical study, the mean estimated $K^{trans}$ was $(9.31 \pm 7.56) \times 10^{-4} \mathrm{s}^{-1}$, the vascular volume fraction $v_c$ was $0.05 \pm 0.03$, and the extracellular extravascular volume fraction $v_e$ was $0.17 \pm 0.06$. The DCE model fitting achieved a mean adjusted $R^2$ of $0.98 \pm 0.01$. From the DSC data, the estimated tissue relaxivity $r^*_{2,tissue}$ was $71.9 \pm 49.2 \mathrm{mM}^{-1} \cdot \mathrm{s}^{-1}$ with a mean adjusted $R^2$ of $0.87 \pm 0.08$. The method effectively reduced leakage artifacts while preserving residual contrast levels post-bolus, unlike the BSW method, which enforced the tail of the $\Delta R_2^*$ curves to baseline.

In conclusion, the proposed method effectively mitigates leakage artifacts while preserving important vascular information. These findings suggest that combined DCE and DSC imaging analyses could improve CBV estimation in brain tumors. Further studies with larger cohorts are warranted to validate these results and support clinical adoption.

## 5.1. INTRODUCTION

Dynamic susceptibility contrast (DSC) MRI is a perfusion imaging technique that utilizes gadolinium-based contrast agents (GBCAs) to assess properties of the cerebral perfusion through dynamic $T_2^*$-weighted imaging. Specifically, the paramagnetic GBCA induces a signal drop as the contrast bolus passes through a region of interest. By monitoring the signal changes and converting them into concentration-time curves, quantitative perfusion parameters such as cerebral blood volume (CBV), cerebral blood flow (CBF), and mean transit time (MTT) can be estimated. Among these, CBV is particularly valuable in brain tumor diagnostics, offering insight into tumor hemodynamics, grading, treatment response, prognosis, and differentiation between tumor recurrence and radiation necrosis [1]. A crucial assumption in the calculation of the CBV is that the contrast agent remains confined within the cerebral vasculature, so that there is no extravasation into the extracellular extravascular space (EES). However, in brain tumors the blood-brain barrier (BBB) may be compromised, leading to contrast leakage during imaging. This leakage induces $T_1$ enhancement, that will counteract the $T_2^*$ effects. A common approach to mitigate this issue is to inject a preload bolus of the contrast agent before the DSC acquisition [2]. The extravasation of the preload contrast agent shortens the $T_1$-time of the EES to such an extent that further extravasation of contrast agent during the main DSC bolus induces but limited additional signal increase. However, remaining leakage can still affect the measurements via $T_2^*$ changes as well as residual $T_1$ effects [3], necessitating the application of post-processing methods to avoid a bias in the parameter estimation [4–7]. Still, a preload bolus combined with post-processing corrections is an often applied strategy in clinical implementations due to their relative simplicity.

Among the post-processing algorithms addressing GBCA leakage, the unidirectional Boxerman–Schmainda–Weisskoff (BSW) method [4] has been initially widely used, e.g. via commercially available software [8]. The BSW method aims to reconstruct a true $\Delta R_2^*$ curve, which refers to the curve that would have been measured without the $T_1$ or $T_2^*$ effects on the signal due to extravasation of contrast agent. Implicitly, it is assumed that this true curve is linearly proportional to the average $\Delta R_2^*$ curve measured in areas without extravasation, i.e. in healthy tissue. This assumption allows for compensating the measured $\Delta R_2^*$ curve for remaining leakage. Specifically, the correction term is a linear function of the time integral of the averaged $\Delta R_2^*$ curve. More recently, the BSW model was extended to include bidirectional contrast agent exchange, accounting for the reflux of GBCA from the EES back to the plasma [7]. Studies have shown that CBV measurements from DSC imaging after a preload and using the BSW method correlate well with histological data in high-grade glioma patients [9, 10]. Despite these results, limitations remain regarding the accuracy of the correction method. For instance, the assumption regarding the linearity to the average $\Delta R_2^*$ curve is not valid when the MTTs are different between normal and malignant tissues [5, 6, 11, 12], and if the $T_1$ enhancement exceeds about 30% [11, 13]. Therefore, a more accurate estimation of tissue concentration without assumptions could further improve leakage correction.

Dynamic contrast enhanced (DCE) MRI is another technique that uses GBCA's to derive properties of the vascularization from $T_1$-weighted imaging. The resulting $T_1$-weighted images can be used to classify tissue types, e.g. through qualitative analysis of the signal intensity-time curves [14]. Furthermore, these data are often analyzed using pharmacokinetic models, among which the extended Tofts model (ETM) is the most widely applied approach [15, 16]. The ETM asserts that there are two compartments in which the GBCA can reside: the blood plasma and the EES. Importantly, it enables gauging of the quantitative vascular permeability parameters, such as the volume transfer constant $K^{trans}$.

In this paper, we aim to study the potential of leakage correction based on DCE and DSC imaging performed sequentially, back-to-back, and including two separate GBCA injections. In practice, this would imply that the preload injection is used for the DCE-measurements. We aimed to combine the DCE and DSC data analyses, using vascular parameters and tissue concentrations derived from DCE imaging to predict and correct leakage effects in DSC imaging. We hypothesized that this approach would diminish the impact of GBCA leaked into tissue on the $\Delta R_2^*$ curve, leading to more accurate CBV estimation. It would also use the strong points of both techniques: leakage estimation by DCE and CBV mainly determined by DSC. The BSW method was applied for comparison, as a reference correction approach.



## 5.2. THEORY

### 5.2.1. GRADIENT ECHO SIGNAL

The spoiled gradient echo sequence is a commonly used MRI technique in GBCA perfusion imaging. The steady state signal ($S$) in a homogeneous sample generated by this sequence is described by the following equation:

$$S = M_0 \cdot \sin\alpha \cdot \frac{1 - e^{\frac{-TR}{T_1}}}{1 - \cos\alpha \cdot e^{\frac{-TR}{T_1}}} \cdot e^{\frac{-TE}{T_2^*}}, \tag{5.1}$$

in which $M_0$ represents the net magnetization, $\alpha$ is the flip angle, $TR$ is the repetition time, $TE$ is the echo time, and $T_1$ and $T_2^*$ denote the longitudinal and transverse relaxation times, respectively. Upon administration of the GBCA, the two relaxation times are altered, leading to a change in signal intensity as a function of the local GBCA concentration $C$:

$$\frac{1}{T_1} = \frac{1}{T_{10}} + r_1 \cdot C, \tag{5.2}$$

and

$$\frac{1}{T_2^*} = \frac{1}{T_{20}^*} + r_2^* \cdot C, \tag{5.3}$$

in which $T_{10}$ and $T_{20}^*$ represent the initial longitudinal and transverse relaxation time, respectively, and $r_1$ and $r_2^*$ denote the longitudinal and transverse relaxivity

of the GBCA, respectively.

### 5.2.2. FOUNDATIONS OF DSC MRI

In DSC imaging, it is usually assumed that contrast agent leakage is negligible and that $T_2^*$ effects induced by the GBCA in the capillaries dominates the signal in a voxel, while $T_1$ effects can be ignored. Under these circumstances, Equation 5.1 can be simplified as:

$$S_{DSC}(t) = M_0 \cdot \sin\alpha \cdot e^{-TE(\frac{1}{T_{20}^*} + r_2^* \cdot C_v(t)}, \tag{5.4}$$

in which $C_v(t)$ is the time-dependent GBCA concentration in the voxel. The GBCA is confined to the capillaries in the absence of leakage, so that $C_v(t) = CBV * C_c(t)$, in which $C_c$ is the GBCA concentration in the capillaries. From the equation it can be deduced that the change in transverse relaxation rate is linearly related to the concentration of the contrast agent, i.e. $\Delta R_2^*(t) = r_2^* \cdot C_v(t)$:

$$\Delta R_2^*(t) = -\frac{1}{TE} \cdot ln(\frac{S_{DSC}(t)}{S_{DSC}(0)}), \tag{5.5}$$

in which $S_{DSC}(0)$ is the baseline signal before GBCA administration, corresponding to Equation 5.4 with $C_v(0) = 0$.

In brain tumors, however, the GBCA can leak into the EES due to a compromised BBB. Asserting a small volume of the capillaries, the $T_1$-time in tissue is especially affected by the extravasated GBCA concentration. As a consequence, the DSC signal in a voxel in the presence of leakage is conventionally modeled as:

$$\hat{S}_{DSC}(t) = M_0 \cdot \sin\alpha \cdot \frac{1 - e^{-TR\cdot(\frac{1}{T_{10}} + r_1 \cdot C_E(t))}}{1 - \cos\alpha \cdot e^{-TR\cdot(\frac{1}{T_{10}} + r_1 \cdot C_E(t))}} \cdot e^{\frac{-TE}{T_{20}^*}} \cdot e^{-TE\cdot r_2^* \cdot (C_{vc}(t) + C_E(t))}, \tag{5.6}$$

in which $C_{vc}(t)$ represents the contribution to the total voxel's GBCA concentration emanating from the capillaries (as above $C_{vc}(t) = CBV * C_c(t)$); furthermore, $C_E(t)$ is the contribution to the voxel GBCA concentration resulting from the extravascular space (analogously $C_E(t) = (1 - CBV) * C_{EES}(t)$). Based on this equation and using the baseline signal in which both concentrations are 0, an estimate of the change in transverse relaxation rate when leakage is present ($\Delta\hat{R}_2^*(t)$) can be defined as:

$$\begin{aligned} \Delta\hat{R}_2^*(t) \equiv & -\frac{1}{TE} \cdot ln(\frac{\hat{S}(t)}{S_0}) = \Delta R_2^*(t) \\ & - \frac{1}{TE} \cdot ln[\frac{1 - e^{-\frac{TR}{T_{10}}} \cdot e^{-TR\cdot r_1 \cdot C_E(t)}}{1 - \cos\alpha \cdot e^{-\frac{TR}{T_{10}}} \cdot e^{-TR\cdot r_1 \cdot C_E(t)}} \cdot \frac{1 - \cos\alpha \cdot e^{-\frac{TR}{T_{10}}}}{1 - e^{-\frac{TR}{T_{10}}}}] + r_2^* \cdot C_E(t). \end{aligned} \tag{5.7}$$

One can observe that the leaked concentration $C_E(t)$ modulates the $T_1$-time in the second term in this equation that is subtracted from $\Delta R_2^*(t)$. Simultaneously, it affects $\Delta R_2^*(t)$ in the third term that is proportional to $r_2^*$. As such, estimates of

$C_E(t)$ and $r_2^*$ could enable the computation of these leakage terms, according to which the contaminated transverse relaxation rate could be corrected to yield the underlying true $\Delta R_2^*(t)$.

### 5.2.3. LEAKAGE ESTIMATION

DCE MRI is well known to facilitate measurement of the $K^{trans}$ parameter, which reflects capillary permeability. We exploit DCE imaging performed during DSC preloading to determine the leaked concentration $C_E(t)$.

Importantly, the signal from DCE imaging also adheres to Equation 5.1. However, since the applied echo time is typically small, the $T_2^*$ effect is usually ignored, so that the DCE signal in a homogeneous sample can be described as:

$$S_{DCE}(t, C(t)) = M_0 \cdot \sin\alpha \cdot \frac{1 - e^{-TR\cdot(\frac{1}{T_{10}} + r_1 \cdot C(t))}}{1 - \cos\alpha \cdot e^{-TR\cdot(\frac{1}{T_{10}} + r_1 \cdot C(t))}}, \tag{5.8}$$

in which $C(t)$ is, as above, the local GBCA concentration.

We assert that the DCE signal in the presence of leakage, is a weighted average of the DCE signal from the capillaries $S_c$ and the extravascular space $S_E$:

$$S_{DCE,region}(t) = v_c \cdot S_{DCE,c}(t, C_c(t)) + (1 - v_c) \cdot S_{DCE,E}(t, C_E(t)), \tag{5.9}$$

in which $v_c$ represents the volume fraction of the blood vessels, relative to the total space of the region.

A close approximation of the GBCA concentration in the capillaries is given by the arterial input function (AIF): $C_c(t) \approx C_a(t)$. The AIF generally represents the GBCA concentration inside the vasculature that is flowing into the tissue, which can be measured in a nearby artery. Furthermore, the extravascular concentration can be derived from the ETM [15]:

$$C_E(K^{trans}, v_e, t) = K^{trans} \cdot \frac{C_a(t)}{1 - Hct} \circledast e^{-\frac{K^{trans}}{v_e}\cdot t}, \tag{5.10}$$

in which $K^{trans}$ represents the GBCA exchange rate from the plasma to the EES, and $v_e$ is the fractional volume of the EES.

By normalizing the regional signal intensity-time curve ($S_{DCE,region}(t)$) with the baseline signal, e.g. at t=0, a detailed DCE ratio signal model $D(K^{trans}, v_c, v_e, t)$ results:

$$\begin{aligned} D_{DCE}(K^{trans}, v_c, v_e, t) &= \frac{S_{DCE,region}(t)}{S_{DCE,region}(0)} \\ &= \frac{v_c \cdot S_{DCE,c}(t, C_a(t)) + (1 - v_c) \cdot S_E(t, C_{DCE,E}(K^{trans}, v_e, t))}{v_c \cdot S_{DCE,c}(0,0) + (1 - v_c) \cdot S_{DCE,E}(0,0)} \end{aligned} \tag{5.11}$$

$K^{trans}$, $v_c$, and $v_e$ can be estimated by fitting this model to a measured DCE signal

ratio curve from a region of interest. Subsequently, $C_E$ is obtained via Equation 5.10 which can then be used for leakage correction through Equation 5.7.

### 5.2.4. ESTIMATION OF $r_2^*$

It is usually asserted that the longitudinal relaxivity ($r_1$) is relatively constant across different tissue types [17]. Instead, the transverse relaxivity $r_2^*$ is presumed higher in tissue than in arteries, while there is no established consensus on its exact value [18–20]. To determine the particular $r_2^*$ in a region, a model comparable to Equation 5.11 is applied to fit the measured signal ratio curves in the DSC data. Distinguishing separate signal contributions for the capillaries and the extravascular space and normalizing it with the baseline signal yields the next signal ratio expression for the DSC signal:

$$
\begin{aligned}
&D_{DSC}(T_{1,tissue}, r^*_{2,tissue}, t) = \\
&\Bigg( v_c \cdot \frac{1 - e^{-TR\cdot(\frac{1}{T_{10,c}} + r_1 \cdot C_c(t))}}{1 - \cos\alpha \cdot e^{-TR\cdot(\frac{1}{T_{10,c}} + r_1 \cdot C_c(t))}} \cdot e^{-TE\cdot(\frac{1}{T^*_{20,c}} + r^*_2 \cdot C_c(t))} \\
&+ (1 - v_c) \cdot \frac{1 - e^{-TR\cdot(\frac{1}{T_{10,E}} + r_1 \cdot C_E(t))}}{1 - \cos\alpha \cdot e^{-TR\cdot(\frac{1}{T_{10,E}} + r_1 \cdot C_E(t))}} \cdot e^{-TE\cdot(\frac{1}{T^*_{20,E}} + r^*_2 \cdot (C_E(t) + v_c \cdot C_c(t))} \Bigg) \\
&/ (v_c \cdot S_{DSC,c}(0,0) + (1 - v_c) \cdot S_{DSC,E}(0,0)).
\end{aligned}
\tag{5.12}
$$

In this equation we set $C_c(t) = C_a(t) + L$ (as above), in which $L$ is the concentration of the AIF in the last image acquired during the prebolus injection. Note that $t = 0$ now refers to the baseline (first images) of the DSC scan. Furthermore, injection time and protocol are assumed to be the same as for the DCE-scan. Also, observe that $v_c, C_E(t)$ were determined in the previous step via Equations 5.10 and 5.11. Here we assume that the concentration of the GBCA in the capillaries and in tissue is in equilibrium at the start of the DSC injection. Finally, $T_{10,c}$, $T^*_{20,c}$ and $T^*_{20,E}$ are assumed to be known constants (see below for their settings). As such $r_2^*$ and $T_{10,E}$ (due to the prebolus injection) are unknown parameters. These are determined by fitting the equation to the measured DSC ratio curve after which the two estimated parameters can be applied in the correction equation (Equation 5.7).

## 5.3. MATERIALS AND METHODS

### 5.3.1. SIMULATIONS

Several simulations were performed to assess the accuracy and precision of the parameter estimation and the leakage correction under controlled circumstances. All simulations were performed using custom Matlab scripts (version R2020b; MathWorks, Natick, MA, USA).

### GENERATING THE SIGNALS

We simulated a clinical scenario with two consecutive GBCA injections, each with a standard dosage of 0.1 mmol/kg. The (DCE) signal from preload injection was simulated for a duration of 200 seconds, after which the (DSC) signal from the second contrast bolus was simulated for an additional 200 seconds. Both injections were modeled using Orton's AIF model with population-averaged parameters [21], applying a bolus arrival time set at 20 seconds. To simulate physiological conditions, however, the second AIF was superimposed onto the first one, taking residual contrast agent from the preloading into account. As such a composited input function was constructed. The extravasation of GBCA into the EES was subsequently modeled based on the ETM through Equation 5.10.

Tumour $D_{DCE}$ curves were simulated by combining contributions from both the capillaries and the extravascular compartment via Equation 5.11. The signal components of this equation were generated by converting the GBCA concentrations into MRI signal intensity using Equations 5.1 through 5.3. Furthermore, $D_{DSC}$ curves were simulated via Equation 5.12. The input concentrations for simulating the DSC signal corresponded to the composited input function for the capillary compartment.

All simulations applied the following physiological parameters: $Hct$ = 0.45, $T_{10}$ = 1.8 s for blood [22], $T_{20}^*$ = 0.02 s for blood and tissue [23], $r_1$ = 4.5 $(\text{mM}\cdot\text{s})^{-1}$ for gadobutrol [24], and a $r_2^*$ = 6 $(\text{mM}\cdot\text{s})^{-1}$ for gadobutrol in blood [25, 26]. Other parameters were varied as indicated in next section.

The DCE signal during the first bolus passage was simulated using parameters that were compatible with our clinical protocol: $TR$ = 2.7 ms, $TE$ = 0.9 ms, and $FA = 25°$. Subsequently, the DSC signals during the second bolus signal were generated with $TR$ = 2 s, $TE$ = 45 ms, and $FA = 90°$. Both signals were sampled at 2-second intervals, producing 100 samples per sequence. Gaussian white noise was added to the signal intensity curves to achieve a signal-to-noise ratio (SNR) of 40 decibels. The resulting signal intensity curves were normalized using the average baseline signal (first 5 samples) to produce signal ratio curves. The DSC signal ratio curve was also converted into a $\Delta R_2^*$ curve using Equation 5.5.

### ASSESSMENT OF THE ESTIMATION PERFORMANCE

We first investigated the feasibility of the proposed leakage correction method. The signal ratio curves were generated as explained in Section 5.3.1 while applying $K^{trans}$ = 0.001, $v_c$ = 0.03, $v_e$ = 0.3, $T_{1,tissue}$ = 1.2, and $r_{2,tissue}^*$ = 30. The DCE signal ratio model, as described in Equation 5.11, was fit to the simulated DCE signal ratio curves to estimate parameters $K^{trans}$, $v_c$, and $v_e$, which then served to compute $C_E(t)$. Subsequently, the outcomes were applied in the DSC signal ratio model (Equation 5.12), which was fit to the DSC signal ratio curves to estimate $T_{1,tissue}$ and $r_{2,tissue}^*$. The parameter estimates were constrained to be positive and were obtained using a nonlinear least squares regression approach. Thereafter the estimated parameters were used to derive the correction terms in Equation

5.7 to compute the "uncontaminated" $\Delta R_2^*$ curve. To assess the accuracy of the correction, a simulated $\Delta R_2^*$ curve with $K^{trans} = 0$ was used as the ground truth and compared with the corrected $\Delta R_2^*$ curve.

Additionally, a range of parameter values was applied to evaluate the robustness of the model fitting.: $0 < K^{trans}$ (1/s) $< 0.01$ (stepsize: 0.0005), $0 < v_c < 0.1$ (stepsize: 0.005), $0 < v_e < 1$ (stepsize: 0.05), tissue $T_1$ (s) ranging from 1 s to 2 s with a step size of 0.02, and tissue $r_2^*$ ($(\text{mM}\cdot\text{s})^{-1}$) ranging from 5 to 100 using a stepsize of 5. The estimation of the first three parameters was evaluated by fitting to the simulated DCE signal ratio curves, while the estimation of last two was evaluated by fitting to the simulated DSC signal ratio curves. Each parameter was varied while fixating the values for the other parameters in the signal simulation to the values defined in the first paragraph of this section. For each such test, 1000 simulations with different noise realizations were performed. Box plots were used to visualize the performance of the estimation.



### 5.3.2. APPLICATION WITH CLINICAL DATA

#### PATIENT COHORT

Patient recruitment for this study was approved by the Medical Ethics Committee at Erasmus MC in the Netherlands (NCT05798273). Patients with radiologically presumed and/or histologically confirmed grade 2–4 glioma showing enhancement on post-contrast MRI, or brain metastasis, and with complete relevant imaging data available were included. As such, ten patients were enrolled, in which the following brain tumors were histologically confirmed: glioblastoma (n = 4), oligodendroglioma (n = 1), and brain metastasis from lung cancer (n = 4) and breast cancer (n = 1). Written informed consent was obtained from all patients.

#### IMAGING PROTOCOL

Image acquisition was performed on a 3T whole-body hybrid PET-MRI system (Signa PET-MR, GE Healthcare, Chicago, IL, USA) with a 24-channel head coil at Erasmus MC in the Netherlands.

Prior to contrast-enhanced imaging, the Magnetic Resonance Image Compilation (MAGiC) sequence was applied with field of view (FOV): 240 × 240 $mm^2$, acquisition matrix size: 320 × 256, reconstructed matrix size: 512 × 512, reconstructed resolution: 0.47 × 0.47 $mm^2$, and slice thickness: 4 mm, acquiring a total of 40 slices. Phase-sensitive inversion recovery (PSIR) images were generated from the MAGiC sequence with 12 inversion times (TIs) ranging from 25 to 3000 ms. In addition, $T_2$-weighted images were acquired via the Periodically Rotated Overlapping ParallEL Lines with Enhanced Reconstruction (PROPELLER) sequence in axial view with TR/TE: 9182/149 ms, voxel size: 0.5 × 0.5 × 3 $mm^3$, FOV: 400 x 400 $mm^2$, obtaining 59 slices. Furthermore, a fluid attenuated inversion recovery (FLAIR) imaging was performed with TR/TE: 7602/136 ms, voxel sizes: 0.5 × 0.5 × 1.6 $mm^3$, FOV: 224 x 224 $mm^2$, acquiring 208 slices.

In each patient, 7.5 mL of gadobutrol (Gadovist®, Bayer, Germany)—corresponding to a standard dose for a 75 kg patient—followed by a 15 mL saline flush, was automatically injected via the antecubital vein at 5 mL/s using a power injector during DCE imaging. Immediately after the DCE acquisition, a second bolus of contrast agent with the same dose was injected in the same way during DSC imaging. The contrast agent injections were initiated 20 seconds after the commencement of the DCE and DSC acquisitions, respectively.

DCE images were acquired using the differential subsampling with Cartesian ordering sequence [27] with TR/TE: 2.7/0.9 ms, flip angle (FA): 25°, FOV: 240 × 240 × 144 $mm^3$, acquisition matrix size: 160 × 128, reconstructed matrix size: 256 × 256 resulting a reconstructed resolution of 0.9 × 0.9 $mm^2$, slice thickness: 3 mm, 48 slices, and temporal resolution of 2 s, acquiring a total of 100 image volumes. DSC images were obtained through a $T_2^*$-weighted gradient-echo echo-planar imaging sequence with TR/TE: 2000/45 ms, FA: 90°, FOV: 256 × 256 × 100 $mm^3$, matrix size: 128 × 128, 20 slices, in-plane resolution: 2 × 2 $mm^2$, slice thickness: 5 mm, and temporal resolution: 2 s, acquiring a total of 50 dynamics.

Finally, 3D fat-suppressed fast spoiled gradient echo (FSPGR) $T_1$ images were obtained immediately both before and after the dynamic contrast enhanced series using TR/TE: 7.7/3.1 ms, voxel size: 0.9 × 0.9 × 1.6 $mm^3$, FOV: 256 × 256 $mm^2$, to acquire two sets of 228 slices.

### PRE-PROCESSING

Preprocesing comprised the registration of all the imaging data, segmenting the the tumor from the data and computing a $T_1$ map.

Initially, the pre-contrast $T_1$-weighted image and the $T_2$-weighted and FLAIR scans were rigidly, in a groupwise fashion registered to the post-contrast $T_1$-weighted images. This registration was followed by an affine registration to the ICBM 152 2009a nonlinear symmetric atlas using Elastix (version 5.0.1) [28–30]. Automatic segmentation was then performed using multiple algorithms: HD-GLIO [31, 32], nnU-Net tasks 1 and 82, and an extended version of nnU-Net [32, 33]. The segmentation outputs from these algorithms were combined using the multi-label Simultaneous Truth and Performance Level Estimation algorithm [34]. The segmented contrast-enhancing tumor regions were then visually inspected and manually corrected if necessary using ITK-SNAP version 3.6.0 (University of Pennsylvania and Utah, USA) [35] to yield a final tumor mask. During this process, areas corresponding to blood vessels, necrosis, and post-operative resection cavities were excluded from the segmentation.

A two-parameter exponential recovery function was fitted to the MAGiC PSIR volumes to derive a whole-brain initial $T_1$ map [36].

The post-contrast $T_1$ image was coregistered to both the first DCE and DSC volumes, and the resulting transformations were also used to transfer the tumor mask onto the DCE and DSC images, respectively. Thereafter, the 3D $T_1$ map derived from the MAGiC sequence was also registered to the first DCE volume

to facilitate the subsequent analysis. These registrations were performed using a 3D affine transformation optimizing the normalized mutual information, as implemented in Statistical Parametric Mapping (SPM) version 12 [37].

The DCE and DSC series were corrected for potential motion during scanning by rigidly registering the entire series to the first volume of the DCE and the DSC series, respectively. This was achieved using a least squares approach and a six-parameter rigid body spatial transformation, as implemented in SPM12 [38].

#### APPLICATION

Average signal intensity-time curves from the DCE and DSC series were computed over the tumor mask. Both curves were normalized by dividing each time point with the baseline signal to generate signal ratio curves for DCE and DSC imaging.

#### DCE IMAGE PROCESSING

A small group of voxels in an artery were manually selected in the hemisphere containing the tumor to determine the AIF. These voxels were selected as closely as possible to the tumor in the last acquired volume of the DCE series. Subsequently, the mean of the signal values over this group was computed for each time point, which was then divided by the baseline signal to yield the AIF's signal ratio curve. Here, the baseline signal was determined by averaging the time points before the bolus arrived. The bolus arrival time was visually identified. Finally, inflow and partial voluming were corrected as described in [39, 40] to generate the AIF. Next, the DCE signal ratio model (Equation 5.11) was fit to the DCE signal ratio curve from the tumor using the estimated AIF. To this end, $T_{10}$ in the capillaries was assumed to be 1.8 s, while $T_{10}$ in tissue was set to the average value over the tumor mask in the PSIR $T_1$ map. As such, the vascular coefficients $K^{trans}$, $v_c$, and $v_e$ for each patient were obtained. Finally, the leaked GBCA concentration was derived using Equation 5.10.

#### DSC IMAGE PROCESSING

The DCE-derived AIF as described in the previous paragraph was also used in the DSC analysis. This was done since we have found that the DCE-AIF is more reliable than a DSC-based AIF [41]. The AIF and estimated leaked GBCA concentration were manually shifted to align with the measured DSC signal ratio curve, specifically to match the bolus arrival time. The DSC signal ratio model (Equation 5.12) was then fitted to the measured DSC signal ratio curve to estimate $T_{10,E}$ and the tissue $r_2^*$.

#### LEAKAGE CORRECTION

The measured signal ratio curve over the tumor mask from the DSC imaging was used as the argument of the natural logarithm, on the left handside of Equation 5.7. Subsequently, the estimated leaked concentration $C_E(t)$ and $T_{10,E}$ were applied

to compute the second term on the right hand side of this equation and $C_E(t)$ combined with the tissue's $r_2^*$ were used to compute the third term of the equation. Finally, bringing these terms to left hand side yielded the uncontaminated $\Delta R_2^*$ curve from the equation.

#### EVALUATION

The mean and standard deviation of each estimated parameters in the DCE and DSC analyses were assessed. The goodness-of-fit of the models was evaluated using the root mean square error (RMSE) and the adjusted R-square value of both the DCE and DSC parameters.

The RMSE was calculated through:

$$\text{RMSE} = \sqrt{\frac{1}{n-k}\sum_{i=1}^{n}(y_i - \hat{y}_i)^2} = \sqrt{\frac{\text{SSE}}{n-k}}, \tag{5.13}$$

in which $y_i$ is the observed value, $\hat{y}_i$ is the model-predicted value, $n$ is the number of observations, and $k$ is the number of independent variables in the model. Thus, an RMSE value close to 0 indicates a better fit between the model and the data, signifying smaller discrepancies between observed and predicted values.

To account for the number of fitted parameters, c.q. adjust for the number of terms, the adjusted R-square ($R^2_{\text{adj}}$) was computed:

$$R^2_{\text{adj}} = 1 - \left(\frac{\text{SSE}/(n-k)}{\text{SST}/(n-1)}\right), \tag{5.14}$$

with $\text{SSE} = \sum_{i=1}^{n}(y_i - \hat{y}_i)^2$ is the sum of squared residuals, $\text{SST} = \sum i = 1^n (y_i - \bar{y})^2$ is the total sum of squares, and $\bar{y}$ is the mean of the observed data. An $R^2_{\text{adj}}$ value closer to one indicates a better fit while accounting for the complexity of the model. Specifically, a $R^2_{\text{adj}}$ value greater than 0.85 was considered indicative of a very good fit; values between 0.75 and 0.85 were taken to indicate a good fit; and values below 0.75 were assumed to correspond to a moderate to poor fit.

To further assess the efficacy of our leakage correction approach, the BSW method was applied to each patient for comparison. Graphs were created of the uncorrected $\Delta\hat{R}_2^*$ curve, the curve corrected using the proposed method and the curve resulting from the BSW method. These graphs were visually compared.

## 5.4. RESULTS

### 5.4.1. SIMULATION RESULTS

The feasibility of the proposed leakage correction method is illustrated in Figure 5.1. Specifically, Figure 5.1a) shows the simulated DCE signal ratio curve corresponding to injection of a first bolus and the fitted model c.f. Equation 5.11. Likewise, Figure 5.1b shows the simulated DSC ratio curve related to injection of the

second bolusand the fitted model as represented in Equation 5.12. The estimated parameters of these fits and their simulated reference values are presented in the inset. The indicated reference $T_1$ value takes the $T_1$ shortening induced by the preload into account, yielding a markedly lower value than prior to both contrast injections (i.e. 0.5 s versus 1.2 s). Finally, Figure 5.1c) shows the uncorrected $\Delta\hat{R}_2^*$ curve, computed from the simulated DSC signal ratio curve through Equation 5.5, the corrected curve, based on the estimated parameters, and the reference curve, assuming no leakage. It can be observed that our models fit well with the simulated signal ratio curves, leading to a corrected $\Delta R_2^*$ curve that closely follows the reference curve.

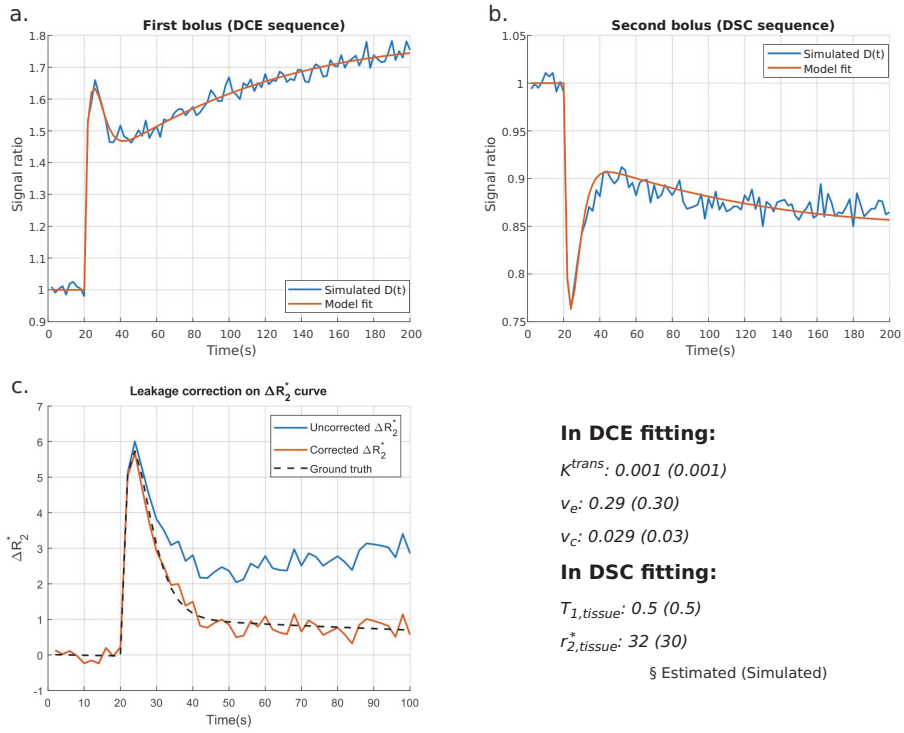


Figure 5.1: (a),(b) Simulated DCE and DSC signal ratio curves and corresponding model fits; (c) uncorrected, corrected and reference $\Delta R_2^*$ curves. The inset shows the associated estimated and reference parameter values.

Figure 5.2 shows boxplots reflecting the variability in parameter estimation from noisy simulated DCE ratio curves, as a function of varying input parameter values. Notice that per plot one parameter is varied while the other (two) parameters were kept constant as indicated in the headings. The deviation of the boxes from the dashed lines reflects a small bias in the estimation. Furthermore, increasingly larger variation in estimated $v_e$ is noticeable as the simulated $v_e$ value increased, reflecting increasingly larger EES.

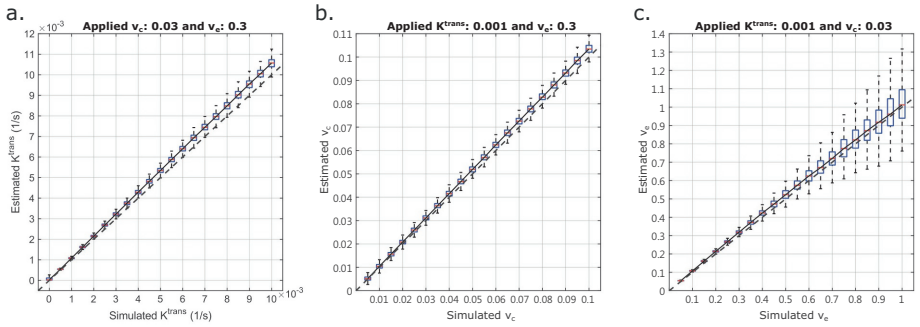


Figure 5.2: Boxplots representing estimated parameter distributions and reference values, while varying (a) $K^{trans}$, (b) $v_c$, and (c) $v_e$. Parameters kept constant are indicated above each graph. Whiskers reflect 1.5 times the interquartile range. The dashed lines reflect the reference values.

5

Similarly, boxplots representing the variability in parameter estimation from noisy simulated DSC ratio curves are shown in Figure 5.3. While the $r_2^*$ plots signify high accuracy and precision of the parameter estimations, a slight bias can be observed in the predicted $T_1$ values. The whiskers reflect a variation in $T_1$ parameter estimates of approximately 10%. Notice that the reference tissue $T_1$ value represents the simulated $T_1$ value modulated by the last observed GBCA concentration from the preload, as described by Equation 5.2.

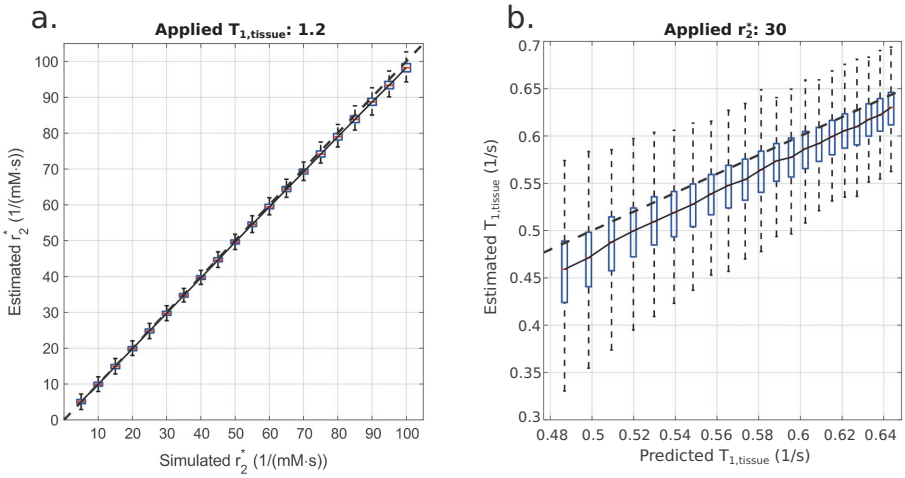


Figure 5.3: Boxplots showing estimated versus simulated DSC parameter values while varying (a) tissue $r_2^*$ and (b) tissue $T_1$, just as in Figure 5.2. Again, the dashed lines reflect the reference values.

### 5.4.2. CLINICAL APPLICATION RESULTS

Table 5.1 collates the mean and standard deviation of the estimated parameters and the goodness-of-fit measures for both the DCE and the DSC fits across all patients. The RMSE values are small and close to zero, reflecting small discrepancy between the applied models and the measured signal ratio curves. Furthermore, the $R^2_{\text{adj}}$ values reflect that the signal ratio models provided good fits given the number of parameters. The DSC analysis gave slightly lower average $R^2_{\text{adj}}$ value, as three patients yielded moderate to good $R^2_{\text{adj}}$ values.

| | DCE Analysis | DSC Analysis |
|---|---|---|
| $K^{trans}(\times 10^{-4})$ | $9.31 \pm 7.56$ | – |
| $v_c$ | $0.05 \pm 0.03$ | – |
| $v_e$ | $0.17 \pm 0.06$ | – |
| $T_{1,tissue}$ | – | $1.64 \pm 1.07$ |
| $r^*_{2,tissue}$ | – | $71.9 \pm 49.2$ |
| RMSE | $0.05 \pm 0.02$ | $0.04 \pm 0.03$ |
| $R^2_{\text{adj}}$ | $0.98 \pm 0.01$ | $0.87 \pm 0.08$ |

Table 5.1: Mean and standard deviation of estimated parameters and goodness-of-fit measures. Data are reported as mean ± standard deviation.

Figure 5.4 shows original data, model fits and leakage correction outcomes for a representative patient. Panels (a) and (b) display the measured DCE and DSC signal ratio curves as well as the associated model fits, respectively. All other DCE and DSC data and fitting results are presented in Supplementary Figures S5.1 and S5.2. The $T_1$ and $T_2^*$ leakage terms c.f. in Equation 5.7, calculated using the estimated coefficients, as well as the uncorrected (contaminated) $\Delta\hat{R}^*_2(t)$ term are plotted in Figure 5.4c. Finally, Figure 5.4d shows the uncorrected $\Delta\hat{R}^*_2(t)$ curve and the corrected curve resulting from our method and the one from the BSW method.

The leakage correction results for all other 9 patients are presented in Figure 5.5. Effectively, our method markedly suppresses the leakage effect, i.e. the tail of the $\Delta\hat{R}^*_2(t)$ curve. In contrast, it can be observed that the BSW method consistently reduces the tail of the curve to baseline level. This was observed also in a case with balanced $T_1$ and $T_2^*$ corrections (Figure 5.5e) and in two cases with dominating $T_1$ correction (Figures 5.5d and i).

## 5.5. DISCUSSION

In this paper, we introduced a novel correction method for DSC MRI that leveraged DCE MRI for estimating and reducing leakage effects. Corrected $\Delta R^*_2$ curves

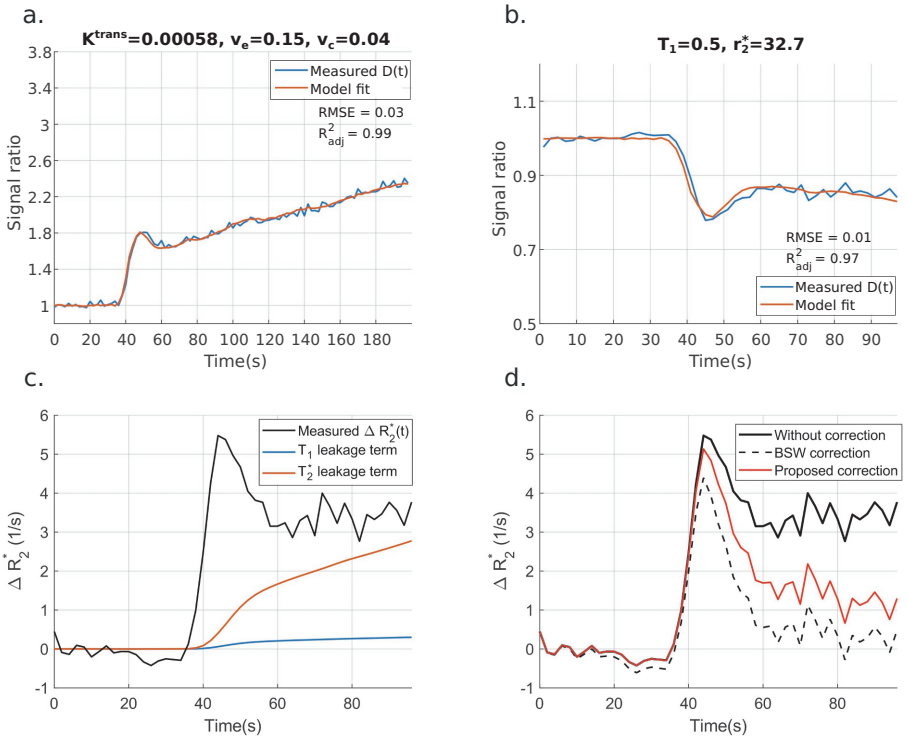


Figure 5.4: Example curves from a representative patient. (a) DCE and (b) DSC signal ratio curves with model fits; (c) $T_1$ and $T_2^*$ leakage terms from Equation 5.7 as well as the contaminated (uncorrected) $\Delta\hat{R}_2^*(t)$ curve; (d) uncorrected $\Delta\hat{R}_2^*(t)$ curve and curves corrected through the proposed approach and the BSW method.

accurately followed the ground truth in simulations, while realistic corrections resulted with practical data.

By combining DCE and DSC imaging analyses performed sequentially, our approach capitalizes on the strengths of both techniques: DCE MRI provides accurate estimation of vascular permeability and leaked contrast concentration, while DSC MRI offers high sensitivity to cerebral blood volume. This integration allows for precise correction of leakage artifacts in DSC data, overcoming limitations of conventional methods approach. Specifically, our method does not rely on the assumption to the leakage component and incorporates gauging of the $T_1$ and $r_2^*$ constants prior to the (second) bolus injection. This can enhance the reliability of CBV measurements in brain tumors and may lead to better tumor characterization, treatment planning, and monitoring of therapeutic response.

The simulation experiments showed that our approach theoretically facilitates accurate estimation of underlying parameters and appropriate modeling of signal

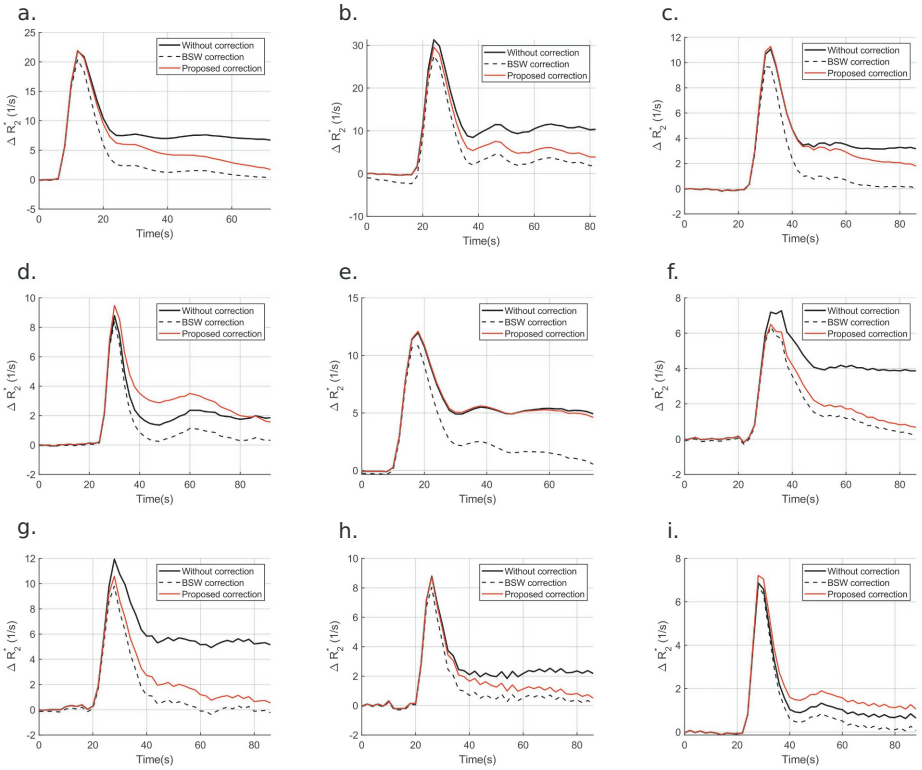


Figure 5.5: Leakage correction outcomes for each patient (a)-(i). Each graph shows the uncorrected $\Delta\hat{R}_2^*(t)$ curve and curves corrected through the proposed approach and the BSW method as in Figure 5.4d.

ratio curves both for DCE and DSC imaging (Figure 5.1). In particular, the simulations demonstrated that wide ranges of vascular parameters underlying the DCE and DSC data were determined with only marginal bias and high precision (Figure 5.2 and 5.3), except for the $T_{1,tissue}$ parameter. The graph for the latter parameter reflected systematic underestimation and rather large variation compared with the other parameters. We attribute this to small errors in the estimated leaked GBCA concentrations between the first and second (simulated) injections. This was checked by simulating the DSC imaging without the prebolus injection, see Figure S5.3. In that case, no bias is observable while whiskers are markedly smaller. In all cases, the final effect of these errors is small (see e.g. Figure 5.1c). We attribute this to the preload injection, of which the extravasation beforehand shortens the tissue's $T_1$-time. Subsequently, the second injection has a smaller effect on the $T_1$ value, leading to dominating $T_2^*$ effect on the signal. This is also corroborated by Figure 5.4c.

Upon fitting our DCE signal ratio model to the measured signal ratio curves, the estimated parameters consistently fell within realistic physiological ranges [42],

see Supplementary Figure S5.1. Additionally, the RMSE values were low, and the $R^2_{adj}$ values indicated excellent fits. Regarding the DSC fitting, although the goodness-of-fit metrics indeed pointed at reliable fitting outcomes, the measured DSC signal ratio curves exhibited slightly wider dips than the fitted models. This discrepancy might arise from small errors propagating from the estimated DCE parameters or from the proposed model not perfectly representing the DSC signal. In spite of this misalignment, it should be noticed that the estimated tissue $r_2^*$ is primarily determined by the depth of the dip in the signal ratio curve, while the estimated tissue $T_1$ parameter is more influenced by the tail level of the curve. Since these aspects were fitted accurately, we believe that the estimated parameters are sufficiently reliable for the eventual leakage correction.

An particular strength of our method is in the included estimate of the tissue's transverse relaxivity, $r_2^*$, directly from the DSC data. This is important because $r_2^*$ is dependent on the microvascular architecture and geometry of the tissue, which can vary considerably between healthy tissue and tumors due to differences in vessel density, size, and permeability. By estimating $r_2^*$, our method inherently accounts for these variations in vascular structure, which can lead to more accurate leakage correction and CBV estimation. In our study, the estimated $r_2^*$ values were mostly within the reported range of 32 to 85 $mM^{-1} \cdot s^{-1}$ [43, 44], which aligns with known physiological values. Notably, in one case we observed exceptionally large estimated $r_2^*$ value (Figure S5.2d). This patient also exhibited a higher estimated tissue $T_1$ value compared to other cases. The simultaneously large $r_2^*$ and $T_1$ values eventually led to a corrected curve that is slightly higher than the original, non-corrected $r_2^*$ curve (Figure 5.5d). In general this can be the case when the $T_1$ term exceeds the $T_2^*$ term in Equation 5.7 (also observable in Figure 5.5i). Apparently, the large parameter values associated with S5.2d) compensated each other to some extent and did not lead to a very large deviation in the corrected curve.

One may observe that the corrected $\Delta R_2^*$ curves from our method generally did not go back to the 0-level in the tails. Instead, the corrected $\Delta R_2^*$ curves resulting from the BSW method did tend to return to this baseline level (Figures 5.4d and 5.5). This difference arises because the BSW approach assumes that the uncontaminated $\Delta R_2^*$ curve in leaked tissue is proportional to the average $\Delta R_2^*$ curve in normal-appearing tissue. Specifically, these voxels are usually identified as not exhibiting signal enhancement exceeding the baseline in the final time points after the first bolus [4]. As a result, the BSW correction may misinterpret regions that merely contain residual GBCA concentration in the vasculature as ones that harbor leaky vessels. This could be particularly problematic in richly vascularized areas, and might lead to an underestimation of the CBV. Instead, in our approach the leaked tissue concentration is computed from the DCE datasets and only this component is subtracted from the measured $\Delta R_2^*$ curve. In effect, any GBCA concentration that remains circulating in the vascular system is preserved in the tails of the $\Delta R_2^*$ curve by our method. What is more, the Boxerman approach assumes that the leakage-induced $T_1$ enhancement is less than 30% (see Equations A5 and A6 in [4]). However, this assumption may not hold true in tissues with

severe leakage as observed in our cases (e.g. Figure 5.5).

Leu et al. enhanced the BSW model by incorporating bidirectional contrast agent exchange, that accounts for the reflux of GBCA from the EES back to the plasma [7, 45]. Their approach resembles the model used in our DCE analysis, in which we defined the leaked GBCA concentration based on the ETM two-compartment, mutual exchange model. We still compared our approach to the BSW method, as it remains the most widely used leakage correction method in commercial tools [8]. Moreover, accounting for the reflux rate did not eliminate the assumptions inherent in the BSW method. Indeed, Arzanforoosh et al. [46] investigated both unidirectional and bidirectional models for leakage correction and found that the bidirectional approach often resulted in a lower relative CBV than the unidirectional method in both enhancing and non-enhancing areas. This could also reflect that the bidirectional model still forces the $\Delta R_2^*$ curves to return to baseline, even with an improved contrast exchange model.

Several other studies, with some variations, have also utilized the DSC signal in healthy tissue as a reference [5, 7, 45]. An extended two-step technique was introduced [12, 47], in which reference curves generated from the tissue residue function were used for leakage estimation. Applying a fundamentally different approach, Bjørnerud et al. [6] and Emblem et al. [48] determined the leakage component of the signal with a more complex model. These efforts in our opinion signify the complexity of recovering the uncontaminated tissue curve merely from the DSC series. Importantly, they served as an inspiration for us to combine DCE with DSC MRI, and using DCE to facilitate estimation of the leaked contrast agent concentration.

Recently, Sankaralayam et al. [49] utilized $K^{trans}$ for leakage correction in deriving CBV and CBF from DCE MRI for glioma grading. Notably, the use of $K^{trans}$ for correcting leakage contamination conceptually parallels our approach. However, their study involved only a mere DCE acquisition, unlike the back-to-back DCE and DSC imaging applied by us. Surprisingly, their findings suggested that leakage correction might negatively impact the accuracy of glioma grading via the DCE-driven perfusion parameters. This unexpected result could be due to the sensitivity of the applied model to noise.

Our study has several limitations. First, the clinical validation sample size was relatively small, consisting of ten patients with various types of brain tumors. We consider our work as a proof of concept, and concede that a larger cohort will surely be needed to further validate our method. Second, the assumption that the difference in the amount of leaking contrast agent between the first and second injections is minimal may not hold in all cases. Variations in vascular permeability and patient-specific factors could affect leakage dynamics, potentially postponing the equilibrium state. This concern could be addressed by extending the DCE scan, assuring that the equilibrium state is truly achieved. Finally, our image acquisition protocol could be further optimized. Specifically, the DCE sequence was acquired with a relatively large flip angle, resulting in a low SNR. To compensate for this, we applied a region-based analysis rather than performing a voxel-wise analysis.

## 5.6. CONCLUSION

We have developed a novel leakage correction method for DSC MRI that exploits DCE-derived vascular parameters to accurately estimate and correct for GBCA leakage effects. Our approach preserves residual contrast levels, which is often suppressed by conventional correction techniques. Our findings suggest that integrating DCE and DSC imaging analyses can enhance the reliability of perfusion measurements in patients with brain tumors. Further studies with larger cohorts are warranted to confirm the results and facilitate true practical adoption.

## 5.7. SUPPLEMENTARY MATERIAL

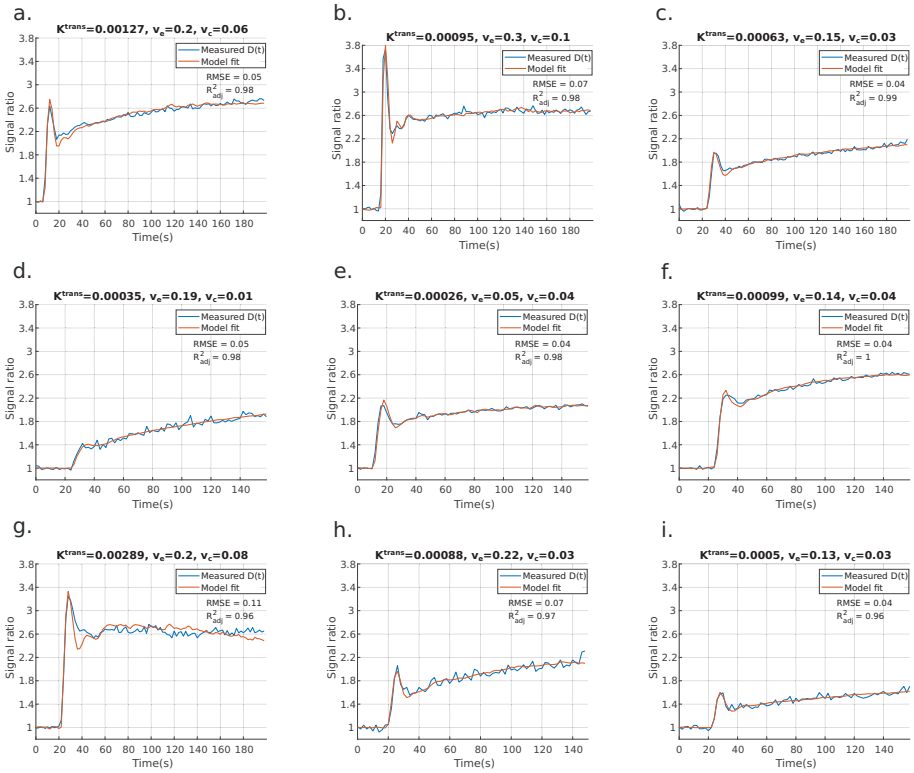


Figure S5.1: Individual DCE fitting results for all patients. Each plot shows the measured DCE signal ratio curve (blue curve) and the model fit (red line) for a single patient, illustrating the accuracy of the model across the cohort.

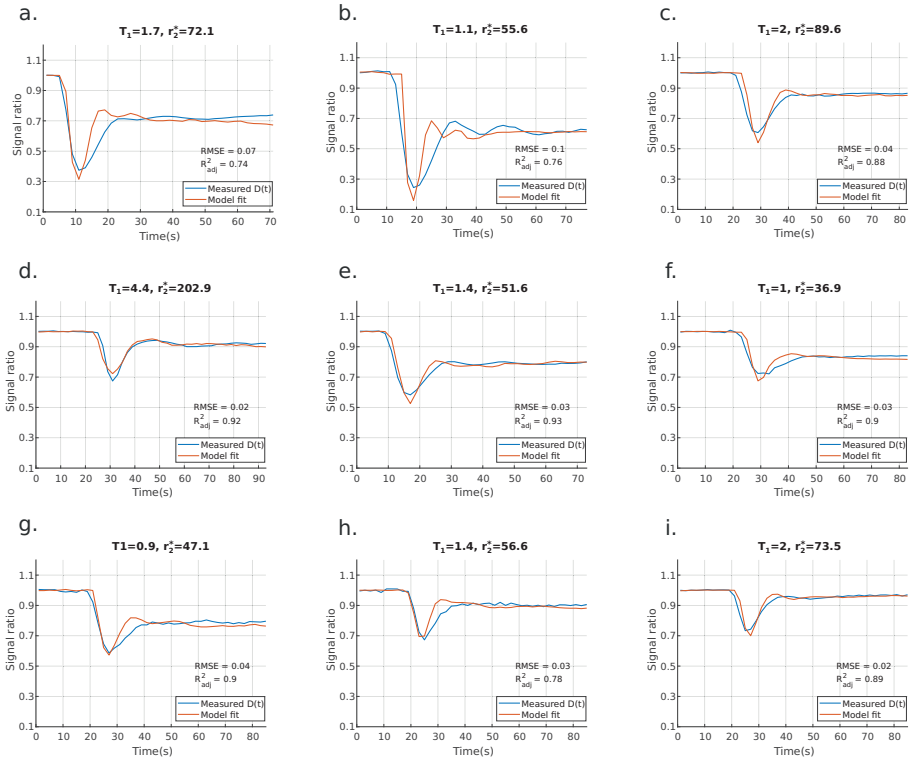


Figure S5.2: Individual DSC fitting results for all patients. Each plot displays the measured DSC signal ratio curve (blue curve) and the model fit (red line) for a single patient, demonstrating the effectiveness of the model in capturing the DSC dynamics across different patients.

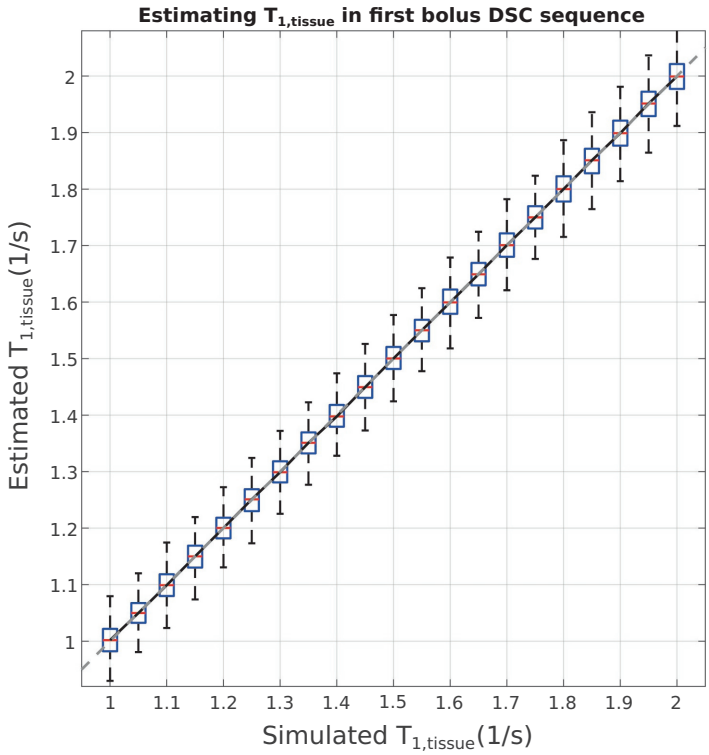


Figure S5.3: Boxplots showing estimated versus simulated DSC parameter values while varying tissue $T_1$ in first injection. The dashed lines reflect the reference values.

# REFERENCES


[1] M. S. Shiroishi *et al.* "Principles of T2*-weighted dynamic susceptibility contrast MRI technique in brain tumor imaging". In: *Journal of Magnetic Resonance Imaging* 41.2 (Feb. 2015), pp. 296–313. ISSN: 1053-1807. DOI: 10.1002/jmri.24648.

[2] J. L. Boxerman *et al.* "The Role of Preload and Leakage Correction in Gadolinium-Based Cerebral Blood Volume Estimation Determined by Comparison with MION as a Criterion Standard". In: *American Journal of Neuroradiology* 33.6 (June 2012), pp. 1081–1087. ISSN: 0195-6108. DOI: 10.3174/ajnr.A2934.

[3] C. C. Quarles *et al.* "A theoretical framework to model DSC-MRI data acquired in the presence of contrast agent extravasation". In: *Physics in Medicine and Biology* 54.19 (Oct. 2009), pp. 5749–5766. ISSN: 0031-9155. DOI: 10.1088/0031-9155/54/19/006.

[4] J. L. Boxerman, K. M. Schmainda, and R. M. Weisskoff. "Relative cerebral blood volume maps corrected for contrast agent extravasation significantly correlate with glioma tumor grade, whereas uncorrected maps do not." In: *AJNR. American journal of neuroradiology* 27.4 (Apr. 2006), pp. 859–67. ISSN: 0195-6108.

[5] R. Leigh *et al.* "Arrival Time Correction for Dynamic Susceptibility Contrast MR Permeability Imaging in Stroke Patients". In: *PLoS ONE* 7.12 (Dec. 2012), e52656. ISSN: 1932-6203. DOI: 10.1371/journal.pone.0052656.

[6] A. Bjornerud *et al.* "T1- and T2*-dominant extravasation correction in DSC-MRI: part I–theoretical considerations and implications for assessment of tumor hemodynamic properties." In: *Journal of cerebral blood flow and metabolism : official journal of the International Society of Cerebral Blood Flow and Metabolism* 31.10 (Oct. 2011), pp. 2041–53. ISSN: 1559-7016. DOI: 10.1038/jcbfm.2011.52.

[7] K. Leu *et al.* "Bidirectional Contrast agent leakage correction of dynamic susceptibility contrast (DSC)-MRI improves cerebral blood volume estimation and survival prediction in recurrent glioblastoma treated with bevacizumab". In: *Journal of Magnetic Resonance Imaging* 44.5 (Nov. 2016), pp. 1229–1237. ISSN: 1053-1807. DOI: 10.1002/jmri.25227.

[8] L. Hu *et al.* "Impact of Software Modeling on the Accuracy of Perfusion MRI in Glioma". In: *American Journal of Neuroradiology* 36.12 (Dec. 2015), pp. 2242–2249. ISSN: 0195-6108. DOI: 10.3174/ajnr.A4451.

[9] L. Hu *et al.* "Correlations between Perfusion MR Imaging Cerebral Blood Volume, Microvessel Quantification, and Clinical Outcome Using Stereotactic Analysis in Recurrent High-Grade Glioma". In: *American Journal of Neuroradiology* 33.1 (Jan. 2012), pp. 69–76. ISSN: 0195-6108. DOI: 10.3174/ajnr.A2743.

[10] M. A. Prah *et al.* "Spatial discrimination of glioblastoma and treatment effect with histologically-validated perfusion and diffusion magnetic resonance imaging metrics". In: *Journal of Neuro-Oncology* 136.1 (Jan. 2018), pp. 13–21. ISSN: 0167-594X. DOI: 10.1007/s11060-017-2617-3.

[11] R. Haselhorst *et al.* "Dynamic susceptibility contrast MR imaging of plaque development in multiple sclerosis: Application of an extended blood-brain barrier leakage correction". In: *Journal of Magnetic Resonance Imaging* 11.5 (May 2000), pp. 495–505. ISSN: 1053-1807. DOI: 10.1002/(SICI)1522-2586(200005)11:5<495::AID-JMRI5>3.0.CO;2-S.

[12] C. C. Quarles, B. D. Ward, and K. M. Schmainda. "Improving the reliability of obtaining tumor hemodynamic parameters in the presence of contrast agent extravasation". In: *Magnetic Resonance in Medicine* 53.6 (June 2005), pp. 1307–1316. ISSN: 0740-3194. DOI: 10.1002/mrm.20497.

[13] R. Weisskoff *et al.* "Simultaneous blood volume and permeability mapping using a single Gd-based contrast injection". In: *the 2nd Annual Meeting of SMRM*. San Francisco, 1994, p. 279.

[14] C. Lavini *et al.* "Pixel-by-pixel analysis of DCE MRI curve patterns and an illustration of its application to the imaging of the musculoskeletal system". In: *Magnetic Resonance Imaging* 25.5 (June 2007), pp. 604–612. ISSN: 0730725X. DOI: 10.1016/j.mri.2006.10.021.

[15] P. S. Tofts. "Modeling tracer kinetics in dynamic Gd-DTPA MR imaging". In: *Journal of Magnetic Resonance Imaging* 7.1 (Jan. 1997), pp. 91–101. ISSN: 1053-1807. DOI: 10.1002/jmri.1880070113.

[16] P. S. Tofts *et al.* "Estimating kinetic parameters from dynamic contrast-enhanced t1-weighted MRI of a diffusable tracer: Standardized quantities and symbols". In: *Journal of Magnetic Resonance Imaging* 10.3 (Sept. 1999), pp. 223–232. ISSN: 1053-1807. DOI: 10.1002/(SICI)1522-2586(199909)10:3<223::AID-JMRI2>3.0.CO;2-S.

[17] M. Rohrer *et al.* "Comparison of Magnetic Properties of MRI Contrast Media Solutions at Different Magnetic Field Strengths". In: *Investigative Radiology* 40.11 (Nov. 2005), pp. 715–724. ISSN: 0020-9996. DOI: 10.1097/01.rli.0000184756.66360.d3.

[18] V. G. Kiselev. "Transverse relaxation effect of MRI contrast agents: A crucial issue for quantitative measurements of cerebral perfusion". In: *Journal of Magnetic Resonance Imaging* 22.6 (Dec. 2005), pp. 693–696. ISSN: 1053-1807. DOI: 10.1002/jmri.20452.

[19] G. C. Newman *et al.* "Experimental Estimates of the Constants Relating Signal Change to Contrast Concentration for Cerebral Blood Volume by T2* MRI". In: *Journal of Cerebral Blood Flow & Metabolism* 26.6 (June 2006), pp. 760–770. ISSN: 0271-678X. DOI: 10.1038/sj.jcbfm.9600242.

[20] B. Kjølby, L. Østergaard, and V. Kiselev. "Theoretical model of intravascular paramagnetic tracers effect on tissue relaxation". In: *Magnetic Resonance in Medicine* 56.1 (July 2006), pp. 187–197. ISSN: 0740-3194. DOI: 10.1002/mrm.20920.

[21] M. R. Orton *et al.* "Computationally efficient vascular input function models for quantitative kinetic modelling using DCE-MRI." In: *Physics in medicine and biology* 53.5 (Mar. 2008), pp. 1225–39. ISSN: 0031-9155. DOI: 10.1088/0031-9155/53/5/005.

[22] X. Zhang *et al.* "In vivo blood T1 measurements at 1.5 T, 3 T, and 7 T". In: *Magnetic Resonance in Medicine* 70.4 (Oct. 2013), pp. 1082–1086. ISSN: 07403194. DOI: 10.1002/mrm.24550.

[23] A. Petrovic *et al.* "Time related changes of T1, T2, and T2* of human blood in vitro". In: *Forensic Science International* 262 (May 2016), pp. 11–17. ISSN: 03790738. DOI: 10.1016/j.forsciint.2016.02.032.

[24] Y. Shen *et al.* "T1 relaxivities of gadolinium-based magnetic resonance contrast agents in human whole blood at 1.5, 3, and 7 T." In: *Investigative radiology* 50.5 (May 2015), pp. 330–8. ISSN: 1536-0210. DOI: 10.1097/RLI.0000000000000132.

[25] F. Calamante, E.-j. P. A. Vonken, and M. J. P. van Osch. "Contrast agent concentration measurements affecting quantification of bolus-tracking perfusion MRI." In: *Magnetic resonance in medicine* 58.3 (Sept. 2007), pp. 544–53. ISSN: 0740-3194. DOI: 10.1002/mrm.21362.

[26] M. Pedersen *et al.* "Quantitative cerebral perfusion using the PRESTO acquisition scheme". In: *Journal of Magnetic Resonance Imaging* 20.6 (Dec. 2004), pp. 930–940. ISSN: 10531807. DOI: 10.1002/jmri.20206.

[27] M. Saranathan *et al.* "DIfferential subsampling with cartesian ordering (DISCO): A high spatio-temporal resolution dixon imaging sequence for multiphasic contrast enhanced abdominal imaging". In: *Journal of Magnetic Resonance Imaging* 35.6 (June 2012), pp. 1484–1492. ISSN: 10531807. DOI: 10.1002/jmri.23602.

[28] S. Klein *et al.* "elastix: A Toolbox for Intensity-Based Medical Image Registration". In: *IEEE Transactions on Medical Imaging* 29.1 (Jan. 2010), pp. 196–205. ISSN: 0278-0062. DOI: 10.1109/TMI.2009.2035616.

[29] V. Fonov *et al.* "Unbiased average age-appropriate atlases for pediatric studies". In: *NeuroImage* 54.1 (Jan. 2011), pp. 313–327. ISSN: 10538119. DOI: 10.1016/j.neuroimage.2010.07.033.

[30] V. Fonov *et al.* "Unbiased nonlinear average age-appropriate brain templates from birth to adulthood". In: *NeuroImage* 47 (July 2009), S102. ISSN: 10538119. DOI: 10.1016/S1053-8119(09)70884-5.

[31] F. Isensee *et al.* "nnU-Net: a self-configuring method for deep learning-based biomedical image segmentation". In: *Nature Methods* 18.2 (Feb. 2021), pp. 203–211. ISSN: 1548-7091. DOI: 10.1038/s41592-020-01008-z.

[32] P. Kickingereder *et al.* "Relative cerebral blood volume is a potential predictive imaging biomarker of bevacizumab efficacy in recurrent glioblastoma." In: *Neuro-oncology* 17.8 (Aug. 2015), pp. 1139–47. ISSN: 1523-5866. DOI: 10.1093/neuonc/nov028.

[33] H. M. Luu and S.-H. Park. "Extending nn-UNet for Brain Tumor Segmentation". In: 2022, pp. 173–186. DOI: 10.1007/978-3-031-09002-8{_}16.

[34] T. Rohlfing, D. Russakoff, and C. Maurer. "Performance-Based Classifier Combination in Atlas-Based Image Segmentation Using Expectation-Maximization Parameter Estimation". In: *IEEE Transactions on Medical Imaging* 23.8 (Aug. 2004), pp. 983–994. ISSN: 0278-0062. DOI: 10.1109/TMI.2004.830803.

[35] P. A. Yushkevich *et al.* "User-guided 3D active contour segmentation of anatomical structures: Significantly improved efficiency and reliability". In: *NeuroImage* 31.3 (July 2006), pp. 1116–1128. ISSN: 10538119. DOI: 10.1016/j.neuroimage.2006.01.015.

[36] W. Shin, H. Gu, and Y. Yang. "Fast high-resolution T1 mapping using inversion-recovery look-locker echo-planar imaging at steady state: Optimization for accuracy and reliability". In: *Magnetic Resonance in Medicine* 61.4 (Apr. 2009), pp. 899–906. ISSN: 07403194. DOI: 10.1002/mrm.21836.

[37] K. J. Friston *et al.* "Statistical parametric maps in functional imaging: A general linear approach". In: *Human Brain Mapping* 2.4 (1994), pp. 189–210. ISSN: 10659471. DOI: 10.1002/hbm.460020402.

[38] K. Friston *et al.* “Characterizing Dynamic Brain Responses with fMRI: A Multivariate Approach”. In: *NeuroImage* 2.2 (June 1995), pp. 166–172. ISSN: 10538119. DOI: 10.1006/nimg.1995.1019.

[39] J. J. N. Van Schie *et al.* “Estimating the arterial input function from dynamic contrast-enhanced MRI data with compensation for flow enhancement (I): Theory, method, and phantom experiments”. In: *Journal of Magnetic Resonance Imaging* 47.5 (May 2018), pp. 1190–1196. ISSN: 10531807. DOI: 10.1002/jmri.25906.

[40] C.-H. Tseng *et al.* “Arterial input function estimation compensating for inflow and partial voluming in dynamic contrast-enhanced MRI”. In: *NMR in Biomedicine* (Aug. 2024). ISSN: 0952-3480. DOI: 10.1002/nbm.5225.

[41] C.-H. Tseng *et al.* “Improved reliability of perfusion estimation in dynamic susceptibility contrast MRI by using the arterial input function from dynamic contrast enhanced MRI”. In: *NMR in Biomedicine* 37.1 (Jan. 2024). ISSN: 0952-3480. DOI: 10.1002/nbm.5038.

[42] V. C. Keil *et al.* “DCE-MRI in Glioma, Infiltration Zone and Healthy Brain to Assess Angiogenesis: A Biopsy Study”. In: *Clinical Neuroradiology* 31.4 (Dec. 2021), pp. 1049–1058. ISSN: 1869-1439. DOI: 10.1007/s00062-021-01015-3.

[43] R. Wirestam *et al.* “Dynamic susceptibility contrast perfusion MRI using phase-based venous output functions: comparison with pseudo-continuous arterial spin labelling and assessment of contrast agent concentration in large veins”. In: *Magnetic Resonance Materials in Physics, Biology and Medicine* 29.6 (Dec. 2016), pp. 823–831. ISSN: 0968-5243. DOI: 10.1007/s10334-016-0567-y.

[44] E. Lind *et al.* “Assessment of MRI contrast agent concentration by quantitative susceptibility mapping (QSM): application to estimation of cerebral blood volume during steady state.” In: *Magma (New York, N.Y.)* 30.6 (Dec. 2017), pp. 555–566. ISSN: 1352-8661. DOI: 10.1007/s10334-017-0637-9.

[45] K. Leu *et al.* “Improved Leakage Correction for Single-Echo Dynamic Susceptibility Contrast Perfusion MRI Estimates of Relative Cerebral Blood Volume in High-Grade Gliomas by Accounting for Bidirectional Contrast Agent Exchange.” In: *AJNR. American journal of neuroradiology* 37.8 (Aug. 2016), pp. 1440–6. ISSN: 1936-959X. DOI: 10.3174/ajnr.A4759.

[46] F. Arzanforoosh *et al.* “Effect of Applying Leakage Correction on rCBV Measurement Derived From DSC-MRI in Enhancing and Nonenhancing Glioma”. In: *Frontiers in Oncology* 11 (Mar. 2021). ISSN: 2234-943X. DOI: 10.3389/fonc.2021.648528.

[47] E.-j. P. Vonken *et al.* “Simultaneous quantitative cerebral perfusion and Gd-DTPA extravasation measurement with dual-echo dynamic susceptibility contrast MRI”. In: *Magnetic Resonance in Medicine* 43.6 (June 2000), pp. 820–827. ISSN: 0740-3194. DOI: 10.1002/1522-2594(200006)43:6<820::AID-MRM7>3.0.CO;2-F.

[48] K. E. Emblem *et al.* “T1- and T2*-Dominant Extravasation Correction in DSC-MRI: Part II—Predicting Patient Outcome after a Single Dose of Cediranib in Recurrent Glioblastoma Patients”. In: *Journal of Cerebral Blood Flow & Metabolism* 31.10 (Oct. 2011), pp. 2054–2064. ISSN: 0271-678X. DOI: 10.1038/jcbfm.2011.39.

[49] D. S. Sankaralayam *et al.* “Evaluating the Role of Leakage Correction of Hemodynamic Parameters derived from Dynamic Contrast Enhanced MRI for Glioma Grading”. In: *Journal of Magnetic Resonance Imaging* (Mar. 2024). ISSN: 1053-1807. DOI: 10.1002/jmri.29338.

# 6

# Discussion and Conclusion

## 6.1. RESEARCH OVERVIEW

This dissertation aimed to enhance the accuracy of quantitative parameter estimation from contrast-agent enhanced perfusion MRI and to further increase its value for clinical applications. Particularly, I combined dynamic contrast enhanced (DCE) MRI with dynamic susceptibility contrast (DSC) MRI to (1) establish an optimal strategy for measurement of the arterial input function (AIF), (2) limit inflow and partial volume effects (PVEs) on AIF estimation from DCE MRI, and (3) reduce the errors emanating from contrast agent leakage in DSC MRI.

In Chapter 2 I reviewed the current state-of-the-art in DCE and DSC MRI for imaging of glioma. A substantial amount of pre-clinical and clinical research conclude that parameters from DCE and DSC imaging hold promise as potential biomarkers for evaluation of glioma. However, widespread integration of these perfusion techniques into clinical practice has yet to be realized. Further practical adoption could be facilitated by establishing consensus recommendations for data acquisition on systems from different vendors and in cross-center studies, and by standardizing the analysis methods. This would enhance the reliability and comparability of perfusion measurements in a clinical setting.

In Chapter 3 I studied the use of an AIF obtained from DCE MRI prior to DSC imaging, for use in the analysis of the DSC data. I established that DCE-derived AIFs exhibit superior similarity across different vessels compared to those derived from DSC MRI, which in effect enhanced the reproducibility of perfusion parameter estimation. Alternatively, a semi-automatic algorithm eased the identification of the AIFs, which showed relative consistency. However, these AIFs had unrealistic shape: they exhibited unnaturally high peaks and small widths. Importantly, the quantitative attributes of a DCE-derived AIF may inherently promise more accurate quantification of perfusion parameters from DSC MRI.

In Chapter 4 I proposed a novel approach to simultaneously compensate for inflow effect and PVE on the AIF measurement from DCE MRI. I demonstrated that an increase in PVE closely correlates with an increased inflow effect. Through a mathematical derivation and numerical simulation, I validated the similarity of the two effects. In clinical datasets, the proposed method enabled reconstruction of realistic AIFs in the presence of variable inflow effect and PVE. Furthermore, while the superior sagittal sinus (SSS) is generally less affected by these issues, it proved unsuitable for obtaining a substitute AIF due to increased contrast agent dispersion. This dispersion leads to an overestimation of vascular permeability coefficients compared to using AIFs. Thus, our findings suggest that a more effective strategy for DCE MRI analysis is to derive the AIF directly from an artery, with meticulous correction for inflow and PVE, ensuring accurate and reliable assessments of vascular parameters.

In Chapter 5 I developed a general model to fit the signals obtained from DCE and DSC images, respectively. This model enables the estimation of contrast agent concentration in tissue from DCE imaging, which is subsequently used to eliminate the leakage contamination on DSC signals. Simulation demonstrated that the model successfully fit the signals and provided unbiased estimates of the

estimators. Moreover, the leakage effect was effectively removed from the $\Delta R_2^*$ curves, which are used to derive the clinically valuable coefficient, cerebral blood volume (CBV). While applying the leakage correction methods on clinical datasets, the widely applied Boxerman–Schmainda–Weisskoff (BSW) correction method [1] enforces a return of the $\Delta R_2^*$ curves to the baseline level. Instead, my method conserved the level in the tail of the tissue concentration curve, reflecting residual contrast concentration in the vasculature after the main bolus, which is much more expected due to remain Gadolinium-based contrast agents (GBCAs) in the vascular system.

## 6.2. LIMITATIONS

While this dissertation has made several contributions to the field of contrast enhanced perfusion MRI, several limitations must be acknowledged.

In Chapter 3 we showed that the AIFs derived from DCE data had improved reproducibility and reliability compared to traditional AIF estimation in DSC MRI. However, a major limitation was the lack of a 'true' AIF for comparison. Ideally, a true AIF could have been obtained directly from blood sampling, but this is generally not feasible. Furthermore, it was assumed that the change in $R_2^*$ ($\Delta R_2^*$) in tissue is linearly proportional to the contrast agent concentration. Also, the relaxivity of the GBCA ($r_2^*$) was presumed to be constant and independent of tissue type. This assumption is a common simplification in DSC studies but may not be universally true. Relaxivity could vary among different tissue types and might be influenced by factors such as the local microvascular architecture, permeability, and proton exchange rates between tissue and blood.

Chapter 4 explored a correction method for compensation of flow and PVEs on the AIF measurement in DCE data. However, the impact of AIF on the estimation of key pharmacokinetic model parameters, such as $K^{trans}$, was not investigated due to the absence of observable contrast leakage in the $T_1$-weighted images of the patients in this part of our study. Our data was acquired post-tumor resection and several months after proton radiation therapy. It could be that the effect induced by this type of radiotherapy is subtle or barely detectable within this short period after treatment. Clearly, further research is required to establish this.

In Chapter 5 introduced an innovative leakage correction method for DSC MRI analysis. As above a limitation of this work was that ground truth data (e.g. for CBV measurement) was not available. In general, establishing a reference for parameters like CBV is challenging, as it can only be measured in very indirect ways and is highly dependent on physiological condition of the subject.

An additional limitation that holds for my entire dissertation is that all analyses concerned only a limited number of subjects. Particularly, normal control subjects and subjects with specific types of glioma were not included. At same time, however, the results reveal the potential that combined analysis of DCE and DSC data may offer.

While these limitations restrict the interpretation of our findings, they also underscore the need for further research to refine the methodology and expand the applicability in clinical practice.

## 6.3. RELATION TO RECENT DEVELOPMENTS

During the course of my research project there were several developments that are relevant to my work.

In Chapter 3, we concluded that AIF derivation from DCE MRI outperforms AIF determination from DSC MRI regarding the reproducibility. However, a recent study by Kang et al. presents a contrasting viewpoint [2]. The latter study concluded that DCE-derived pharmacokinetic parameters using the DSC AIF showed improved reliability and yielded enhanced diagnostic accuracy for differentiating glioblastoma with low relative CBV (rCBV) from primary central nervous system lymphoma. Possibly, this discrepancy could be due to the lower temporal resolution of the DCE imaging (2.8 seconds) compared to the DSC series (1.6 seconds). Furthermore, a recent paper by Knutsson et al. [3] provided a comprehensive overview of the role of AIFs in various perfusion MRI techniques. The study highlighted the challenges associated with accurately measuring AIFs in DSC MRI, which aligns with the issues discussed in Chapter 3 of this dissertation. The integration of DCE-derived AIFs into DSC analysis in Chapter 3 was shown to yield accurate assessment of perfusion-related parameters.

Also, Gwilliam et al. [4] recently reported that quantitative $T_1$ measurement in flowing blood using spoiled gradient echo sequences is subject to large measurement errors which are non-linear in relation to flow velocity. This can undermine the value of using AIFs since an erroneous $T_1$ value is used for concentration mapping. Therefore, it is suggested that a larger effort should be put in developing tissue-level AIF estimation methods. In my opinion this also underscores the relevance of the approach presented in Chapter 4 of my dissertation, which effectively compensates for mixed contamination from inflow effect and PVEs. Additionally, the AIFs corrected as such exhibited more reasonable and reliable patterns compared to the venous output function (VOF) measured from the SSS. On the other hand, we did not optimize the VOF measurement, as the approach we took is more compatible with clinical applications. Lately, Bourassa-Moreau et al. [5] proposed a novel, complex-signal based method for determining the VOF from the SSS, which accounts for blood inflow and vessel curvature. This approach was shown to be robust against biases such as errors in the asserted blood $T_1$ value and blood fraction. This development suggests that reconsidering the use of VOF measured from the SSS as a surrogate vascular input function in DCE analysis could be valuable.

Recently, Hedderich et al. [6] investigated whether appropriate leakage correction could obviate the need for a preload contrast injection. Specifically, DSC-based rCBV measurements from two consecutive contrast injections were compared. Their study demonstrated that the BSW correction method resulted in

the highest agreement between rCBV values obtained with and without prebolus contrast agent administration, highlighting the potential of excluding the prebolus injection in DSC acquisition. However, in this paper only the one-directional model was investigated. Arzanforoosh et al. [7] evaluated the impact of leakage correction on rCBV estimates, noting that a bidirectional model for leakage correction had a stronger effect than unidirectional correction, particularly in enhancing tumors. Our approach in Chapter 5, utilizes an estimated leakage term from a bidirectional model in DCE analysis, which is in line with the suggested approach in the Arzanforoosh paper. Finally, Sankaralayam et al [8] focused on evaluating the impact of leakage correction on hemodynamic parameters derived from DCE-MRI for glioma grading. In this study, the vascular permeability coefficient ($K^{trans}$) was employed to compensate for the leakage effect on DCE-derived CBV and CBF. Although the findings suggested that leakage correction might negatively impact the accuracy of glioma grading, the use of $K^{trans}$ for correcting leakage contamination is conceptually consistent with the approach discussed in Chapter 5 of my dissertation. The unexpected results may be attributed to the sensitivity of the applied model to noise, which underscores the advantages of our approach using the DSC sequence, which is specifically designed for accurate hemodynamic parameter measurement.



## 6.4. FUTURE DIRECTIONS

In my perspective, any developed technology should not only deliver additional scientific insight, but also fit with clinical practice. Therefore, the acquisition protocols applied in this dissertation need to be optimized. Specifically, we utilized two separate full doses of GBCA: one for DCE imaging that also serves as a preload for DSC imaging, the other especially for the DSC acquisition. The protocol ensured comprehensive coverage and good contrast in both series. However, the administration of two full doses of GBCA is currently less preferred in clinical practice. Recent research has explored the possibility of reducing the preload dosage in DSC acquisitions and has even suggested that a preload may be unnecessary when a low flip angle DSC-MRI is employed [9]. In spite of these findings, we proved that it may still be useful not to eliminate the preload as it facilitates deriving an accurate AIF and vascular parameters while DCE imaging is applied. At the same time, it is important to investigate what (minimal) dosage and sequence duration should be applied in order to obtain the most reliable and relevant information on the vascularization.

In Chapter 3 we evaluated different sources and methods for AIF extraction. However, numerous automatic AIF searching approaches implemented in other studies were not included in our analysis. More than that, artificial intelligence (AI), particularly convolutional neural networks (CNNs), are increasingly applied to automate AIF assessment in MRI studies. For instance, Fan et al. [10] developed a multi-stream 3D CNN to determine the AIF voxels. This method was shown to outperform traditional manual and automatic methods. Similarly, Winder et al. [11] applied a CNN framework to automatically identify AIFs from Computed

Tomography perfusion data as well as from DSC MRI datasets. The CNN-derived AIFs showed higher cross-correlation values and were comparable to manual AIFs in terms of shape features. Both studies demonstrated the potential of deep learning in automating the estimation of the AIF from perfusion images. It is clearly of interest to study the effectiveness of such approaches with combined DCE-DSC imaging (specifically when the total GBCA dose is minimized at the same time) and compare them with our methods.

The methodologies proposed in this dissertation enhanced the accuracy and reliability of perfusion measurements. Our methods are potentially applicable in a broad range of clinical applications, such as in monitoring post-treatment effects in glioma patients. Utilizing the refined AIF extraction from Chapter 4 for enhanced DCE-derived vascular coefficients, or the corrected rCBV using the approach from Chapter 5, might improve the differentiation between recurrent tumors and post-treatment effects. Moreover, the methodologies have the potential to aid in tumor grading, classification, and predicting treatment efficacy, which are all pivotal aspects in the workup of oncology patients. Future research should also focus on validating our methods across different clinical datasets, including distinct patient cohorts, scan protocols and scanners, to further substantiate the benefits and pave the way for routine clinical use.



Alternatively, arterial spin labeling (ASL) is an MRI perfusion technique that does not require administration of a contrast agent. Instead, inflowing spins are exploited as an intrinsic tracer, allowing for (absolute) CBF measurement, which makes it a valuable tool in various clinical settings [12]. While ASL precludes a GBCA, it is traditionally associated with a low signal-to-noise ratio and a lack of familiarity among clinicians. Addressing these shortcomings through continued research and further technological improvements could enhance the clinical viability of ASL. Comparing the outcomes of the novel DCE and DSC approaches developed in this dissertation with those obtained via ASL could be another topic of further research. This comparison may be crucial for establishing the value of ASL and broadening its clinical acceptance and application.

## 6.5. CONCLUSION

This dissertation has advanced the field of perfusion MRI through innovative methodologies that improve the accuracy and reliability of perfusion parameter estimation. I have renewed the image analysis procedures for DCE and DSC MRI, specifically by creating novel techniques for AIF measurement from DCE MRI and by introducing a new combined approach for leakage correction in DSC imaging. It is my sincerest hope that these developed methods will not only improve the clinical utility of perfusion MRI but also inspire further innovations and broader applications of contrast-agent based perfusion MRI.

# REFERENCES


[1] J. L. Boxerman, K. M. Schmainda, and R. M. Weisskoff. "Relative cerebral blood volume maps corrected for contrast agent extravasation significantly correlate with glioma tumor grade, whereas uncorrected maps do not." In: *AJNR. American journal of neuroradiology* 27.4 (Apr. 2006), pp. 859–67. ISSN: 0195-6108.

[2] K. M. Kang *et al.* "Differentiation between glioblastoma and primary CNS lymphoma: application of DCE-MRI parameters based on arterial input function obtained from DSC-MRI". In: *European Radiology* 31.12 (Dec. 2021), pp. 9098–9109. ISSN: 0938-7994. DOI: 10.1007/s00330-021-08044-z.

[3] L. Knutsson, R. Wirestam, and E. Lind. "Arterial input function: A friend or a foe?" In: 2023, pp. 171–196. DOI: 10.1016/B978-0-323-95209-5.00011-8.

[4] M. N. Gwilliam *et al.* "Quantifying MRI T 1 relaxation in flowing blood: implications for arterial input function measurement in DCE-MRI". In: *The British Journal of Radiology* 94.1119 (Mar. 2021). ISSN: 0007-1285. DOI: 10.1259/bjr.20191004.

[5] B. Bourassa-Moreau *et al.* "Robust arterial input function surrogate measurement from the superior sagittal sinus complex signal for fast dynamic contrast-enhanced MRI in the brain". In: *Magnetic Resonance in Medicine* 86.6 (Dec. 2021), pp. 3052–3066. ISSN: 0740-3194. DOI: 10.1002/mrm.28922.

[6] D. Hedderich *et al.* "Consistency of normalized cerebral blood volume values in glioblastoma using different leakage correction algorithms on dynamic susceptibility contrast magnetic resonance imaging data without and with preload". In: *Journal of Neuroradiology* 46.1 (Feb. 2019), pp. 44–51. ISSN: 01509861. DOI: 10.1016/j.neurad.2018.04.006.

[7] F. Arzanforoosh *et al.* "Effect of Applying Leakage Correction on rCBV Measurement Derived From DSC-MRI in Enhancing and Nonenhancing Glioma". In: *Frontiers in Oncology* 11 (Mar. 2021). ISSN: 2234-943X. DOI: 10.3389/fonc.2021.648528.

[8] D. S. Sankaralayam *et al.* "Evaluating the Role of Leakage Correction of Hemodynamic Parameters derived from Dynamic Contrast Enhanced MRI for Glioma Grading". In: *Journal of Magnetic Resonance Imaging* (Mar. 2024). ISSN: 1053-1807. DOI: 10.1002/jmri.29338.

[9] J. L. Boxerman *et al.* "Consensus recommendations for a dynamic susceptibility contrast MRI protocol for use in high-grade gliomas". In: *Neuro-Oncology* 22.9 (Sept. 2020), pp. 1262–1275. ISSN: 1522-8517. DOI: 10.1093/neuonc/noaa141.

[10] S. Fan *et al.* "An Automatic Estimation of Arterial Input Function Based on Multi-Stream 3D CNN". In: *Frontiers in Neuroinformatics* 13 (July 2019). ISSN: 1662-5196. DOI: 10.3389/fninf.2019.00049.

[11] A. Winder *et al.* "Automatic arterial input function selection in CT and MR perfusion datasets using deep convolutional neural networks". In: *Medical Physics* 47.9 (Sept. 2020), pp. 4199–4211. ISSN: 0094-2405. DOI: 10.1002/mp.14351.

[12] R. L. Wolf and J. A. Detre. “Clinical Neuroimaging Using Arterial Spin-Labeled Perfusion Magnetic Resonance Imaging”. In: *Neurotherapeutics* 4.3 (July 2007), pp. 346–359. ISSN: 18787479. DOI: 10.1016/j.nurt.2007.04.005.

# ACKNOWLEDGEMENTS

During the past few years, the moment of reaching this page has always been envisioned in my mind. Expressing my heartfelt gratitude to everyone who supported me along this journey is the most fitting way to close this long, winding chapter of my life.

First, I would like to thank several PIs in Taiwan who introduced me to this captivating field and encouraged me during the early stages of my research career. **Wen-Yih**, joining your lab for my graduate studies unlocked my research journey. I could not have ventured into the MRI world—or pursued a PhD—without your unwavering support. I wish you every success in your new endeavors following your retirement from academia. **Fa-Hsuan**, your persistent encouragement to think outside the box left an indelible mark; the inspiration you provided helped shape my way of thinking—a foundation that proved invaluable throughout my PhD. **Li-Wei** and **Wen-Tsau**, as emerging MRI researchers, you generously shared your experiences and offered me a broad perspective on what life in research entails. Although our encounters were few, each meeting at international conferences felt like a warm return to my beloved hometown. **Hsu-Hsia**, thank you for introducing me to Wen-Yih's lab, where I discovered my true passion and committed myself to the MRI community. Special thanks go to the late **Fu-Nien** at NTHU. I took my very first course on MRI principles with you, and your kindness and passion paved the way for my entry into this field. Your passing is a profound loss not only to the university but to the entire community. May you rest in peace.

Next, I extend my deepest gratitude to my supervisors during my PhD in Delft. **Frans**, your guidance alleviated many challenges along this journey. Thank you for granting me the freedom and trust to balance academic pursuits with personal growth. I cherished our weekly meetings and the stimulating discussions we shared. You consistently offered clear direction and patiently explored alternative approaches whenever obstacles arose. Beyond academic mentoring, you helped me embrace Dutch culture—each coffee chat deepened my understanding of the Netherlands. I vividly recall that when I joined the team in 2020 during the UEFA European Championship season, I mentioned my unfamiliarity with football, and you replied, "Come on, guy, it is time to grow up!" Four years later, at the 2024 UEFA European Championship, I did grow up—finding myself more confident in the Dutch national team than you are! **Thijs**, you are among the most brilliant people I have ever met, and it has been a privilege to have you as my supervisor. My research would not have progressed as smoothly without your invaluable guidance. You consistently rescued us from impasses, steering us back on track—like a superhero in my academic journey. I deeply valued every discussion we shared. Thank you for your patient support. **Marion**, thank you sincerely for your assistance on the clinical front, including—but not limited to—recruiting pa-

tients and organizing data collection. Additionally, the events and workshops you organized brought together scholars from diverse backgrounds and provided opportunities to connect with others dedicated to the MRI community.

I would also like to thank the other members at MI. **Sebastian**, although we did not work directly together, every of our brief discussions left a profound impact; your passion for MRI shone through every conversation, and I appreciated the moments you joined us for a drink and shared invaluable guidance. **David**, you embody the spirited new generation of professors. I remember when I first joined in 2020 and you enthusiastically recounted your experience at a conference in Taiwan in 2015. Neither of us imagined that it would be again in Taiwan in 2024, giving me the delightful opportunity to show you around my hometown. I look forward to exploring even more of Taiwan's beauty together in the future. Furthermore, **Nico**, **Martin**, **Guillaume**, **Qian**, and **Rik**, thank you for fostering an exceptional research environment at MI and for the occasional hallway chats that brightened my days. I also extend my sincere gratitude to the secretaries and IT staff. **Angela** and **Annelies**, thank you for providing indispensable administrative support and organizing numerous events to ensure everything ran smoothly behind the scenes. Likewise, **Henry** and **Ranold** have been invaluable in managing IT needs and maintaining efficient systems. Your dedicated efforts greatly contributed to the smooth progress of my work, and I truly appreciate all that you do.

Next, I wish to thank my PhD and postdoc colleagues in our department. First, I acknowledge those who shared an office with me. **Martijn**, your talent and diligence continuously inspired me; your contributions during our early weekly meetings with Frans were invaluable. I wish you all continued success in your academic career. **Agis**, you never failed to engage me in conversation—whether lighthearted or profound. Your vibrant, sometimes chaotic spirit brought a unique energy to our workspace, and I will never forget our late-night drinking sessions. Most importantly, I will always cherish the mutual support we offered each other in the final stages of our PhD journey. Take care and see you in Crete one day. **Djama**, you were invariably the first to arrive at the office—even during the holiday season when others were away—serving as the steadfast guardian of our workspace. I treasured every moment we spent sharing our daily experiences, and your insightful suggestions on both research and life were always appreciated. I wish you and your family all the best, and I look forward to visiting Brazil soon. I am equally grateful to the other colleagues, **Paulina** and **Chiara**, you started your PhDs at the same time as I did. It brings me joy to see us all reach this milestone, and I sincerely appreciate your support, particularly during the challenging COVID period. **Rick**, **Hugues**, **Min**, and **Eleonora**, I cherish every relaxed moment and drinking session we shared. It was unforgettable showing you around my lovely hometown, and I hope you all enjoyed that and will return one day. Finally, I extend my gratitude to all the old and new colleagues at MI—**Martina**, **Niccolo**, **Ayda**, **Masa**, **Joao**, **Yidong**, **Yi**, **Fabian**, **Sabiju**, **Xiufeng**, **Dion**, **Moein**, **Gabrielle**, and **Baptiste**—as well as to the members of the CI group: **Wenxiu**, **Qingru**, **Huangcheng**, **Sobhan**, and **Alim**. Each of you has planted a memory in my heart during this journey.

Researchers at LUMC and Erasmus MC have also played crucial roles in my scientific endeavors. **Dirk**, although we did not collaborate closely, I am immensely grateful

for your valuable insights and the invitations to present to your group. I extend my thanks to **Jaap**, **Alejandra**, **Ilanah**, **Sophie**, **Esther**, and **Piotr** for assisting with patient recruitment, image acquisition, and data transfer; without your help, my work would not have progressed. It was a pleasure to collaborate with all of you. I would also like to express my gratitude to other PhDs—**Fatemeh**, **Yichuang**, **Yulun**, **Yiming**, **Daniëlle**, and **Krishnapriya**. Sharing our daily lives and exchanging research experiences has enriched this journey with vibrant chapters.

Living in a new country is challenging without the support of a community that shares the same cultural background. I must express my gratitude to the wonderful and closely connected Taiwanese community in the Netherlands. We have shared experiences, overcome challenges together, and enjoyed time during the holidays. Every moment spent playing Mahjong, drinking, partying, traveling, and celebrating our festivals has given me the courage to persevere. I also owe a great debt to my friends in Taiwan. Even though I have been away for years, every visit home has been met with warm enthusiasm and genuine care, fueling my energy to continue exploring the world.

Finally, I must thank my beloved family. You supported every endeavor of mine without hesitation, even when doubts arose. I could not have completed this journey without your unwavering love and support.

Thus, my PhD journey comes to a close. I am profoundly grateful to everyone mentioned above. This dissertation is as much a product of your support as it is of my own efforts.

# Curriculum Vitæ

## Chih-Hsien Tseng

March 25 1993 — Born in Taipei City, Taiwan.

## Education

2011–2015
Bachelor of Science
Biomedical Engineering and Environmental Science
*National Tsing Hua University*
Hsinchu City, Taiwan

2015–2017
Master of Science
Biomedical Engineering
*National Taiwan University*
Taipei City, Taiwan
*Thesis:* A novel algorithm for segmenting white matter hyperintensities based on mean apparent propagator MRI
*Supervisors:* Prof. dr. W.-Y. I. Tseng
Prof. dr. F.-H. Lin

2020–2024
Doctor of Philosophy
Applied Physics
*Delft University of Technology*
Delft, The Netherlands
*Thesis:* Improving contrast agent based cerebral perfusion assessment - Arterial input function measurement and leakage correction
*Promoters:* Dr. F.M. Vos
*Delft University of Technology*
Prof. dr. ir. M.J.P. van Osch
*Leiden University Medical Center*
Prof. dr. M. Smits
*Erasmus MC*

# List of Publications

## Journal Publications

1. **Tseng, C.-H.**, van Osch, M.J.P., Pruis, Ilanah J., Veldhuijzen van Zanten, Sophie E.M., Wielopolski, P., Smits, M. and Vos., F.M. Leakage correction in dynamic susceptibility contrast MRI: a combined analysis with dynamic contrast enhanced imaging. Submitted to *Magnetic Resonance in Medicine*.

2. **Tseng, C.-H.**, Nagtegaal, M.A., van Osch, M.J.P., Jaspers, J., Romero, A.M., Wielopolski, P., Smits, M. and Vos., F.M. Arterial input function estimation compensating for inflow and partial voluming in dynamic contrast enhanced MRI. *NMR in Biomedicine*. 2024;e5225. doi:10.1002/nbm.5225

3. **Tseng, C.-H.**, Jaspers, J, Romero, A.M., Wielopolski, P., Smits, M., van Osch, M.J.P. and Vos., F.M. Improved reliability of perfusion estimation in dynamic susceptibility contrast MRI by using the arterial input function from dynamic contrast enhanced MRI. *NMR in Biomedicine*. 2024; 37(1):e5038. doi:10.1002/nbm.5038

4. Hangel, G., Schmitz-Abecassis, B., Sollmann, N., Pinto, J., Arzanforoosh, F., Barkhof, F., Booth, T., Calvo-Imirizaldu, M., Cassia, G., Chmelik, M., Clement, P., Ercan, E., Fernández-Seara, M.A., Furtner, J., Fuster-Garcia, E., Grech-Sollars, M., Guven, N.T., Hatay, G.H., Karami, G., Keil, V.C., Kim, M., Koekkoek, J.A.F., Kukran, S., Mancini, L., Nechifor, R.E., Özcan, A., Ozturk-Isik, E., Piskin, S., Schmainda, K.M., Svensson, S.F., **Tseng, C.-H.**, Unnikrishnan, S., Vos, F., Warnert, E., Zhao, M.Y., Jancalek, R., Nunes, T., Hirschler, L., Smits, M., Petr, J. and Emblem, K.E. (2023), Advanced MR Techniques for Preoperative Glioma Characterization: Part 2. *J Magn Reson Imaging*, 57: 1676-1695. doi:10.1002/jmri.28663

5. Hirschler, L., Sollmann, N., Schmitz-Abecassis, B., Pinto, J., Arzanforoosh, F., Barkhof, F., Booth, T., Calvo-Imirizaldu, M., Cassia, G., Chmelik, M., Clement, P., Ercan, E., Fernández-Seara, M.A., Furtner, J., Fuster-Garcia, E., Grech-Sollars, M., Guven, N.T., Hatay, G.H., Karami, G., Keil, V.C., Kim, M., Koekkoek, J.A.F., Kukran, S., Mancini, L., Nechifor, R.E., Özcan, A., Ozturk-Isik, E., Piskin, S., Schmainda, K., Svensson, S.F., **Tseng, C.-H.**, Unnikrishnan, S., Vos, F., Warnert, E., Zhao, M.Y., Jancalek, R., Nunes, T., Emblem, K.E., Smits, M., Petr, J. and Hangel, G. (2023), Advanced MR Techniques for Preoperative Glioma Characterization: Part 1. *J Magn Reson Imaging*, 57: 1655-1675. doi:10.1002/jmri.28662

## Conference Contributions

1. **Tseng, C.-H.**, Nagtegaal, M.A., van Osch, M.J.P., Jaspers, J., Romero, A.M., Wielopolski, P., Smits, M. and Vos., F.M. "A dedicated arterial input function compensating for inflow and partial voluming in dynamic contrast enhanced MRI."

    a) In: Proc. Intl. Soc. Mag. Reson. Med. 31. ISMRM. Toronto, June 2023. Digital Poster.

b) ISMRM Benelux, Brussels, March 2023. Poster presentation.

2. **Tseng, C.-H.**, Jaspers, J, Romero, A.M., Wielopolski, P., Smits, M., van Osch, M.J.P. and Vos., F.M. "Comparison of arterial input functions obtained through back-to-back acquisition of DCE and DSC MRI."

   a) In: Proc. Intl. Soc. Mag. Reson. Med. 30. ISMRM. London, May 2023. Digital Poster.

   b) ISMRM Benelux, Maastricht, April 2022. Poster presentation.

## SUPERVISED STUDENT PROJECTS

1. Erik Visnar. "Assessment of feasibility of the integration of dynamic imaging within conventional imaging using combined pharmacokinetic models." May 2023 - September 2023. *TU Delft* Applied Physics. Grade 7.5.

2. Jasper van Leeuwen. "Repercussion of proton therapy on white matter; A tract-based correlation analysis between the alteration of diffusion anisotropy and irradiation dose." April 2021 - July 2021. *TU Delft* Applied Physics. Grade 7.5.